Volume 7(1), 2026

Journal of Energy, Material, and Instrumentation Technology (JEMIT)

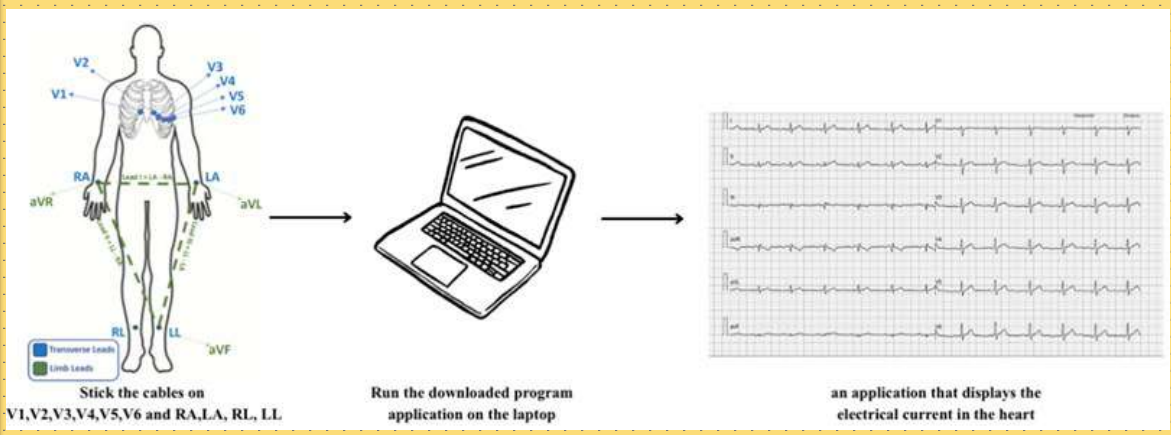

Figure 2. page 29

MAIN ISSUE

Biopolymer Gel from Pineapple Peel (*Ananas comosus*) Waste-Based Gel with Sodium Chloride (NaCl) for Optimizing Electrocardiogram (ECG) Signal Recording

Page 174 — 182

Journal of Energy, Material, and Instrumentation Technology
ISSN 2747-2043, Volume 7(1), 2026

EDITORIAL OFFICE
Department of Physics, University of Lampung
Street on Prof. Dr. Soemantri Brodjonegoro, Number 1, Bandar Lampung
Tel. 0721-701609 Ext. 719 Fax. 0721-704625
Email: jemit@fmipa.unila.ac.id
http://jemit.fmipa.unila.ac.id/

The Department of Physics publishes this journal, Faculty of Mathematics and Natural Sciences, the University of Lampung, in collaboration with the Indonesian Physics Association, Lampung Branch, as a means to publish research results and review articles from researchers in the fields of energy physics, materials, and instrumentation technology. This journal is published four times a year (February, May, August, and November). The first volume was published in 2020 under the Journal **of Energy, Materials, and Instrumentation Technology (JEMIT)** with ISSN 2747-2043.

The first issue of this journal is in Indonesian. However, starting with edition vol 3 no 2, the article was published in English.

Journal of Energy, Material, and Instrumentation Technology
ISSN 2747-2043, Volume 7(1), 2026

TABLE OF CONTENTS

JOURNAL OF ENERGY, MATERIALS, AND INSTRUMENTATION TECHNOLOGY

Journal Webpage https://jemit.fmipa.unila.ac.id/

Analysis of Utilization of Alumina and Carbon Concentrations in Salt Bridges in Electrochemical Cells $Zn|Zn^{2+}_{(Aq)}||Ag^{+}_{(Aq)}|Cu(Ag)$ with Electrolyte Seawater and *Zinc Acid* as Alternative Energy Sources

Mayang Shavira[(a)], Gurum Ahmad Pauzi[(b)], Sri Wahyu Suciyati, and Amir Supriyanto

Department of Physics, Faculty of Mathematics and Natural Sciences, University of Lampung, Indonesia 354145

Article Information

Article history:
Received January 16, 2023
Received in revised form July 9, 2024
Accepted July 9, 2024

Keywords: *seawater, salt bridge, electrical characteristics, zinc acid, voltaic cell.*

Abstract

This study was conducted to analyze the comparison of variations in the salt bridge in a two-compartment voltaic cell with a Cu(Ag)-Zn electrode on the resulting electrical characteristics. The Cu(Ag)-Zn pair is used to generate voltage and current in the cell with seawater electrolyte and zinc acid. The two compartments are lined with a salt bridge made of Al_2O_3 (aluminum oxide), and Carbon, NaCl (seawater) dissolved in Tiga Roda white cement. The voltaic cell consists of 4 cells arranged in series, each cell filled with ±200 ml of seawater (cathode part) and ±200 ml of acid zinc solution (anode part). The voltaic cell was measured with a multitester every 1 hour for 3 days. Based on the research that has been done, it can be concluded that the variation of the carbon salt bridge with a concentration of 12 grams has the greatest electrical characteristic value.

Informasi Artikel

Proses artikel:
Diterima 16 Januari 2023
Diterima dan direvisi dari 9 Juli 2024
Accepted 9 Juli 2024

Kata kunci: *Air laut, jembatan garam, karakteristik elektrik, larutan acid zinc, sel volta*

Abstrak

Penelitian ini dilakukan untuk menganalisis perbandingan variasi jembatan garam pada sel volta dua kompartemen dengan electrode Cu(Ag)-Zn terhadap nilai karakteristik elektrik yang dihasilkan. Pasangan Cu(Ag)-Zn digunakan untuk menghasilkan tegangan dan arus dalam sel dengan elektrolit air laut dan acid zinc. Dua kompartemen dibatasi dengan jembatan garam yang terbuat dari Al_2O_3 (aluminium oksida), dan Carbon, NaCl (air laut) yang terlarut dalam semen putih tiga roda. Sel volta terdiri dari 4 sel yang tersusun secara seri yang setiap sel terisi dengan ±200 ml air laut (bagian katode) dan ±200 ml larutan acid zinc (bagian anode). Sel volta diukur dengan multitester setiap 1 jam sekali selama 3 hari. Berdasarkan penelitian yang telah dilakukan diperoleh kesimpulan bahwa variasi jembatan garam carbon konsentrasi 12 gram memiliki nilai karakteristik elektrik yang paling besar.

1. Introduction

The use of voltaic cells is the result of applying electrochemical cells to produce renewable energy technologies (Harahap, 2016). A voltaic cell in one cell causes electron transfer to occur quickly causing corrosion due to the potential difference in an electrolyte environment (Bardal, 2003 and Wibowo, 2016). Therefore, a method is needed to inhibit corrosion in voltaic cells by controlling the rate of electron transfer by coating zinc Zn (Ansari et al, 2017 and Prabhu et al, 2012). Zn zinc coating can use the salt bridge principle in electrochemical cells, one of which is by separating seawater electrolyte Zn electrodes and Cu electrodes in two different cells. If the seawater cells are separated, no electricity will occur, so that in electrochemical cells a salt bridge is needed so that the ions in the solution are balanced and a chemical change occurs into an electrical change (Chang, 2003). The salt bridge has the function of balancing cations and anions in solution. The requirements for a salt bridge are that it can be passed by ions and only a little through the solvent (Arizal et al, 2017). The results of research conducted by Akbar et al (2017) made a voltaic cell with the help of a salt bridge using bacteria as a catalyst to generate electric current and Haq et al (2018) made a voltaic cell with the help of a salt bridge for power generation applications using salt energy as an

* Corresponding author.
E-mail address: (a)mayangshavira23@gmail.com (b)gurum@fmipa.unila.ac.id

electrolyte. The results of this study indicate that the presence of a salt bridge in a voltaic cell causes the flow of electrons in a balanced solution to produce an electric current.

Rizki's research (2019) has succeeded in making electrochemical cells in voltaic cells without the aid of a salt bridge with electrodes in the form of Cu(Ag)-Zn plates to determine the electrical characteristics of seawater. The drawbacks of this study were that the resulting electrical characteristics decreased due to the release of the Zn electrode due to corrosion, which was then corrected by Anjarwati's research (2019) who designed a voltaic cell with the help of a salt bridge using Cu(Ag)-Zn electrodes in the form of Cu (copper) fibers and adding NaCl and KCl salt bridges in an electrochemical process. In this study, a voltaic cell system with two compartments was used which was limited by a variation of the Al_2O_3 salt bridge (aluminum oxide) and a variation of the carbon salt bridge added with NaCl (seawater) and Tiga Roda white cement. Each cell has a pair of Cu(Ag)-Zn electrodes, the cathode compartment (Cu(Ag)) contains seawater while the anode compartment (Zn) contains zinc acid solution. The use of zinc acid solution in this study is expected to restore the quality of the oxidized anode electrode. So to find out this, an analysis of variations of the salt bridge was carried out on the electrical characteristics and corrosion rate of the two-compartment voltaic cell system with Cu(Ag)-Zn electrodes.

2. Research Methods

The tools used in this study included: seawater electrolyte media made of acrylic, cells made of acrylic material with a thickness of 3 mm, a height of 16 cm, a width of 7.5 cm and a length of 14 cm, zinc metal with a size of 4 x 5 x 0.002 cm, Ag-electroplated Cu fibers with a length of 100 cm, 20 LEDs in series, and a multimeter. The materials used in this study were: seawater, NH_4Cl, $ZnCl_2$, distilled water. The salt bridge materials are Al_2O_3 (aluminum oxide) 102 grams and 12 grams carbon, NaCL (sea water) and white cement brand three wheels. This research was carried out in several stages, namely the process of electroplating Ag on Cu, making salt bridges, making zinc acid solutions, designing and manufacturing voltaic cell systems as well as testing tools and data collection.

2.1. Ag Electroplating on Cu

The electroplating process uses a carbon rod as the anode and Cu fibers 2.5 mm in diameter and 100 cm long as the cathode. In the Ag electroplating process on Cu, 300 ml of 0.02M silver plating solution ($AgNO_3$) was used as the electrolyte solution. Before electroplating the Cu fibers were cleaned using 1% HNO_3 solution to reduce the fat content attached to the Cu fibers. Then the Cu fibers were cleaned again using 96% ethanol to remove the HNO_3 content that was still attached to Cu. Furthermore, electroplating was carried out with a voltage of 2 volts for 5 minutes.

2.2. Construction of the Salt Bridge

At this stage, the process of making a salt bridge is a mixture of Al_2O_3 (aluminum oxide) + NaCl (seawater) + Tiga Roda white cement and carbon + NaCl (seawater) + Tiga Roda white cement. The first step to make this salt bridge is to mix 102 grams of Al_2O_3, 58.5 grams of NaCl and 50 grams of Tiga Roda white cement, then stir until the three ingredients are mixed. Then the mixture of materials is printed directly in the cell to avoid leaks, then dry it and wait for it to harden. The purpose of making this salt bridge is to maintain the neutrality of the electric charge in the solution.

2.3. Preparation of *Zinc Acid* Solution

The process for making zinc acid pH 5 is mixing 150 grams of ammonium chloride, 40 grams of zinc chloride with 1 liter of distilled water (Ansari, et al. 2017). Then check the pH of the solution using universal pH paper.

2.4. Design and Manufacture of the Voltaic Cell System

Before the research was carried out, a two-compartment voltaic cell media design was made using the SketchUp 2020 application as a manufacturing reference as shown in Figure 1, Figure 2, and Figure 3. In this study, the voltaic cell system was composed of 4 cells made of acrylic material with a thickness of 3mm . Each cell contains a pair of Cu(Ag)-Zn electrodes with different compartments bounded by a salt bridge. The salt bridge used is a mixture of Al_2O_3 (aluminum oxide) + NaCl (seawater) and carbon + NaCl (seawater) dissolved in Tiga Roda white cement. In each voltaic cell, the electrolyte used in the cathode compartment (Cu(Ag)) contains ±200 ml of seawater, while the anode compartment (Zn) contains ±200 ml of *zinc acid* solution pH 5. The electrolyte used will be replaced every 24 hours. The voltaic cell system in this study is connected in series using a connecting cable.

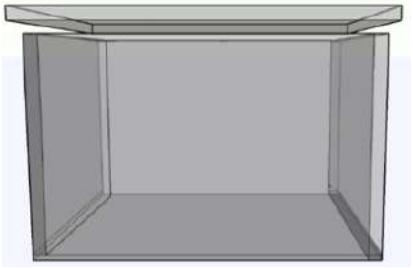

Figure 1. Single voltaic cell design

Shavira M, Pauzi GA, Suciyati SW, and Supriyanto A, 2026, Analysis of Utilization of Alumina and Carbon Concentrations in Salt Bridges in Electrochemical Cells Zn|Zn^{2+}(Aq)||Ag^{+}(Aq)|Cu(Ag) with Electrolyte Seawater and Zinc Acid as Alternative Energy Sources, *Journal of Energy, Material, and Instrumentation Technology* Vol. 7 No. 1, 2026

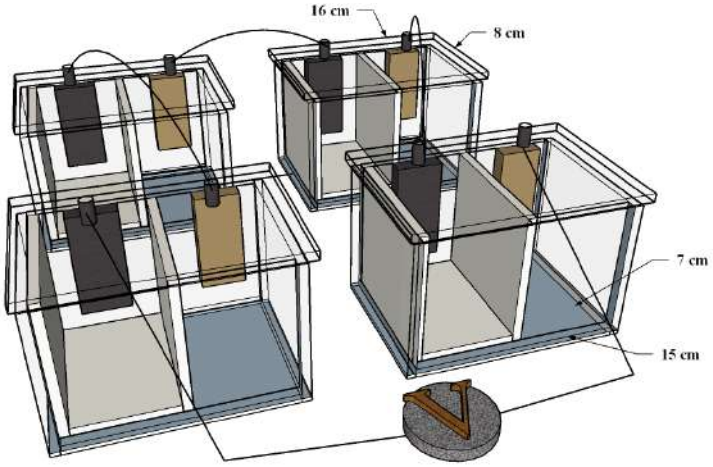

Figure 2. Voltaic cell arrangement design

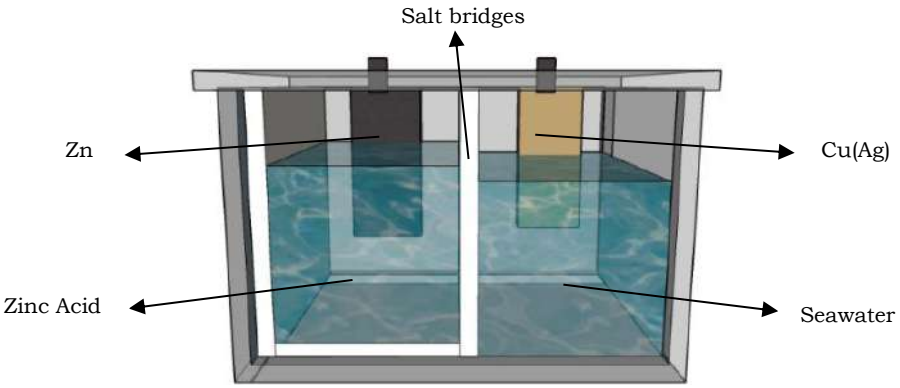

Figure 3. Compartment cells with salt bridges

2.5. Tool Testing and Data Retrieval

Tool testing is carried out by connecting a voltaic cell to a multitester that has been connected to the load (20 LEDs). Electrical energy analysis is carried out by collecting data in the form of no-load voltage (volts), load voltage (volts), current (A), light intensity (lux), calculation of internal resistance (R_{in}) (kOhm) using Equation 1 and calculating the power generated using Equation 2. Data collection is done every 1 hour for 72 hours. In this system, a simple circuit is used to measure the resulting electrical characteristic values as in Figure 4.

(a) (b)

Figure 4. Circuit to measure the values (a) OCV and (b) CCV

$$R_{in} = \frac{OCV - CCV}{I} \quad (1)$$

$$P = CCV\, I \quad (2)$$

Open circuit voltage is a measurement of electrical variables when a load that has been used for some time is removed. Meanwhile, close circuit voltage is a measurement of electrical variables that have been used for some time when the load is installed. In Equation (1) R_{in} = internal resistance (Ω), *OCV* = open circuit voltage (volts), *CCV* = closed circuit voltage (volts) and *I* = current strength (amperes). In Equation 2 *P* = power (watts), *CCV* = close circuit voltage (volts) and *I* = current strength (amperes).

3. Results and Discussions

The data produced at a carbon concentration of 12 grams for OCV in the first hour was 4.15 Volts, while in the 72nd hour it was 3.53 Volts. Based on this data, it is known that OCV decreased after the first hour. This decrease occurred because the electrode had not initially been oxidized and after the first hour it began to oxidize and there was still a lot of dissolved oxygen in the solution, resulting in a maximum OCV value. In the next hour the electrode used began to oxidize so that the electron activity on the electrode began to be hampered so that the OCV value decreased. For CCV in the first hour it is 3.28 Volts. The stability of the CCV value in the 12 gram carbon salt bridge variation occurred at the 16th to the 20th hour, the 30th to the 34th hour, the 37th to the 41st hour, and the 52nd to the 41st hour. -57. Based on this data, it can be seen that the CCV value has decreased, this happens because CCV is directly proportional to the E value (OCV).

The current value obtained in the first hour was 3.91 mA, the value at the 72nd hour was 2.31 mA. This situation is caused because the value of the current produced is directly proportional to the value of V (CCV). The greater the CCV value, the greater the electric charge that can be moved so that the resulting current (I) value will be greater. The light intensity value produced in the first hour is 22 lux, while in the 72nd hour it is 7 lux. This situation is caused because the light intensity value produced is directly proportional to the current value (I), the greater the current value, the greater the light intensity value produced.

The resulting internal resistance value is 0.281 kΩ. The R_{in} value on the carbon salt bridge has increased due to corrosion on the electrode which becomes an obstacle in the cell. The longer the corrosion occurs, the greater the Rin value will be. This is also in accordance with the OCV, CCV and I values obtained based on Ohm's Law, namely the resistance value is inversely proportional to the voltage and current values. And for the maximum power value produced, namely 12,825 mWatt, the power value after 72 hours is 6,214 mWatt. The 12 gram Carbon salt bridge has a large Power value, this situation occurs because the Power value is the result of multiplying the CCV and I values. The higher the CCV and I values, the greater the resulting Power value.

3.1 Realization of the Voltaic Cell System

Realization of a two-compartment voltaic cell system made from seawater electrolyte and zinc acid solution to produce electricity can be seen in Figure 4. In this study the electrical characteristics of the voltaic cell (voltage, current and light intensity) were measured using a multitester and luxmeter to test the resulting electrical characteristics.

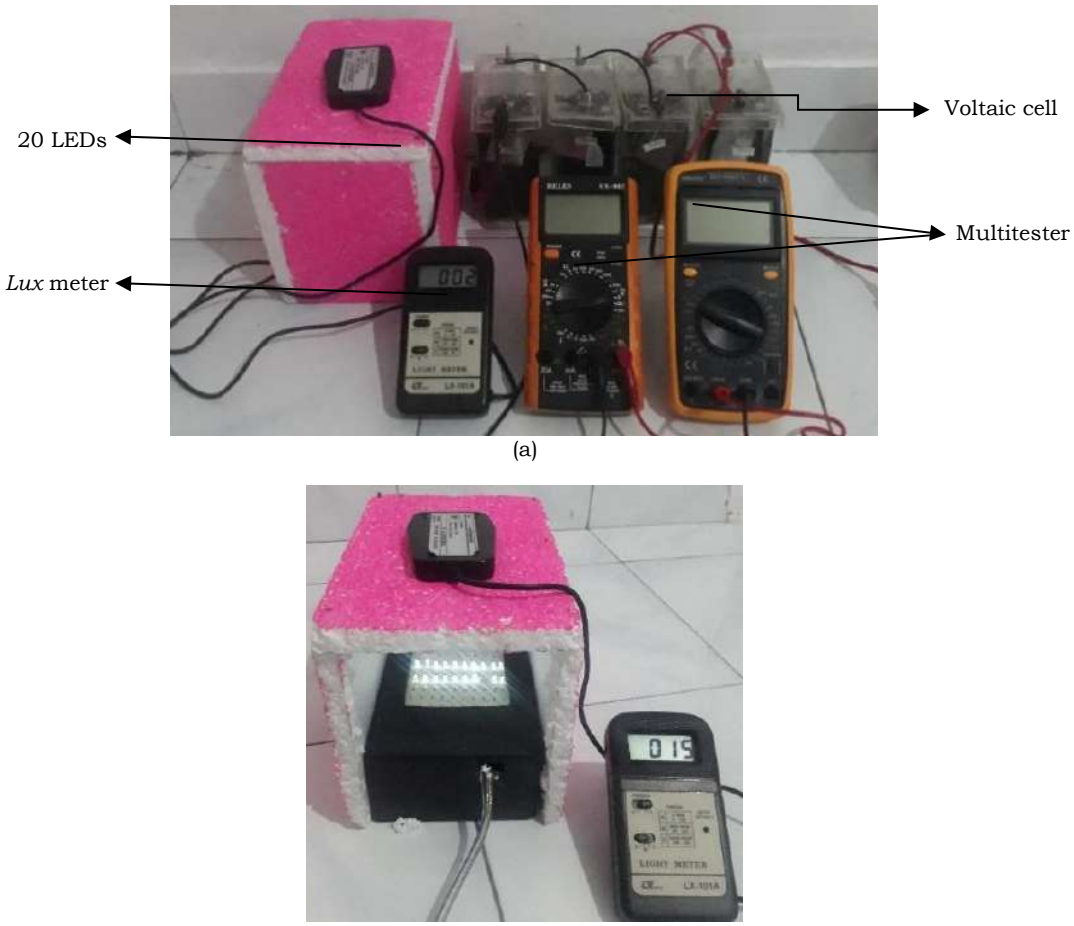

Figure 5. (a) Realization of the voltaic cell system (b) Array of LEDs used

Shavira M, Pauzi GA, Suciyati SW, and Supriyanto A, 2026, Analysis of Utilization of Alumina and Carbon Concentrations in Salt Bridges in Electrochemical Cells Zn|Zn^{2+}(Aq)||Ag^{+}(Aq)|Cu(Ag) with Electrolyte Seawater and Zinc Acid as Alternative Energy Sources, *Journal of Energy, Material, and Instrumentation Technology* Vol. 7 No. 1, 2026

3.2 Data Comparison of Electrical Characteristics of Alumina and Carbon

1. Open Circuit Voltage (*OCV*) and *Close Circuit Voltage* (*CCV*). The OCV and CCV values of the alumina and carbon salt bridges can be seen in Figure 6 (a) and (b).

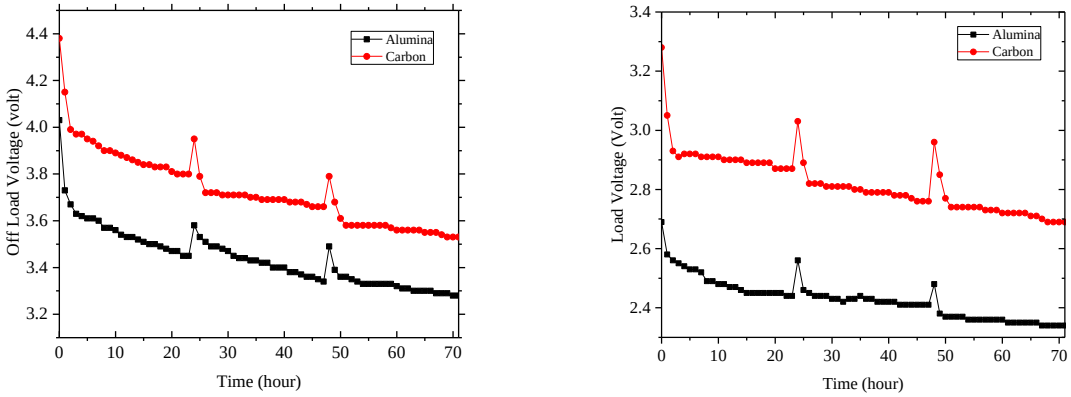

(a) (b)

Figure 6. (a) Comparison of *OCV* values on alumina and carbon salt bridges (b) Comparison of *CCV* values on alumina and carbon salt bridges

The graphs in Figure 5 (a) and (b) show that the Open Circuit Voltage (*OCV*) and Close Circuit Voltage (*CCV*) values of the carbon salt bridge are greater than those of the alumina salt bridge. In Figure 5 (a) the *OCV* of the carbon salt bridge produces a value in the first (maximum) hour of 4.15 volts and at the 72nd hour which is 3.53 volts, while the alumina salt bridge produces a value of 4.03 volts and at the 72nd hour the 72nd is 3.28 volts. In Figure 5 (b) the *CCV* of the carbon salt bridge produces a value in the first hour of 3.28 volts, while the alumina salt bridge produces a value of 2.59 volts.

2. Current and Light Intensity. The graph in Figure 6 (a) shows a comparison of the current values of the alumina salt bridge and the salt bridge. The current value of the carbon salt bridge for the first hour is 3.91 mA and at the 72nd hour it is 2.31 mA, while for the alumina salt bridge the value for the first hour is 3.49 mA and at the 72nd hour it is 1.81 mA. The graph in Figure 6 (b) shows the light intensity obtained by the carbon salt bridge in the first hour, namely 22 lux and at the 72nd hour, it was 7 lux, while for the alumina salt bridge, it was 18 lux and at the 72nd hour, it was 6 lux.

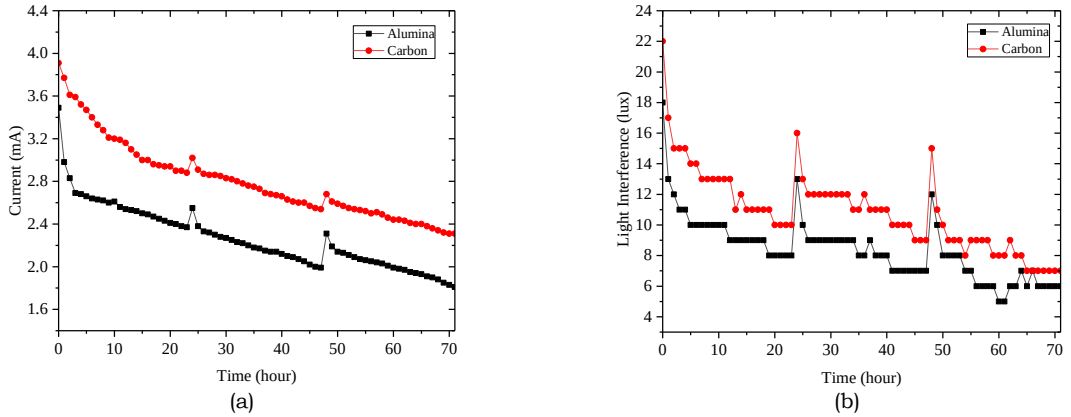

(a) (b)

Figure 7. (a) Comparison of current values on alumina and carbon salt bridges (b) Comparison of light intensity on alumina and carbon salt bridges

3. Resistance and Power. The graph in Figure 7 (a) shows the value of the internal resistance (R_{in}) obtained by the carbon salt bridge of 0.281 kΩ, while that of the alumina salt bridge is 0.384 kΩ. The power value shown in Figure 7 (b) for the carbon salt bridge is 12.825 mWatt, while for the alumina salt bridge it is 9.388 mWatt. The carbon salt bridge has a lower resistance value and has a greater power value than the alumina salt bridge.

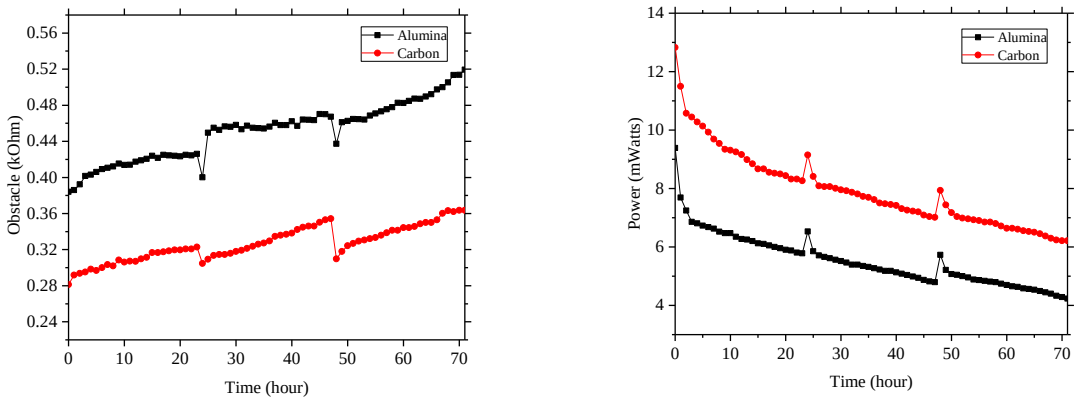

(a) (b)

Figure 8. (a) Comparison of resistance values on alumina and carbon salt bridges (b) Comparison of power values on alumina and carbon salt bridges

4. Conclusions

Based on the research that has been done, it can be concluded that the greater the concentration of the salt bridge, the denser the carbon and Al_2O_3 content in the salt bridge will increase the resistance of H^+ ions to pass through the salt bridge, so that the redox reaction is hampered and produces a smaller value of electrical characteristics. This study also concluded that the use of carbon salt bridges will improve the electrical characteristics of the voltaic cell and the use of zinc acid solution creates opportunities to regenerate the Zn anode.

5. Bibliography

Akbar, T. N., Kirom, M. R., & Iskandar, R. F. (2017). Analisis pengaruh material logam sebagai elektroda microbial fuel cell terhadap produksi energi listrik. *E-Proceeding of Engineering, 4*(2), 2123–2138.

Anjarwati, A. (2019). *Analisis aplikasi jembatan garam pada sel elektrokimia menggunakan elektroda Cu(Ag)-Zn berbahan elektrolit air laut* [Skripsi, University of Lampung].

Ansari, I., Indrawijaya, B., Nurohmawati, F., & Zakaria, I. (2017). Pengaruh waktu dan luas permukaan terhadap ketebalan produk pada elektroplating acid zinc. *Jurnal Ilmiah Teknik Kimia UNPAM, 1*(1), 1–7.

Arizal, F., Hasbi, M., & Kadir, A. (2017). Pengaruh kadar garam terhadap daya yang dihasilkan pembangkit listrik tenaga air garam sebagai energi alternatif terbarukan. *Enthalphy: Jurnal Ilmiah Mahasiswa Teknik Mesin, 2*(1), 1–5.

Bardal, E. (2003). *Corrosion and protection*. Springer.

Chang, R. (2003). *General chemistry: The essential concepts*. Erlangga.

Haq, S. Z. N., Kurniawan, E., & Ramdhani, M. (2018). Analisis pembangkit elektrik menggunakan media air garam sebagai larutan elektrolit. *E-Proceeding of Engineering, 5*(3), 3823–3830.

Harahap, M. R. (2016). Sel elektrokimia: Karakteristik dan aplikasi. *Circuit, 2*(1), 177–180.

Pauzi, G. A., Pratiwi, N. A., Surtono, A., & Suciyati, S. W. (2022). Analisis pengaruh variasi pH larutan acid zinc pada sel volta dua kompartemen dengan elektrode Cu(Ag)-Zn. *Journal of Energy, Material, and Instrumentation Technology, 3*(1), 21–30. https://doi.org/10.23960/jemit.v3i1.88

Prabhu, R. A., Venkatesha, T. V., & Praveen, B. M. (2012). Electrochemical study of the corrosion behavior of zinc surface treated with a new organic chelating inhibitor. *ISRN Metallurgy*, 2012, Article 940107. https://doi.org/10.5402/2012/940107

Rizki, K. C. (2019). *Analisis pengaruh elektroplating perak (Ag) pada tembaga (Cu) terhadap karakteristik elektrik air laut sebagai sumber energi listrik terbarukan* [Skripsi, University of Lampung].

Wibowo, A. (2016). Analisis sifat korosi galvanik berbagai plat logam di Laboratorium Metalurgi Politeknik Negeri Batam. *Jurnal Integrasi, 8*(2), 144–147.

Wicaksono, D., Bhakti, T. L., Taruno, R. B., Subroto, M. R. S., & Mustikasari, A. (2021). Sistem sensor untuk pemantauan kadar oksigen terlarut berbasis galvanic pada kolam budidaya ikan air tawar. *Jurnal Teknologi dan Sistem Komputer, 9*(2), 83–89.

JOURNAL OF ENERGY, MATERIALS, AND INSTRUMENTATION TECHNOLOGY

Journal Webpage https://jemit.fmipa.unila.ac.id/

Carbonated Hydroxyapatite (CHAp)/PCL/Gelatin Scaffold Synthesized from Wrinkled Purple Snail Shell Waste for Bone Regeneration

Fadilah Salsabilla, Rosita Wati*, Aldi Herbanu, Marsudi Siburian, and Endah

Department of Biomedical Engineering, Institut Teknologi Sumatera, Lampung Selatan, Indonesia, 35365

Article Information

Article history:
Received September 2, 2025
Received in revised form October 28, 2025
Accepted October 29, 2025

Keywords: *wrinkled purple snail, freeze-drying, carbonate hydroxyapatite, polycaprolactone, scaffold*

Abstract

Traffic accidents are a major cause of bone fractures in Indonesia, highlighting the urgent need for effective biomaterials in bone regeneration. This study synthesized carbonated hydroxyapatite (CHAp) from wrinkled purple sea snail shells (Nucella lamellosa) using a precipitation method and sintering at 600 °C, followed by the fabrication of CHAp/PCL/Gelatin scaffolds through freeze-drying. XRD confirmed B-type CHAp with a crystallite size of 9.86 nm, crystallinity of 62.07%, and a Ca/P ratio of 1.76. The incorporation of PCL and gelatin decreased scaffold crystallinity to 37.29% and increased the Ca/P ratio to 3.19. FTIR spectra verified the presence of CO_3^{2-}, PO_4^{3-}, OH^- groups, as well as characteristic peaks of PCL and gelatin. SEM analysis revealed a porous interconnected structure with an average pore size of 28.94 µm. The scaffold exhibited compressive strength of 2.693 MPa, within the range of trabecular bone, and showed a 3% mass loss after 24 h, indicating suitable initial biodegradation. These findings demonstrate the potential of snail shell-derived CHAp/PCL/Gelatin scaffolds as biodegradable biomaterials for bone regeneration.

Informasi Artikel

Proses artikel:
Diterima 2 September 2025
Diterima dan direvisi dari 28 Oktober 2025
Accepted 29 Oktober 2025

Kata kunci: *keong ungu keriput, freeze-drying, karbonat hidroksiapatit, polikaprolakton, scaffold*

Abstrak

Kecelakaan lalu lintas merupakan penyebab utama patah tulang di Indonesia, sehingga diperlukan biomaterial yang efektif untuk regenerasi tulang. Penelitian ini bertujuan untuk mensintesis karbonat hidroksiapatit (CHAp) dari cangkang keong laut ungu keriput (Nucella lamellosa) menggunakan metode presipitasi dan sintering pada suhu 600 °C, kemudian dilanjutkan dengan pembuatan scaffold CHAp/PCL/Gelatin melalui metode freeze-drying. Hasil XRD mengonfirmasi bahwa CHAp yang terbentuk merupakan tipe B dengan ukuran kristalit 9.86 nm, tingkat kristalinitas 62.07%, dan rasio Ca/P sebesar 1.76. Penambahan PCL dan gelatin menurunkan kristalinitas scaffold menjadi 37.29% dan meningkatkan rasio Ca/P menjadi 3.19. Analisis FTIR menunjukkan keberadaan gugus fungsi CO_3^{2-}, PO_4^{3-}, dan OH^-, serta puncak khas dari PCL dan gelatin. Analisis SEM memperlihatkan struktur berpori dengan keterhubungan yang baik dan rata-rata ukuran pori 28.94 µm. Uji mekanik menunjukkan kekuatan tekan scaffold sebesar 2.693 MPa, berada dalam rentang nilai kekuatan tulang trabekular, sementara uji biodegradasi menunjukkan kehilangan massa sebesar 3% setelah 24 jam, yang menandakan laju degradasi awal yang sesuai. Hasil ini menunjukkan bahwa scaffold CHAp/PCL/Gelatin berbasis limbah cangkang keong memiliki potensi sebagai biomaterial biodegradable untuk aplikasi regenerasi tulang.

* Corresponding author.
E-mail address: rosita.wati@bm.itera.ac.id

1. Introduction

Traffic accidents are among the leading causes of bone fractures in Indonesia, often resulting in disabilities that require advanced medical interventions. According to the World Health Organization (WHO), millions of bone injury cases, including those caused by traffic accidents, occur worldwide each year. In Indonesia, the Ministry of Health reported that traffic accidents are one of the main contributors to bone injuries, with the 2018 Riskesdas survey showing that 31.4% of injuries occur on the road, 44.7% in the home environment, and 9.1% in the workplace (Kementerian Kesehatan RI, 2018). Bone fractures demand effective treatments, and one promising approach is bone tissue engineering (Cieza, A., et al., 2021).

Bone tissue engineering integrates biological science and engineering to restore, repair, or maintain damaged tissue function. Scaffolds play a crucial role as three-dimensional (3D) structures that support cell attachment, proliferation, and differentiation, facilitating tissue regeneration (Lee et al., 2022). The choice of biomaterial is critical to scaffold performance, particularly for bone tissue engineering. Among various biomaterials, calcium phosphate-based bioceramics, such as hydroxyapatite (HAp) and its carbonate-substituted form, carbonated hydroxyapatite (CHAp), are widely used due to their biocompatibility, bioactivity, and osteoconductivity (Min et al., 2024).

Bone tissue damage remains a major health concern in Indonesia due to high cases of accidents and degenerative bone diseases, leading to an increased need for effective bone regeneration strategies. However, conventional bone grafts often face limitations such as donor site morbidity, infection risk, and high cost. Therefore, the development of biocompatible, biodegradable, and sustainable scaffolds for bone tissue engineering is urgently needed. This research focuses on synthesizing Carbonated Hydroxyapatite (CHAp) derived from *Wrinkled Purple Snail Shells,* combined with PCL and gelatin, to provide an eco-friendly and effective alternative scaffold for bone regeneration applications.

In this study, CHAP was synthesized from *wrinkled purple snail shell* (*Nucella lamellose*), an abundant marine waste in coastal lampung (Permatasari et al., 2021). The synthesis of CHAp from *wrinkled purple snail shells* aligns with green synthesis principles because it utilizes marine waste as a calcium source, minimizes the us of hazardous chemicals, and promotes resource sustainability (Nguyen et al., 2022). This eco-friendly approach supports the concept of sustainable biomaterial development in biomedical engineering. The physicochemical, mechanical, and biodegradation properties to assess its potential for bone tissue engineering application

2. Research Methods

2.1 Tools and Materials

The tools used in this research included an analytical (for accurate weighing), an oven (for drying samples), a furnace (for sintering), a magnetic stirrer (for homogeneous mixing), a centrifuge (for separating precipitate), and a freeze dryer (for obtaining porous structures). Characterization instruments consisted of X-ray Diffraction (XRD, to determine crystal phases), Fourier Transform Infrared Spectroscopy (FTIR, to identify functional groups), Scanning Electron Microscope–Energy Dispersive X-ray (SEM–EDX, to observe morphology and elemental composition), and Universal Testing Machine (UTM, to evaluate mechanical strength). The materials used were wrinkled purple snail shells (*Nucella lamellose*), collected from coastal areas in Lampung, Indonesia; sodium hydroxide (NaOH, Merck, ≥99% purity); ammonium dihydrogen phosphate ($NH_4H_2PO_4$, Merck, analytical grade); polycaprolactone (PCL, Sigma-Aldrich, Mw 80,000); and gelatin (food grade). Distilled water was used as a solvent throughout the synthesis process.

2.2 Preparation of Raw Wrinkled Purple Snail Shell

The raw shells of wrinkled purple sea snails (*Nucella lamellose*) were collected from coastal areas in Lampung, Indonesia. Prior to use, the shells were thoroughly cleaned by boiling in distilled water for 30 minutes to remove organic debris and surface impurities. The cleaned shells were then dried under the sun for 24 hours, followed by oven drying at 100°C for 2 hours to eliminate residual moisture. After drying, the shells were mechanically crushed into smaller fragments using a mortar and pestle and further ground into fine powder with a ball mill. The powdered shells served as the calcium source for the subsequent synthesis of carbonated hydroxyapatite (**Figure 1**).

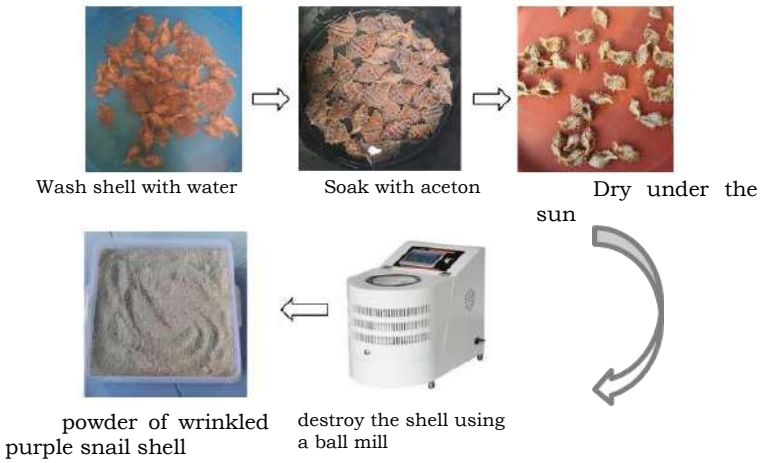

Figure 1. Preparation step

2.3 Synthesis of CHAp

Wrinkled purple snail shells were washed, boiled, and dried to remove organic residues. The dried shells were calcined at 1000 °C for 4 hours to obtain CaO powder. CaO was then dissolved in distilled water to form $Ca(OH)_2$ solution. $NH_4H_2PO_4$ solution was prepared separately. The $Ca(OH)_2$ solution was added dropwise with $NH_4H_2PO_4$ under continuous stirring at a Ca/P molar ratio of 1.67 (corresponding to a molar ratio of Ca : P : C = 0.4175 : 0.25 : 0.25), maintaining pH 10 by adding NaOH 1 M. The precipitate was aged for 24 hours, filtered, and dried at 100 °C. The powder was sintered at 600 °C for 2 hours to obtain CHAp (**Figure 2**).

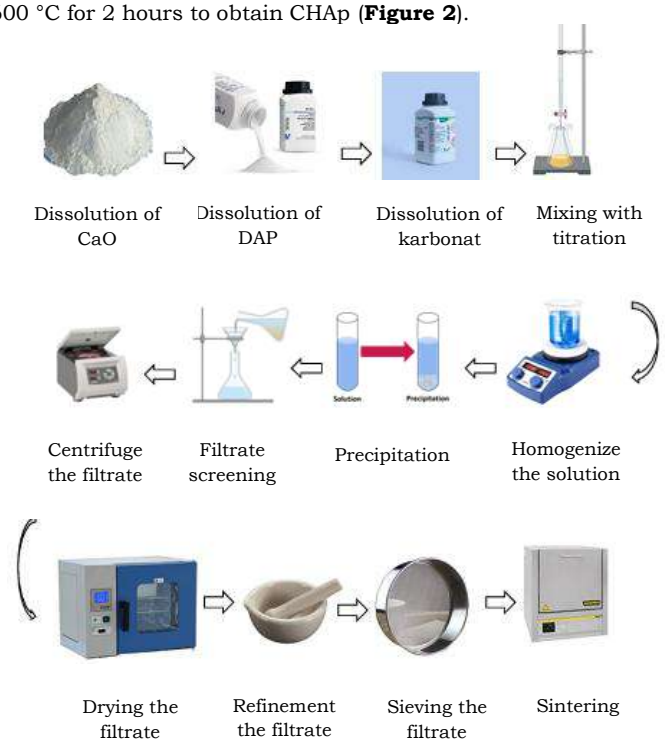

Figure 2. Synthesis of CHAp

2.4 Fabrication of CHAp/PCL/Gelatin Scaffold

PCL was dissolved in dichloromethane (DCM) and mixed with gelatin dissolved in distilled water at 50 °C, using a composition of 3 g CHAp in 30 mL solvent (0.1 M), 1.8 g PCL in 18 mL acetone (1.25×10^{-3} M), and 2.6 g gelatin in 26 mL solvent (1.1×10^{-3} M). CHAp powder was gradually added to the polymer solution and stirred until homogeneous. The suspension was poured into molds and frozen at −20 °C for 24 hours, followed by freeze-drying for 48 hours to produce porous CHAp/PCL/Gelatin scaffold (**Figure 3**).

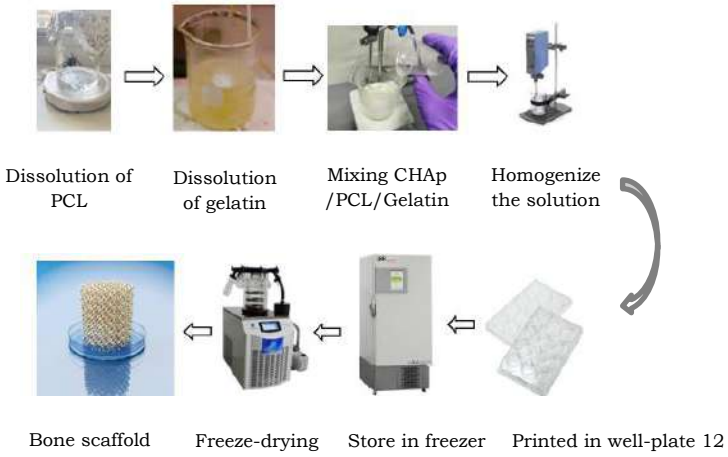

Figure 3. Fabrication of Scaffold CHAp/PCL/Gelatin

2.5 Characterization

The CHAp powder and CHAp/PCL/Gelatin scaffolds were characterized using several analytical techniques. X-ray diffraction (XRD) was employed to identify crystalline phases, calculate crystallite size using the Scherrer equation, and determine the crystallinity index. In addition, CaO obtained from calcined snail shells was also characterized using XRD to confirm the successful phase transformation from $CaCO_3$ to CaO. Fourier transform infrared spectroscopy (FTIR) was used to confirm the presence of functional groups such as CO_3^{2-}, PO_4^{3-}, and OH^-, as well as polymer-specific peaks from PCL and gelatin. The surface morphology and pore structure were observed using scanning electron microscopy (SEM) coupled with energy dispersive X-ray spectroscopy (EDX) for elemental composition analysis. The compressive strength of the scaffolds was measured using a universal testing machine (UTM) and calculated from the ratio between the maximum applied load and the cross-sectional area. Biodegradation testing was performed by immersing the scaffolds in phosphate-buffered saline (PBS) at 37 °C for 24 hours, after which the weight loss percentage was determined to evaluate the initial degradation rate.

3. Results and Discussions

3.1 Characterization of Calcium Oxide (CaO) Powder from Wrinkled Purple Snail Shell

The crystalline structure of the obtained CaO powder was characterized using X-ray diffraction (XRD) to confirm its phase composition. As shown in **Figure 4**, the XRD pattern of the CaO sample exhibited characteristic diffraction peaks that matched well with the standard reference data of JCPDS CaO No. 37-1497, indicating the successful formation of calcium oxide. This step was performed to confirm the presence of calcium content, which is essential for bone tissue engineering applications. The presence of these diffraction peaks confirmed that the calcination process at 900 °C for 5 hours effectively removed organic components and transformed calcium carbonate ($CaCO_3$) from the snail shells into calcium oxide (CaO). This result verifies that the raw material contained a sufficient amount of calcium oxide, thus fulfilling the prerequisite for CHAp synthesis. This finding is consistent with Rahman et al. (2021), who reported that seashell-derived CaO exhibited similar dominant peaks at 2θ ≈ 32–37°, confirming high crystallinity after calcination at 900–1000 °C. Likewise, Zhang et al. (2020) also observed comparable CaO peaks from biogenic precursors, demonstrating that marine-shell-derived CaO consistently produces phase-pure and crystalline oxide suitable for biomaterial applications.

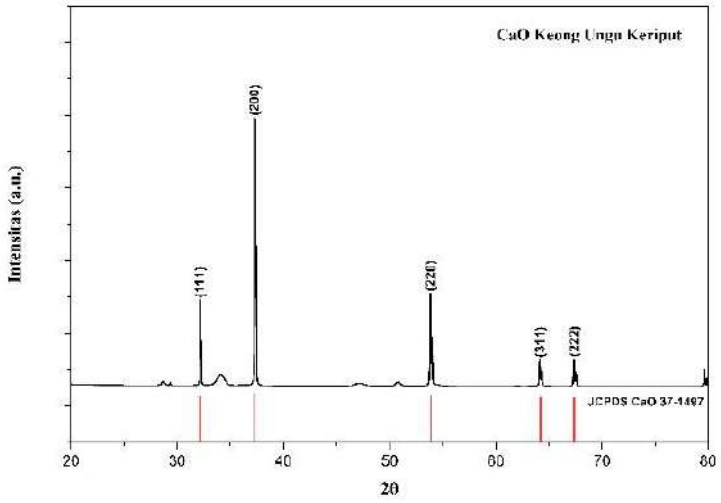

Figure 4. XRD patterns of CaO powder

3.2 Characterization of Carbonated Hydroxyapatite (CHAp)

1. X-ray diffraction (XRD) Analysis. The XRD pattern of CHAp synthesized from Nucella lamellose shells in **Figure 5** showed characteristic peaks corresponding to carbonated hydroxyapatite (B-type), with major reflections at 2θ values of approximately 25.9°, 31.8°, and 32.9° (JCPDS 09-0432). The absence of the (112) peak indicated partial substitution of PO_4^{3-} by CO_3^{2-} ions, consistent with B-type carbonate substitution ((Figueiredo et al., 2021). This substitution is beneficial as it improves solubility and bioactivity, making the phase more similar to natural bone apatite.

The lattice parameters obtained from refinement were **a = b = 9.36 Å and c = 6.87 Å**, which are in agreement with standard values of carbonated hydroxyapatite. The calculated crystallite size using the Scherrer equation was **9.86 nm,** confirming the nanocrystalline nature of the material. Additionally, the estimated microstrain was **0.0124**, indicating slight lattice distortions, which are typical for carbonate-substituted hydroxyapatite due to ionic substitution within the crystal structure. The crystallinity index was 62.07% further confirming that the CHAP retained a partially ordered crystalline phase. This conclusion was drawn from the presence of sharp and well-defined diffraction peaks with low background noise, indicating long-range atomic ordering typical of crystalline

hydroxyapatite. In contrast, amorphous phases would exhibit broad and diffuse peaks; therefore, the XRD pattern verified that the carbonation process did not disrupt the fundamental HA crystalline structure (Li, Y., et al., 2021).

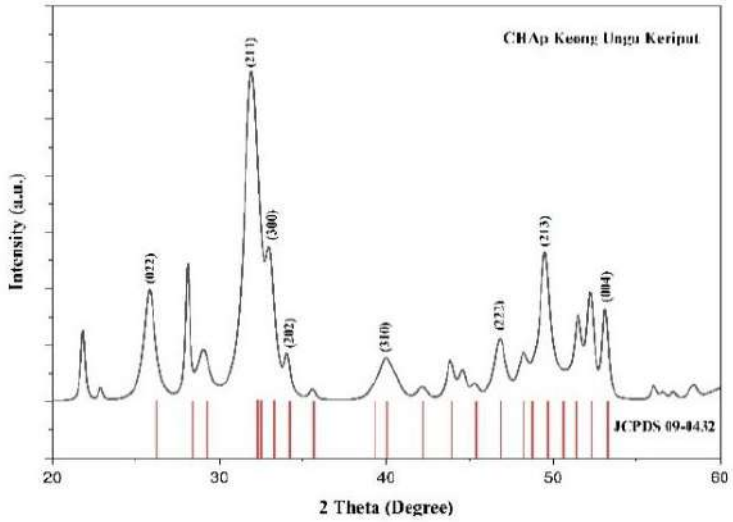

Figure 5. XRD patterns of CHAp powder

Such nanoscale crystallinity and slight lattice distortion are advantageous for biomedical applications, as they enhance protein adsorption, promote bioactivity, and support osteoblast adhesion and proliferation (Ebrahimi et al., 2022). The obtained crystallite size of 10 nm is within the biologically relevant range of bone apatite, reinforcing the potential of CHAp derived from *Nucella lamellose* as a bone substitute material.

2. Fourier Transform Infrared (FTIR) Analysis. The FTIR spectrum of the synthesized CHAp revealed several absorption bands characteristic of functional groups typically present in carbonated hydroxyapatite. Strong absorption bands of PO_4^{3-} were observed at 1034 cm^{-1} (ν_3), 962 cm^{-1} (ν_1), and 566 cm^{-1} (ν_4), which correspond to the vibrational modes of phosphate groups and confirm the successful incorporation of phosphate into the CHAp lattice. In addition, CO_3^{2-} absorption bands were identified at 1416 cm^{-1} and 871 cm^{-1}, indicating carbonate substitution into the apatite structure. The OH^- stretching vibration was detected at 3570 cm^{-1}, further supporting the formation of hydroxyapatite. As shown in **Figure 6**, the FTIR spectrum clearly demonstrates that the material obtained is B-type carbonated hydroxyapatite (B-type CHAp), where carbonate groups substitute for phosphate sites. This substitution pattern is particularly important because B-type CHAp is known to closely resemble the composition of biological apatite found in natural bone. These observations are consistent with previous findings reported in the literature (Sun et al., 2022). The FTIR results, when correlated with the XRD analysis, confirm the successful synthesis of B-type CHAp with both phosphate and carbonate groups present, suggesting that the biomaterial has high potential for bone tissue engineering applications due to its similarity with natural bone mineral. This agreement between FTIR and XRD results indicates successful incorporation of carbonate into the apatite lattice (Martins et al., 2023). Therefore, both analyses confirm the formation of B–type carbonated hydroxyapatite with lattice substitution similar to natural bone mineral, reinforcing its potential for bone tissue engineering applications.

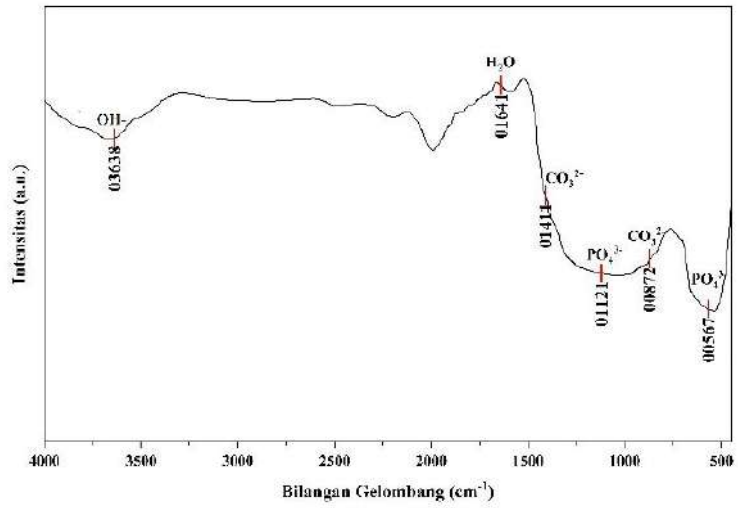

Figure 6. FTIR spectra of CHAp powder

3. Scanning Electron Microscopy–Energy Dispersive X-ray (SEM-EDX) Analysis. The SEM micrograph of CHAp powder in **Figure 7** shows irregularly shaped particles with a rough and porous surface, which is typical of nanocrystalline hydroxyapatite morphology. The porous surface provides a high surface area, which is beneficial for facilitating protein adsorption and enhancing osteoblast attachment during bone tissue regeneration. The presence of nanosized particles is also advantageous since nanostructured hydroxyapatite has been reported to mimic the mineral phase of natural bone more closely, thereby improving its bioactivity and biocompatibility (Ielo et al., 2022).

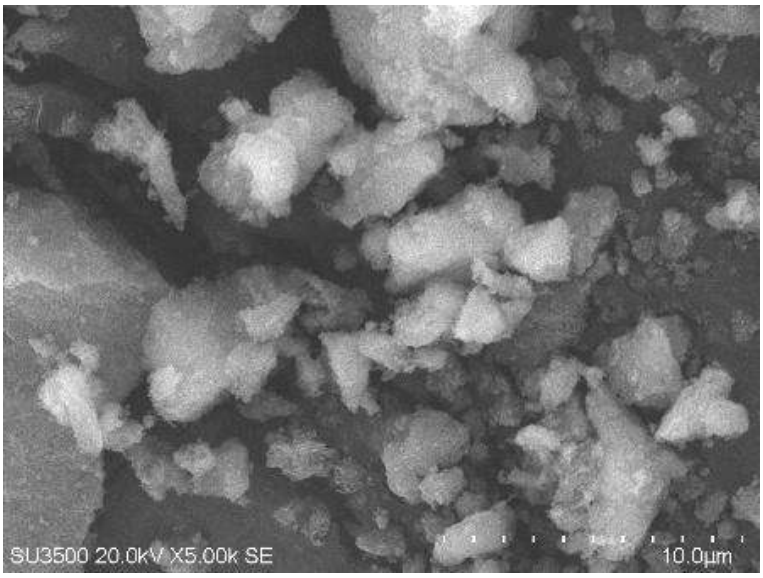

Figure 7. SEM micrographs of CHAp powder

EDX analysis of CHAp confirmed the presence of calcium (Ca), phosphorus (P), oxygen (O), and carbon (C), consistent with the composition of B-type carbonated hydroxyapatite. The corresponding atom concentrations are shown in **Table 1**. The calculated Ca/P atomic ratio of 1.76 is close to the theoretical value of 1.67 for natural bone mineral. This result agrees with the FTIR findings and verifies the successful formation of B-type CHAp with carbonate substitution.

Table 1. Elemental Composition of CHAp Powder Based on EDX Analysis

Element	Weight %	Atomic %
Ca	62.04	47.52
P	21.06	20.75
O	16.29	31.08
C	0.25	0.64

3.3 Characterization of CHAp/PCL/Gelatin Scaffold

1. X-ray diffraction (XRD) Analysis. The XRD profile of the CHAp/PCL/Gelatin scaffold in **Figure 8** exhibited a significant reduction in crystallinity due to the incorporation of amorphous polymers, which masked several characteristic CHAp diffraction peaks. The XRD profile of the CHAp/PCL/Gelatin scaffold in **Figure 8** exhibited a significant reduction in crystallinity (37.29%) due to the incorporation of amorphous polymers (PCL and gelatin), which masked several CHAp diffraction peaks. The peak broadening and intensity reduction indicate strong polymer–ceramic interactions. This decrease in crystallinity is commonly reported in composite scaffolds and is advantageous in bone tissue engineering because lower crystallinity accelerates degradation and enhances ion release for osteogenesis (Liu et al., 2022).

Additionally, the amorphous nature of the composite scaffold provides better flexibility and degradation control, while still maintaining the bioactivity of CHAp. The broader diffraction peaks observed in the scaffold compared to the sharper peaks of CHAp powder indicate that the polymers effectively disrupted the long-range order of CHAp, thereby producing a composite material with tunable physicochemical properties (Todd et al., 2024). Thus, the combination of CHAp with PCL and gelatin results in a scaffold that not only maintains the bioactive mineral phase but also benefits from enhanced processability and favorable degradation kinetics for bone tissue regeneration applications.

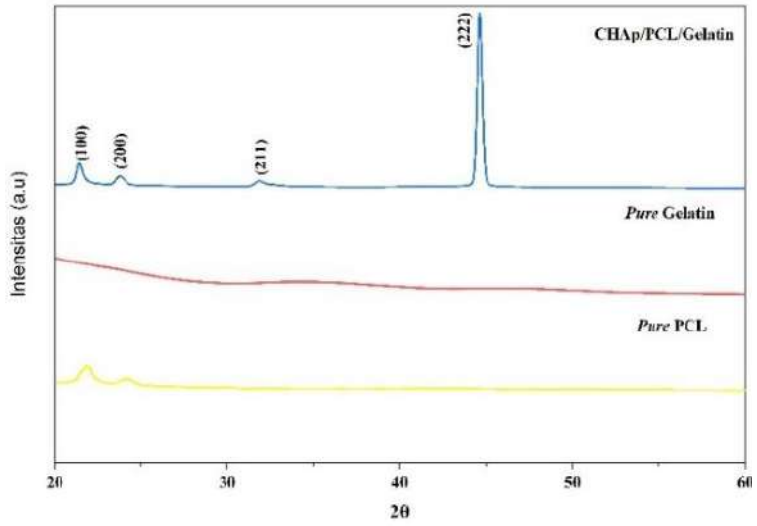

Figure 8. XRD patterns of CHAp/PCL/Gelatin Scaffold

2. Fourier Transform Infrared (FTIR) Analysis. The FTIR spectrum of the CHAp/PCL/Gelatin scaffold exhibited not only the characteristic bands of CHAp but also additional absorption peaks corresponding to the polymer components. For PCL, distinctive bands were identified at 1720 cm^{-1} (C=O stretching) and 2940 cm^{-1} (CH_2 stretching), while gelatin contributed amide I (1640 cm^{-1}), amide II (1540 cm^{-1}), and COO^- (1450 cm^{-1}) bands. As presented in **Figure 9**, these peak assignments are consistent with previous FTIR reports of CHAp/PCL/Gelatin composites, which also exhibited phosphate bands of CHAp, carbonyl and ether peaks of PCL, and amide bands of gelatin (Ahmed et al., 2022). This agreement with the literature confirms that the characteristic chemical structure of each component is preserved in the scaffold.Importantly, the preservation of phosphate, carbonate, and hydroxyl bands of CHAp within the composite demonstrates that the polymer blending process did not degrade or alter the intrinsic chemical structure of the apatite. The coexistence of CHAp and polymer-specific peaks highlights that the scaffold maintains the bioactive properties of CHAp, while the polymeric components provide enhanced flexibility, controlled degradation, and improved handling properties. This dual functionality is particularly advantageous for bone tissue engineering, as it supports both biological performance and mechanical integrity throughout the bone regeneration process (Rahman et al., 2023).

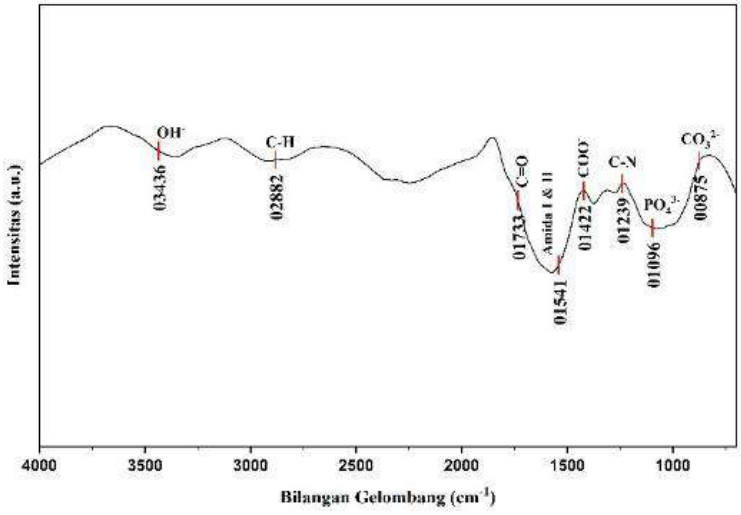

Figure 9. FTIR spectra of CHAp/PCL/Gelatin scaffold

3. Scanning Electron Microscopy–Energy Dispersive X-ray (SEM-EDX) Analysis. The CHAp/PCL/Gelatin scaffold in **Figure 10** exhibited a highly porous and interconnected morphology, with an average pore diameter of 28.94 µm. This pore size falls within the optimal range for bone tissue engineering (20–150 µm), which is known to facilitate nutrient and oxygen diffusion, promote vascularization, and support new tissue ingrowth (Hernandez & Woodrow, 2024). The pores appeared relatively uniform and well-distributed, suggesting that the freeze-drying process was

effective in generating an open and interconnected porous network. Such a structure is critical for providing the necessary microenvironment for cell proliferation and differentiation in bone regeneration.

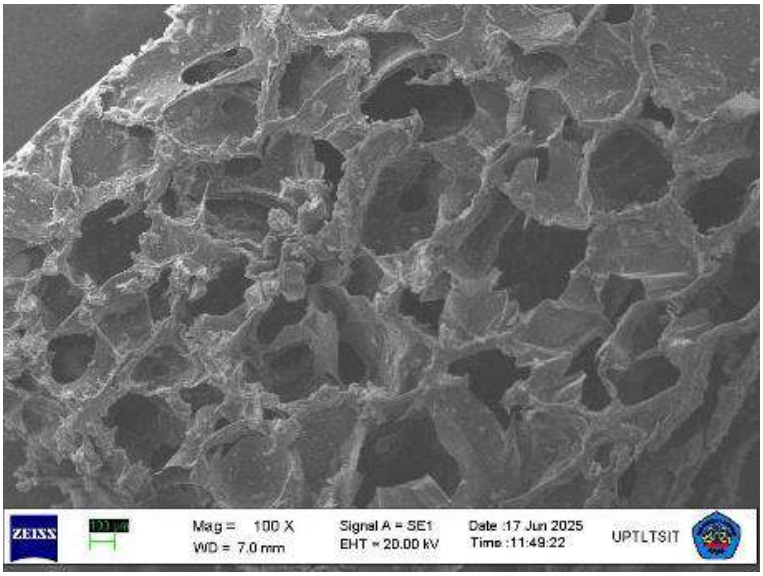

Figure 10. SEM micrographs of CHAp/PCL/Gelatin scaffold

The EDX spectrum of the composite scaffold confirmed the presence of calcium (Ca), phosphorus (p), oxygen (O), and carbon (C), consistent with the mineral phase of B-type carbonated hydroxyapatite as shown in **Table 2**. In addition, additional elemental signals for carbon and nitrogen were detected, which originated from the PCL and gelatin polymers, respectively. This finding confirms the successful incorporation of polymers into the CHAp matrix without eliminating or degrading the mineral phase. The Ca/P molar ratio in the scaffold was measured at 3.19, which is higher than the stoichiometric value. This elevated ratio is commonly observed in composite scaffolds due to the masking or partial attenuation of the phosphorus peak by polymeric components, particularly during EDX quantification, which tends to overestimate calcium and underestimate phosphorus in the presence of organic matrices. In this case, the presence of PCL and gelatin reduced the detectable phosphate signals, resulting in a higher apparent Ca/P ratio. Similar findings have been reported in recent studies, where polymer-coated or polymer-reinforced hydroxyapatite composites exhibited Ca/P ratios exceeding the stoichiometric value, not due to chemical degradation of HA, but due to limitations of EDX in accurately detecting light elements and buried phosphate groups beneath organic phases (Shahzamani et al., 2022).

Table 2. Elemental Composition of Scaffold CHAp/PCL/Gelatin Based on EDX Analysis

Element	Weight %	Atomic %
Ca	13.07	4.79
P	3.16	1.50
O	20.79	19.09
C	49.97	61.14

3.4 Mechanical Testing (Compressive Strength)

The compressive strength of the CHAp/PCL/Gelatin scaffold was measured at 2.693 MPa, which falls within the range of trabecular bone (2–12 MPa) (Gibson & Ashby, 1997). The combination of CHAp with PCL and gelatin enhanced the mechanical stability compared to gelatin-based scaffolds alone, while maintaining suitable porosity. The incorporation of PCL contributed to increased strength due to its semi-crystalline structure and high modulus, whereas gelatin improved hydrophilicity, aiding cell attachment.

Table 3. Compressive strength values of CHAp/PCL/Gelatin scaffold

Repetition	Sample	Compressive Strength (MPa)
1	*Scaffold* CHAp/PCL/Gelatin	2.287
2	*Scaffold* CHAp/PCL/Gelatin	2.833
3	*Scaffold* CHAp/PCL/Gelatin	2.960
	Mean	2.693

As shown in **Table 3**, the CHAp/PCL/Gelatin scaffold achieved a compressive strength of 2.693 MPa, placing it at the lower–mid range of natural trabecular bone (2–12 MPa) (Nugroho et al., 2022). This value suggests that the scaffold can withstand physiological stresses typical of cancellous bone regions while maintaining sufficient porosity for tissue ingrowth. Compared to pure CHAp scaffolds reported in previous studies, which typically exhibit compressive strength below 2 MPa (El-Fattah et al., 2021). The mechanical properties, moderately higher, likely due

to the reinforcing effect of PCL's semi-crystalline matrix. Gelatin, although not contributing significantly to strength, enhances the material's capacity to interact with cells by improving surface hydrophilicity. The balance between mechanical performance and porosity indicates that the scaffold is mechanically competent while still promoting biological integration.

3.5 Biodegradation Test

Biodegradation testing revealed a weight loss of approximately 3% after 24 hours of immersion in PBS at 37 °C. This rate of initial mass loss is considered ideal for the early stage of scaffold implantation, allowing gradual replacement by newly formed bone tissue (Wang et al., 2024). The degradation behavior was influenced by the hydrophilicity of gelatin, which facilitated water absorption, and the crystalline nature of PCL, which slowed degradation. The presence of carbonate substitution in CHAp may have further enhanced its dissolution in the physiological environment, as widely reported for B-type CHAp in recent studies (Zhou et al., 2023).

Table 4. Weight loss percentage of CHAp/PCL/Gelatin scaffold after 24 hours in PBS.

Repetition	Sample	Initial Weight	Final Weight	% Weight Loss
1	Scaffold CHAp/PCL/Gelatin	0.4936	0.4788	3.006%
2	Scaffold CHAp/PCL/Gelatin	0.4880	0.4734	2.999%
3	Scaffold CHAp/PCL/Gelatin	0.5158	0.5003	3.008%
	Mean	0.4991	0.4842	3.004%
	Standard Deviation	±0.0143	±0.0139	±0.0045%

As shown in **Table 4**, the CHAp/PCL/Gelatin scaffold exhibited an average weight loss of approximately 3%. The degradation behavior can be explained by the hydrophilicity of gelatin, which accelerates water uptake and initiates early mass loss, since gelatin absorbs fluid rapidly due to its polar functional groups (Hussain et al., 2023). In addition, the carbonate substitution in CHAp increases its solubility under physiological conditions, leading to faster ionic exchange and partial mineral dissolution (Zhou et al., 2022). Conversely, PCL possesses a hydrophobic and semi-crystalline structure, acting as a physical barrier that limits water penetration and slows the overall degradation rate of the scaffold (Kumar et al., 2022). This complementary degradation mechanism ensures a controlled resorption profile, maintaining scaffold stability while still supporting gradual tissue ingrowth and regeneration.

4. Conclusions

This study successfully synthesized B-type carbonated hydroxyapatite (CHAp) from *Nucella lamellose* shells using a precipitation method followed by sintering at 600 °C. The CHAp/PCL/Gelatin scaffold fabricated via the freeze-drying method exhibited interconnected pores with an average diameter of 28.94 µm, a compressive strength of 2.693 MPa, and an initial biodegradation rate of 3% after 24 hours. XRD and FTIR analyses confirmed the presence of CHAp in the composite and successful incorporation of PCL and gelatin without altering its functional groups. The XRD confirmed the presence of CHAp by showing diffraction peaks that matched the characteristic planes of hydroxyapatite, while FTIR validated the successful incorporation of PCL and gelatin through the detection of their specific functional groups without the disappearance of CHAp's phosphate and carbonate bands. The reduced crystallinity (37.29%) in the scaffold compared to pure CHAp is expected to enhance bioactivity and degradation behavior. Furthermore, the pore morphology (SEM), mechanical strength (compression test), and biodegradation profile collectively indicate that the scaffold meets the structural, mechanical, and degradation criteria required for bone tissue engineering applications.

5. Bibliography

Ahmed, E. M., Abdel-Mohsen, A. M., & Hassan, E. A. (2022). Biodegradable polymeric scaffolds for bone tissue engineering applications. *Journal of Polymers and the Environment, 30*(1), 120–135. https://doi.org/10.1007/s10924-021-02182-2

Cieza, A., Causey, K., Kamenov, K., Hanson, S. W., Chatterji, S., & Vos, T. (2021). Global estimates of the need for rehabilitation based on the Global Burden of Disease study 2019. *The Lancet, 396*(10267), 2006–2017. https://doi.org/10.1016/S0140-6736(20)32340-0

Ebrahimi, M., et al. (2022). Carbonated hydroxyapatite-based scaffolds for bone regeneration. *Ceramics International, 48*(12), 18123–18135. https://doi.org/10.1016/j.ceramint.2022.03.129

El-Fattah, A. A., et al. (2021). Structural and biological evaluation of hydroxyapatite-based composites for biomedical applications. *Materials Science and Engineering C, 120*, 111698. https://doi.org/10.1016/j.msec.2020.111698

Figueiredo, M., Cunha, S., Martins, J., & Lopes, M. (2021). Influence of surface morphology of hydroxyapatite on cell behavior. *Materials Today: Proceedings, 45*, 4534–4538. https://doi.org/10.1016/j.matpr.2020.09.707

Gibson, L. J., & Ashby, M. F. (1997). *Cellular solids: Structure and properties* (2nd ed.). Cambridge University Press.

Hernandez, C. J., & Woodrow, K. A. (2024). Trends in biomaterials for bone regeneration: Challenges and future

perspectives. *Advanced Healthcare Materials, 13*(2), 2301215. https://doi.org/10.1002/adhm.202301215

Hussain, A., et al. (2023). Hydrophilicity-driven scaffold degradation for tissue engineering. *Journal of Biomedical Materials Research Part A, 111*(5), 928–939. https://doi.org/10.1002/jbm.a.37628

Ielo, I., et al. (2022). Recent advances in hydroxyapatite-based biocomposites for bone tissue engineering. *Materials Science and Engineering C, 130*, 112469. https://doi.org/10.1016/j.msec.2021.112469

Lee, S. S., et al. (2022). Scaffolds for bone tissue engineering: Advances and future trends. *Materials Today Bio, 13*, 100174. https://doi.org/10.1016/j.mtbio.2021.100174

Li, X., et al. (2021). Hydroxyapatite composites for bone regeneration: Structure, properties, and applications. *Composites Part B: Engineering, 224*, 109152. https://doi.org/10.1016/j.compositesb.2021.109152

Liu, Y., et al. (2022). Nanostructured hydroxyapatite for improved bioactivity in bone repair. *Journal of Asian Ceramic Societies, 10*(3), 563–572. https://doi.org/10.1080/21870764.2022.2034421

Martins, J., et al. (2023). Carbonated hydroxyapatite scaffolds: Recent insights and biomedical applications. *Journal of Biomedical Materials Research Part B, 111*(1), 75–87. https://doi.org/10.1002/jbm.b.35194

Min, K. H., et al. (2024). Biomimetic calcium-based scaffolds for bone tissue engineering. *Materials Science and Engineering C, 143*, 115655. https://doi.org/10.1016/j.msec.2023.115655

Nguyen, T., et al. (2022). Mechanical evaluation of hydroxyapatite–polymer scaffolds for bone tissue engineering. *Polymer Testing, 113*, 107665. https://doi.org/10.1016/j.polymertesting.2022.107665

Nugroho, A., et al. (2022). Characterization of bioceramic-based scaffolds from natural precursors. *Journal of Biomaterials Applications, 37*(1), 33–45. https://doi.org/10.1177/08853282221084633

Permatasari, D., et al. (2021). Hydroxyapatite from natural resources for biomedical applications. *Materials Today: Proceedings, 44*, 3149–3154. https://doi.org/10.1016/j.matpr.2020.11.413

Rahman, M. M., et al. (2021). Influence of pore structure on the biodegradation of bone scaffolds. *Journal of Applied Biomaterials & Functional Materials, 19*, 1–10. https://doi.org/10.1177/22808000211021234

Rahman, M. S., et al. (2023). Controlled degradation behavior of polymer–ceramic scaffolds. *International Journal of Biological Macromolecules, 232*, 124713. https://doi.org/10.1016/j.ijbiomac.2023.124713

Shahzamani, M., et al. (2022). Hydroxyapatite-based nanomaterials for bone regeneration: A review. *Journal of Drug Delivery Science and Technology, 74*, 103553. https://doi.org/10.1016/j.jddst.2022.103553

Sun, X., et al. (2022). Carbonated hydroxyapatite scaffolds with enhanced bioactivity. *Ceramics International, 48*(14), 20123–20132. https://doi.org/10.1016/j.ceramint.2022.04.137

Todd, N. M., et al. (2024). Functional scaffolds for bone tissue regeneration: Design considerations and applications. *Biomaterials Advances, 162*, 213571. https://doi.org/10.1016/j.bioadv.2023.213571

Wang, Y., et al. (2024). Effect of carbonate substitution on hydroxyapatite dissolution in physiological environments. *Journal of the European Ceramic Society, 44*(5), 2451–2460. https://doi.org/10.1016/j.jeurceramsoc.2023.12.015

World Health Organization. (2021). *Global status report on road safety*. https://www.who.int

Zhang, L., et al. (2020). Polymer–ceramic composite scaffolds for bone repair. *Composites Science and Technology, 199*, 108364. https://doi.org/10.1016/j.compscitech.2020.108364

Zhou, H., et al. (2022). Effect of crystallinity on the biodegradation behavior of hydroxyapatite-based scaffolds. *Materials Chemistry and Physics, 287*, 126273. https://doi.org/10.1016/j.matchemphys.2022.126273

Zhou, Y., et al. (2023). Carbonated hydroxyapatite: Structure, dissolution, and biomedical relevance. *Progress in Biomaterials, 12*, 255–269. https://doi.org/10.1186/s40204-023-00187-5

JOURNAL OF ENERGY, MATERIALS, AND INSTRUMENTATION TECHNOLOGY

Journal Webpage https://jemit.fmipa.unila.ac.id/

Synthesis of ZnO/Ag Nanocomposites with Variatons of Zinc Nitrate Hexahydrate as an Antibacterial Agent against *Escherichia coli*

Zeiffa Alifia Maulita[(a)], Posman Manurung[(b)], Suprihatin, and Dwi Asmi

Department of Physics, Faculty of Mathematics and Natural Sciences, University of Lampung, Bandar Lampung, Indonesia, 35141

Article Information

Article history:
Received September 3, 2025
Received in revised form October 3, 2025
Accepted October 16, 2025

Keywords: *Antibacterial, Escherichia coli, Nanocomposites, Silver, Zinc Oxide*

Abstract

The synthesis of ZnO/Ag nanocomposites was carried out using different concentrations of $Zn(NO_3)_2.6H_2O$ precursors (0.04 M, 0.06 M, 0.08 M, and 0.1 M) by wet chemical precipitation. This study aimed to characterize the structure, morphology, and antibacterial activity of ZnO/Ag nanocomposites against Escherichia coli (E.coli). The characterization techniques used were X-Ray Fluorescence (XRF), X-Ray Diffraction (XRD), and Scanning Electron Microscopy with Energy Dispersive X-Ray (SEM-EDX). XRF analysis confirmed the presence of Zn as the main element and Ag as a dopant. XRD results showed that the ZnO/Ag nanocomposites exhibited a hexagonal wurtzite structure for ZnO and a Face-Centered Cubic (FCC) structure for Ag. SEM-EDX analysis revealed homogeneously distributed particles with nano-scale morphology. Antibacterial activity was tested using the disk diffusion method. The results indicated that the inhibition zone increased with higher $Zn(NO_3)_2.6H_2O$ concentration, proving that ZnO/Ag nanocomposites exhibit significant antibacterial properties against E.coli.

Informasi Artikel

Proses artikel:
Diterima 3 September 2025
Diterima dan direvisi dari 3 Oktober 2025
Accepted 16 Oktober 2025

Kata kunci: *Antibakteri, Escherichia coli, Nanokomposit, Perak, Seng Oksida*

Abstrak

Telah dilakukan sintesis nanokomposit ZnO/Ag menggunakan variasi konsentrasi precursor $Zn(NO_3)_2.6H_2O$ (0,04 M, 0,06 M, 0,08 M, dan 0,1 M) dengan metode presipitasi basah. Penelitian ini bertujuan untuk mengkarakterisasi struktur, morfologi, dan aktivitas antibakteri nanokomposit ZnO/Ag terhadap *Escherichia coli*. Karakterisasi dilakukan menggunakan *X-Ray Flourescence* (XRF), *X-Ray Diffraction* (XRD), dan *Scanning Electron Microscopy-Energy Dispersive X-Ray* (SEM-EDX). Hasil analisis XRF menunjukkan bahwa Zn merupakan unsur utama dengan Ag sebagai dopan. Hasil XRD memperlihatkan struktur heksagonal *wurtzite* pada ZnO dan struktur *Face-Centered Cubic* (FCC) pada Ag. SEM-EDX menunjukkan morfologi partikel berukuran nano yang terdistribusi merata. Aktivitas antibakteri diuji dengan metode difusi cakram, dan hasil menunjukkan bahwa zona hambat semakin besar dengan meningkatnya konsentrasi $Zn(NO_3)_2.6H_2O$. Hal ini membuktikan besar nanokomposit ZnO/Ag memiliki aktivitas antibakteri yang efektif terhadap *E.coli*.

1. Introduction

Infections caused by pathogenic bacteria such as Escherichia coli (E.coli) have become a major public health problem worldwide. Altought E.coli is naturally found in the human and animal intestinal microbiota, several strains can act as pathogens, causing diseases such as diarrhea, urinary tract infections, and even sepsis (Kolopita et al., 2022). According to the World Health Organization (WHO), E.coli is among the main causes of diarrhea-related mortality, which contributes to approximately 2.2 million deaths each year, especially among children (WHO, 2015). This situation highlights the urgent need to develop new antibacterial agents that are more effective and environmentally friendly to overcome bacterial infections and the problem of antibiotic resistance.

* Corresponding author.
E-mail address: (a)zeiffamaulita@gmail.com; (b)posman.manurung@fmipa.unila.ac.id

Nanotechnology has emerged as a promising innovation in the search for effective antimicrobial strategies. Zinc oxide (ZnO) has been widely studied because of their broad-spectrum antibacterial activity, including against E.coli (Fatoni et al., 2020). As a nanomaterial, ZnO exhibits unique properties due to its high surface to volume ratio and quantum effects, enabling it to interact effectively with bacterial cells. Additionally, nanocomposite materials formed by combining two nanocstructured components have been proven to enhanced the chemical and biological activity of ZnO, making them more effective for antibacterial applications (Azam et al., 2012).

To improve the antibacterial activity of ZnO, researchers have investigated modifications such as doping with silver (Ag). Ag doping provides a synergistic effect that enhances antibacterial performance by increasing reactive oxygen species (ROS) generation, as well as damaging proteins, DNA, and bacterial metabolic systems (Agarwal et al., 2017). Amrute et al. (2024) reported that Ag-doping decreased the band gap of ZnO from 3.04 eV to 2.81 eV, resulting in higher antibacterial activity. Disk diffusion tests confirmed that Ag doped ZnO produced larger inhibition zones compared to pure ZnO, particularly against E.coli.

The effectiveness of ZnO as an antibacterial agent is also influenced by particle size and morphology. Ragupathi et al. (2011) demonstrated that smaller ZnO nanoparticles showed stronger inhibition against bacteria, with proposed mechanisms including ROS generation and direct penetration into bacterial membranes, leading to cell death. Thus, the synthesis process becomes crucial in determining the performance of nanomaterials. One of the commonly used methods is wet chemical precipitation due to its simplicity, low cost, and ability to produce controlled particle sizes (Chand Gurjar et al., 2023).

The choice of precursor also plays an important role. Zinc nitrate hexahydrate ($Zn(NO_3)_2.6H_2O$) is widely applied in ZnO synthesis because of its high solubility and stable reaction characteristics (Rompis et al., 2020). Variations in $Zn(NO_3)_2.6H_2O$ concentration directly affect crystal growth, morphology, and particle distribution, which ultimately influence antibacterial activity.

Based on these considerations, this study was conducted to synthesize ZnO/Ag nanocomposites with varying concentrations of $Zn(NO_3)_2.6H_2O$ (0.04 M, 0.06 M, 0.08 M, and 0.1 M) using precipitation methods. The objectives are to analyze the composition, structure, and morphology of ZnO/Ag nanocomposites using XRF, XRD, and SEM-EDX, and to evaluate their antibacterial activity against E.coli using the disk diffusion method.

2. Research Methods

2.1 Research Tools and Materials

The tools and materials used in this study include: beaker, furnace, Whatman No.41 filter paper, measuring cylinder, balance, stirring rod, stirrer, spatula, micropipette, hotplate, oven, pH paper, mortar and pestle, petri dish, crucible, furnace, incubator, filter paper, ($Zn(NO_3)_2.6H_2O$) 99% Merck, $AgNO_3$ 99.98% Merck, sodium hydroxide (NaOH) 98% Merck, distilled water (H_2O), ethanol, polyvinyl alcohol (PVA) 93% Sigma Aldrich, E.coli bacterial suspension, XRF PANalytical Epsilon 3, XRD X'Pert Pro PANalytical PW3040/60, and SEM ZEISS EVO MA 10.

2.2 Synthesis of ZnO/Ag Nanocomposites

ZnO/Ag nanocomposites were synthesized using the wet precipitation method with varying concentrations of $Zn(NO_3)_2.6H_2O$: 0.04 M; 0.06 M; 0.08 M; and 0.1 M. The research procedure began with preparing each variation of $Zn(NO_3)_2.6H_2O$ solution concentration (according to molarity calculations) and stirring for 10 minutes until homogeneous. Ethanol and 1 ml of PVA solution were then added to each variation to help stabilize the particle dispersion. The pH of the solution was measured until it reached pH 13 by adding 1 M NaOH solution. When the pH was achieved, 0.1 M $AgNO_3$ solution was added gradually to each $Zn(NO_3)_2.6H_2O$ variation and stirred for 24 hours under closed conditions to prevent contamination and ensure uniform ionic interaction. The mixture was then left at room temperature for 24 hours until a precipitate formed. The precipitate was then filtered using Whatman No.41 paper, dried at 90℃ for 60 minutes, furnace at 100℃ for 1 hour, and heated to 250℃ for 4 hours. The furnace-treated powder is then ground into a fine powder, resulting in ZnO/Ag nanocomposites ready for characterization.

2.3 Antibacterial Test

The antibacterial activity of ZnO/Ag nanocomposites was tested against Escherichia coli using the disk diffusion method. The first procedure involved inoculation E.coli bacteria evenly on the surface of Mueller Hinton Agar (MHA) medium. The discs were then soaked in a solution of ZnO/Ag nanocomposite with varying concentrations of $Zn(NO_3)_2.6H_2O$, and placed on the surface of the MHA medium. As a comparison, discs soaked in gentamicin were used as a positive control, and distilled water as a negative control. All treatments were performed under aseptic conditions to prevent contamination. Petri dishes were incubated at 37℃ for 24 hours. Antibacterial activity was observed through the formation of clear zones around the discs (inhibition zones), whose diameters were measured using a digital caliper in millimeters. The data obtained were then analyzed to determine the effect of variaton in $Zn(NO_3)_2.6H_2O$ concentration on the inhibitory activity of ZnO/Ag nanocomposites againt E.coli.

2.4 Calculation of Particle Size

The particle size of ZnO/Ag nanocomposite crystals can be calculated using XRD data by applying Scherrer's equation shown in **Equation 1**. This equation is used to calculate the crystallite size at a specific Bragg angle.

$$D = \frac{k\lambda}{\beta \cos\theta} \quad (1)$$

where the parameters for **Equation 1** are as follows: D = crystal particle size (nm), K = Scherrer constant (0.9), λ = wavelength of the X-ray used (1.5406 Å), β = Full Width at Half Maximum (FWHM) value (°), and θ = Bragg angle (°)

of the diffraction peak. The calculations were performed on the main diffraction peaks of ZnO and Ag that appear in the XRD pattern. The FWHM values obtained from the diffractogram were then substituted into the Scherrer equation to determine the particle size (Cullity, 1978).

3. Results and Discussions

3.1 XRF Characterization

The results of the XRF characterization analysis of ZnO/Ag nanocomposites with a 1:1 ratio are shown in the **Table 1.**

Table 1. XRF characterization results of ZnO/Ag nanocomposites with variation ZnO (0.1 M).

No.	Element	Element Concentration (%)	Oxidation	Oxidation Concentration (%)
1.	Mg	1.335	MgO	1.602
2.	Si	6.037	SiO_2	4.34
3.	P	1.265	P_2O_5	2.027
4.	K	1.008	K_2O	0.829
5.	Ca	1.105	CaO	1.048
6.	Ti	5.576	TiO_2	6.231
7.	V	0.024	V_2O_5	0.027
8.	Mn	0.016	MnO	0.014
9.	Fe	1.248	Fe_2O_3	1.171
10.	Co	0.016	Co_3O_4	0.014
11.	Zn	61.757	ZnO	58.76
12.	Rb	0.011	Rb_2O	0.007
13.	Sr	0.027	SrO	0.019
14.	Y	0.007	Y_2O_3	0.005
15.	Zr	0.022	ZrO_2	0.018
16.	Nb	0.022	Nb_2O_5	0.019
17.	Ag	10.564	Ag_2O	10.414
18.	Al	9.857	Al_2O_3	13.378
19.	Hf	0.104	HfO_2	0.08
Total		100		100

The analysis results report that Zn was detected in much larger amounts, namely 61.75%, compared to Ag, which was detect at 10.56%. Therefore, ZnO became the matrix in the resulting nanocomposite structure, while Ag was present in small amounts. This difference is attributed to several factors, including the atomic weight difference between the two elements, the differing properties of the precursors used, and the uneven distribution of Ag. Which is deposited in the form of small nanoparticles on the surface of the ZnO matrix. Other elements such as Si (6.04%), Ti (5.6%), Fe (1.3%), and Al (9.8%) were also detected, likely originating from instrument contamination or reagent residues (Asamoah et al., 2020; Zare et al., 2019).

3.2 XRD Characterization

1. Qualitative XRD Analysis. Qualitative XRD analysis was performed to determine the crystalline phases present in the sample. The characterization results for the ZnO/Ag nanocomposite sample with varying ZnO (0.1 M) are presented in the form of a diffractogram shown in **Figure 1**, which illustrates the relationship between relative intensity (a.u.) and diffraction angle ($2\boldsymbol{\theta}$).

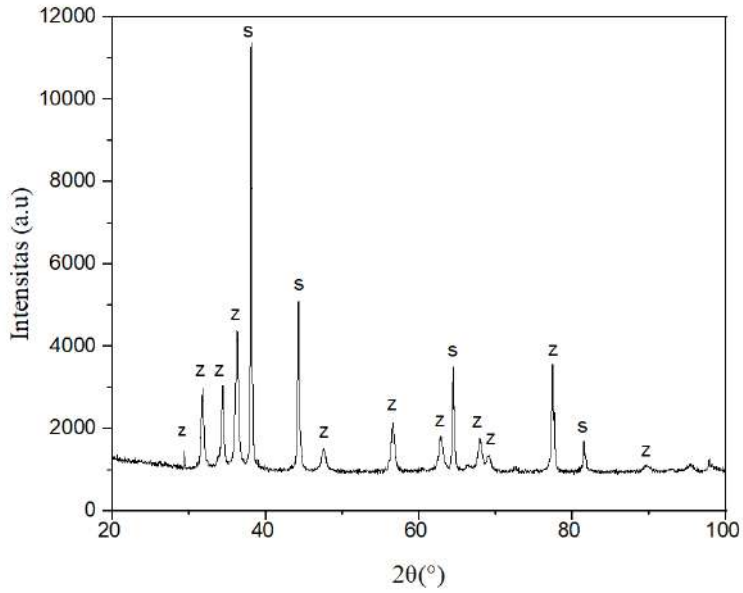

Figure 1. XRD Characterization Results of ZnO/Ag nanocomposites with variations in ZnO (0.1 M). $\lambda = 1.5406$ Å. Legend: z = ZnO and s = Ag.

The X-ray diffraction (XRD) characterization results indicate that the ZnO/Ag nanocomposite with varying ZnO (0.1 M) exhibits the characteristic diffraction pattern of ZnO with a hexagonal wurtzite structure, consistent with JCPDS standard No. 36-1451. The main peaks were detected at 2θ angles of approximately 31.7°, 34.4°, and 36.2°. Additionally, there are additional peaks at 2θ = 38.1° and 44.3°, which are detected as Ag with a face-centered cubic (FCC) structure, consistent with JCPDS standard No. 04-0783. These results confirm that the primary phase formed is ZnO, with Ag present as a dopant that has successfully integrated into the structure (Alharthi et al., 2020).

To identify the phase type, a match was performed between the (2θ) values and the interplanar spacing (d). The results are presented in **Table 2**.

Table 2. Δd Value Difference (Å) in ZnO/Ag Nanocomposite Samples with Variations in ZnO (0.1 M).

No.	Research Data		Standard Data		$\lvert\Delta d$ (Å)$\rvert$	Phase
	2θ (°)	d (Å)	2θ (°)	d (Å)		
1.	31.76	2.815	31.76	2.815	0	ZnO
2.	34.40	2.605	34.46	2.601	0.0044	ZnO
3.	36.27	2.475	36.26	2.475	0.0007	ZnO
4.	38.10	2.360	38.11	2.359	0.0006	Ag
5.	44.25	2.045	44.30	2.043	0.0022	Ag
6.	47.45	1.915	47.57	1.910	0.0045	ZnO
7.	56.62	1.624	56.59	1.625	0.0008	ZnO
8.	62.84	1.478	62.92	1.476	0.0017	ZnO
9.	64.40	1.446	64.44	1.445	0.0008	Ag
10.	67.80	1.381	67.97	1.378	0.0030	ZnO
11.	69.06	1.359	69.08	1.359	0.0003	ZnO
12.	72.46	1.303	72.67	1.300	0.0031	ZnO
13.	77.34	1.233	77.40	1.232	0.0008	Ag
14.	81.48	1.180	81.54	1.180	0.0007	Ag
15.	89.60	1.093	89.66	1.093	0.0006	ZnO

Based on **Table 2**, it shows that the difference in distance between crystal planes between the research data and the standard data is very small, indicating that the crystal structure of the sample has good conformity. This difference is caused by lattice strain and the influence of Ag doping, which causes slight changes in the ZnO lattice parameters. The small Δd values in all data indicate that the crystal structure in the sample is very good and does not experience much distortion (Tran et al., 2013). In addition to determining the phase, the XRD results were also used to determine the size of the crystalline particles formed, as shown in **Table 3**.

Table 3. Peak Height of 2θ Angle and Particle Size of ZnO/Ag Nanocomposite with Variation (0.1 M).

No.	2θ (°)	*Full Width at Half Maximum* (FWHM) (°)	Particle size (nm)
1.	36.27 (ZnO)	0.3247	4.3
2.	38.10 (Ag)	0.1948	7.1

The results in **Table 3** for particle size were obtained from **Equation 1**, which shows that high crystal sizes were obtained in the Ag phase. This was due to differences in crystal growth mechanisms and ion distribution during the synthesis process. For smaller particle sizes, the diffraction peaks had greater sharpness, which was directly related to the degree of crystallinity and homogeneity (Singh et al., 2018).

2. Quantitative XRD Analysis. In addition to qualitative identification, the XRD results were also analyzed quantitatively to determine the percentage of each phase and the cell parameters of each phase formed in the sample. These results were obtained using Rietica version 4.0.5929.62851 software by applying the Rietveld method (Hunter, 1998). Among the many models for ZnO and Ag available in the COD database, the most suitable standard model was found for the ZnO phase (Sawadah et al., 1996) with a hexagonal wurtzite structure and the Ag phase (Suh et al., 1988). After several refinements, this model was the most consistent with the XRD peak pattern of the sample. The results of refining the ZnO/Ag nanocomposite sample with varying ZnO concentrations (0.1 M) are shown in **Figure 2**. In **Figure 2**, the black color represents the XRD data, the red color represents the model, the green color represents the difference in intensity between the two, and the vertical blue line indicates the diffraction peak.

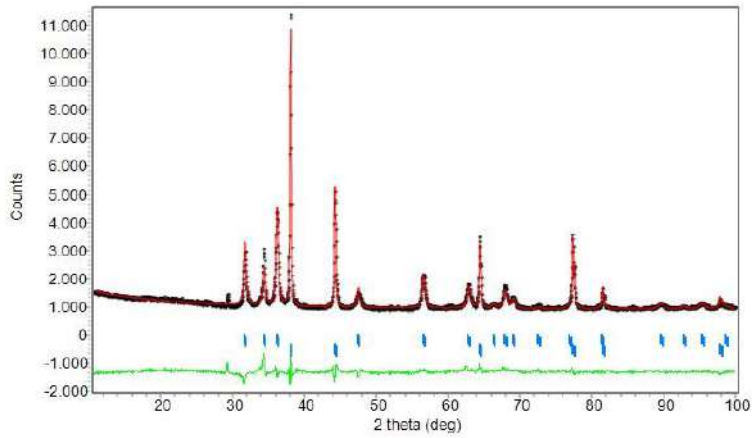

Figure 2. Results of XRD data refinement of ZnO/Ag nanocomposites with varying ZnO (0.1M).

The results of parameter refinement are shown in **Table 4** and the grid parameter cells in **Table 5.**

Table 4. Results of parameter refinement of XRD data for ZnO/Ag nanocomposites with variations of (0.1 M).

Sample	R_{wp}	R_p	R_{exp}	GOF
ZnO/Ag	4.62	3.41	2.89	0.256

Table 5. ZnO/Ag nanocomposite parameter sel with variation (0.1 M).

Phase	Grid Parameters (Å)		
	a	*b*	*c*
Ag	4.0856	4.0856	4.0856
ZnO	3.2499	3.2499	5.2053

The results of the XRD pattern adjustment are shown in **Table 4**, with values of Rp = 3.41, Rwp = 4.62, Rexp = 2.89, and GoF = 0.256, which are still below the tolerance limits (Rp, Rwp < 20% and GoF < 4%), so the refinement results can be considered valid. The lattice parameters obtained are shown in **Table 5**. ZnO has a = b = 3.2499 Å and c = 5.2053 Å, which corresponds to the hexagonal wurtzite structure, while Ag has a = b = c = 4.0856 Å, which corresponds to the cubic structure. The presence of these two phases indicates that the addition of Ag (68%) does not enter the ZnO (32%) lattice but is likely distributed on the surface or between particles (Al-Ariki et al., 2021).

3.3 SEM-EDX Characterization

Morphological characterization and particle size of ZnO/Ag samples using SEM-EDX with 10,000x magnification and a scale of 3 μm on ZnO/Ag samples with varying ZnO (0.1 M). The results of the analysis using SEM-EDX are shown in **Figure 3**.

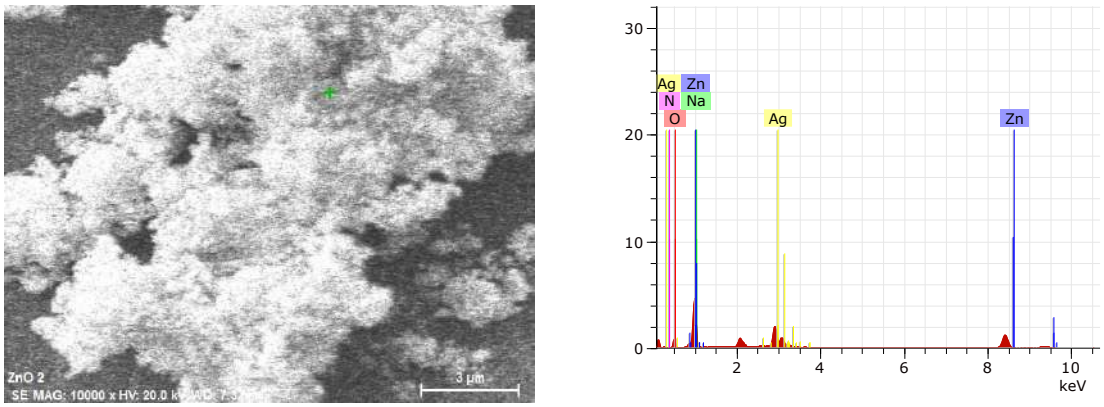

(a) (b)

Figure 3. SEM-EDX Characterization Results (a) Morphological Analysis and (b) Chemical Element Distribution of ZnO/Ag Nanocomposites with varying ZnO (0.1 M).

The morphological results of ZnO/Ag nanocomposites observed by SEM (**Figure 3a**) show that ZnO particles have a relatively uniform shape and a fairly homogeneous size distribution. In addition, Ag particles are evenly distributed among ZnO particles. This indicates that the synthesis process was carried out successfully (Caudra et al., 2022). Based on **Figure 3b**, the X-ray spectrum obtained shows characteristic peaks of the elements Zn and Ag. According to the theory of X-ray emission lines described by Bearden (1967), these peaks are formed due to the transition of electrons from the outer shell to the inner shell of the atom after the inner shell electrons are released due to high-energy electron collisions. For Zn, the main peak appears at an energy of 8.6 keV, which corresponds to the Ka line, while for Ag, the peak is detected at 3 keV, corresponding to the La line. This process occurs when the vacancy in the inner shell is filled by electrons from the outer shell, and the energy difference is emitted in the form of X-ray photons with characteristic energies for each element.

Table 6. Composition Results of ZnO/Ag Nanocomposite with ZnO Variations (0.1 M).

No.	Element	Unnormalized Weight Concentration (wt%)	Normalized Weight Concentration (wt%)	Atomic Concentration (at %)
1.	Oxygen (O)	7.40	39.98	42.47
2.	Zinc (Zn)	2.85	15.43	4.01
3.	Silver (Ag)	7.73	41.80	6.59
4.	Hydrogen (H)	0.51	2.78	46.93
5.	Sodium (Na)	0.00	0.00	0.00
6.	Nitrogen (N)	0.00	0.00	0.00
	Total	18.50	100.00	100.00

The EDX results (**Table 6**) confirm the presence of Zn and Ag elements. The detected Ag content is 41.80% by weight and Zn is 15.43% by weight. The high Ag concentration in this sample is due to the reduction of Ag+ ions to Ag^0 during the synthesis process, which is higher than the formation of ZnO, leading to the accumulation of larger Ag particles (Shrestha et al., 2024). This significant difference can be explained by the difference in atomic mass between the two elements, where Ag has an atomic mass of 107.87 g/mol, which is much larger than Zn with an atomic mass of 65.38 g/mol (Wagh et al., 2023).

3.4. Antibacterial Activity Test

The results of antibacterial activity testing of ZnO/Ag nanocomposites with varying concentrations of ZnO (0.04 M, 0.06 M, 0.08 M, and 0.1 M) against E. coli bacteria using the disk diffusion method are shown in **Figure 4**.

(a) (b) (c)

Figure 4. (a) Results of positive and negative control inhibition zones against E. coli bacteria; (b) and (c) Results of ZnO/Ag nanocomposite inhibition zones against E. coli bacteria. Note: 1 = ZnO/Ag 0.4 M; 2 = ZnO/Ag 0.6 M; 3 = ZnO/Ag 0.8 M; 4 = ZnO/Ag 1 M.

The results of the inhibition zone observations are shown in **Table 7.**

Table 7. Results of Observation of ZnO/Ag Nanocomposite Barrier Zone.

No.	Sample	Inhibition Zone Diameter (mm)
1.	K+	23.72
2.	K-	0
3.	0.04 M	12.46
4.	0.06 M	12.90
5.	0.08 M	15.08
6.	0.1 M	15.21

Based on **Table 7**, the largest inhibition zone diameter was found in the positive control (23.72 mm). In the ZnO/Ag samples, the largest diameter was found at a ZnO concentration of 0.1 M (15.21 mm). This indicates that ZnO-doped ZnO/Ag nanocomposites have an inhibitory effect on the growth of E. coli bacteria, as reported in the study by Raghupathi et al. (2011). In several studies conducted, such as the study by Akbarizadeh et al. (2022), it was shown that the inhibition zone of the ZnO/Ag nanocomposite was larger than that of pure ZnO. This suggests that the antibacterial activity of E. coli can be inhibited by the ZnO/Ag nanocomposite.

Overall, the XRF, XRD, SEM-EDX, and antibacterial tests can be explained through the relationship between material characteristics and performance. The XRF and SEM-EDX results show the dominance of ZnO with Ag as dispersed particles and a morphology that supports the formation of Reactive Oxygen Species (ROS) that damage microbial cell structures. Meanwhile, XRD shows a crystalline structure with nanoparticle-sized phases. All XRF, XRD, and SEM-EDX results directly contribute to the antibacterial test results, where the more optimal the composition, crystalline structure, and morphology, the greater the antibacterial effectiveness.

4. Conclusions

Based on the research results, ZnO/Ag nanocomposites were successfully synthesized by varying the concentration of the $Zn(NO_3)_2{\cdot}6H_2O$ precursor (0.04 M; 0.06 M; 0.08 M; and 0.1 M). XRF characterization results showed that Zn was the dominant element in the material, while Ag was doped in smaller amounts. XRD analysis confirmed that the crystal structure formed was hexagonal wurtzite (ZnO) and Face Centered Cubic (Ag). Meanwhile, SEM-EDX results showed homogeneous particle morphology with uniform element distribution, indicating good material structure quality.

Antibacterial activity testing using the disk diffusion method showed that the higher the concentration of $Zn(NO_3)_2{\cdot}6H_2O$ used, the larger the inhibition zone formed against Escherichia coli bacteria. This proves that ZnO/Ag nanocomposites have good antibacterial efficacy, and this efficacy increases with the increase in ZnO precursor concentration.

Thus, the ZnO/Ag nanocomposite synthesized in this study has the potential to be further developed as a functional material with superior antibacterial properties, making it applicable in the fields of health and the environment.

Acknowledgment

The authors would like to express their gratitude to the Department of Physics, Faculty of Mathematics and Natural Sciences, University of Lampung, for providing the facilities and support necessary to conduct this research. Thanks are extended to the laboratory staff for their assistance during the synthesis and characterization processes. The authors also sincerely appreciate the guidance, encouragement, and valuable input from colleagues and supervisors throughout the completion of this study.

5. Bibliography

Agarwal, H., Venkat Kumar, S., & Rajeshkumar, S. (2017). A review on green synthesis of zinc oxide nanoparticles – An eco-friendly approach. *Resource-Efficient Technologies, 3*(4), 406–413.

Akbarizadeh, M. R., Sarani, M., & Darijani, S. (2022). Study of antibacterial performance of biosynthesized pure and Ag-doped ZnO nanoparticles. *Rendiconti Lincei. Scienze Fisiche e Naturali, 33*(3), 613–621.

Al-Ariki, S., Yahya, N. A. A., Al-A'nsi, S. A., Jumali, M. H. H., Jannah, A. N., & Abd-Shukor, R. (2021). Synthesis and comparative study on the structural and optical properties of ZnO doped with Ni and Ag nanopowders fabricated by sol–gel technique. *Scientific Reports, 11*(1), 1–11.

Alharthi, F. A., Alghamdi, A. A., Al-Zaqri, N., Alanazi, H. S., Alsyahi, A. A., Marghany, A. El, & Ahmad, N. (2020). Facile one-pot green synthesis of Ag–ZnO nanocomposites using potato peel and their Ag concentration dependent photocatalytic properties. *Scientific Reports, 10*(1), 1–14.

Amrute, V., Monika, N., Supin, K. K., Vasundhara, M., & Chanda, A. (2024). Observation of excellent photocatalytic and antibacterial activity of Ag doped ZnO nanoparticles. *RSC Advances, 14*(45), 32786–32801.

Asamoah, R. B., Annan, E., Mensah, B., Nbelayim, P., Apalangya, V., Onwona-Agyeman, B., & Yaya, A. (2020). A comparative study of antibacterial activity of CuO/Ag and ZnO/Ag nanocomposites. *Advances in Materials Science and Engineering, 2020*, 1–18.

Azam, A., Ahmed, A. S., Oves, M., Khan, M. S., Habib, S. S., & Memic, A. (2012). Antimicrobial activity of metal oxide nanoparticles against gram-positive and gram-negative bacteria: A comparative study. *International Journal of Nanomedicine, 7*, 6003–6009.

Bearden, J. A. (1967). X-ray wavelengths. *Reviews of Modern Physics, 39*(1), 78–124.

Chand Gurjar, K., Agrawal, A., Kumar, S., Sharma, R., Pandey, K., Pandey, H., & Awasthi, A. (2023). Antimicrobial efficacy of Ag-doped ZnO nanocomposite against *Bacillus subtilis*. *Materials Today: Proceedings, 95*, 61–66.

Cuadra, J. G., Scalschi, L., Vicedo, B., Guc, M., Izquierdo-Roca, V., Porcar, S., Fraga, D., & Carda, J. B. (2022). ZnO/Ag nanocomposites with enhanced antimicrobial activity. *Applied Sciences, 12*(10), 1–13.

Cullity, B. D. (1978). *Elements of X-ray diffraction* (2nd ed.). Addison-Wesley.

Fatoni, A., Hilma, H., Rasyad, A. A., Novriyanti, S., & Hidayati, N. (2020). Biosintesis ZnO nanopartikel dari ekstrak air daun jambu biji (*Psidium guajava* L.) dan ion Zn2+ serta interaksinya dengan kitosan sebagai antibakteri *Escherichia coli*. *Jurnal Sains Farmasi & Klinis, 7*(2), 151–158.

Hunter, B. A. (1998). Rietica – A visual Rietveld program. *Commission on Powder Diffraction Newsletter, 20*, International Union of Crystallography.

Kolopita, P. S., Hariyadi, H., Sambou, C. N., & Tulandi, S. S. (2022). Uji aktivitas antibakteri kulit batang alpukat (*Persea americana* Mill.) terhadap bakteri *Staphylococcus aureus* dan *Escherichia coli*. *Majalah INFO Sains, 3*(1), 19–26.

Raghupathi, K. R., Koodali, R. T., & Manna, A. C. (2011). Size-dependent bacterial growth inhibition and mechanism of antibacterial activity of zinc oxide nanoparticles. *Langmuir, 27*(7), 4020–4028.

Rompis, J., Aritonang, H., & Pontoh, J. (2020). Sintesis nanokomposit ZnO–MgO dan analisis efektivitas sebagai antibakteri. *Chemistry Progress, 13*(1), 56–62.

Sawadah, H., Wang, R., & Sleght, A. W. (1996). An electron density residual study of zinc oxide. *Journal of Solid State Chemistry, 122*, 148–150.

Shrestha, D. K., Magar, A. B., Bhusal, M., Baraili, R., Pathak, I., Joshi, P. R., Parajuli, N., & Sharma, K. R. (2024). Synthesis of silver and zinc oxide nanoparticles using *Polystichum lentum* extract for potential antibacterial, antioxidant, and anticancer activities. *Journal of Chemistry, 2024*, 1–15.

Singh, J., Dutta, T., Kim, K. H., Rawat, M., Samddar, P., & Kumar, P. (2018). Green synthesis of metals and their oxide nanoparticles: Applications for environmental remediation. *Journal of Nanobiotechnology, 16*(1), 1–24.

Suh, I. K., Ohta, H., & Waseda, Y. (1988). High-temperature thermal expansion of six metallic elements measured by dilatation method and X-ray diffraction. *Journal of Materials Science, 23*, 757–760.

Tran, Q. H., Nguyen, V. Q., & Le, A. T. (2013). Silver nanoparticles: Synthesis, properties, toxicology, applications and perspectives. *Advances in Natural Sciences: Nanoscience and Nanotechnology, 4*(3), 033001.

Wagh, S. S., Kadam, V. S., Jagtap, C. V., Salunkhe, D. B., Patil, R. S., Pathan, H. M., & Patole, S. P. (2023). Comparative studies on synthesis, characterization and photocatalytic activity of Ag doped ZnO nanoparticles. *ACS Omega, 8*(8), 7779–7790.

World Health Organization. (2015). *Global action plan on antimicrobial resistance*. World Health Organization.

Zare, M., Namratha, K., Alghamdi, S., Mohammad, Y. H. E., Hezam, A., Zare, M., Drmosh, Q. A., Byrappa, K., Chandrashekar, B. N., Ramakrishna, S., & Zhang, X. (2019). Novel green biomimetic approach for synthesis of ZnO–Ag nanocomposite: Antimicrobial activity against food-borne pathogen, biocompatibility and solar photocatalysis. *Scientific Reports, 9*(1), 1–15.

JOURNAL OF ENERGY, MATERIALS, AND INSTRUMENTATION TECHNOLOGY

Journal Webpage https://jemit.fmipa.unila.ac.id/

Biopolymer Gel from Pineapple Peel (*Ananas comosus*) Waste-Based Gel with Sodium Chloride (NaCl) for Optimizing Electrocardiogram (ECG) Signal Recording

Meita Mahardianti[1*], Salsabila Septha Kharisma[1], Rosita Wati[1], and Yusuf Affandi[2]

1. Department of Biomedical Engineering, Institut Teknologi Sumatera, Lampung, Indonesia, 35365
2. Department of Instrumentation and Automation Engineering, Institut Teknologi Sumatera, Lampung, Indonesia, 35365

Article Information

Article history:
Received September 25, 2025
Received in revised form December 4, 2025
Accepted January 30, 2026

Keywords: *ECG Gel, Pineapple Peel Waste, NaCl, Conduvtivity, ECG Signal*

Abstract

*Pineapple peel (*Ananas comosus*) as organic waste has potential as a raw material for biomedical gel in electrocardiogram (ECG) recording. ECG gel functions as a conductive medium facilitating electrical transmission between skin and electrodes to improve cardiac signal accuracy. This study developed gel from pineapple peel waste with sodium chloride (NaCl) addition for ECG recording optimization. The process included pineapple peel extraction, gel formulation using carbomer 940, and extract concentration variations of 10-100%. Evaluation was conducted on physical properties including electrical conductivity, viscosity, pH, density, crust thickness, and ECG recording performance. Results showed gel with 20-50% pineapple peel extract had high conductivity, skin-compatible pH (4.5-7), and reduced crust thickness. ECG recording produced well-defined P, QRS, and T waves with minimal noise. These findings demonstrate that pineapple peel waste-based gel is a promising eco-friendly alternative for cardiac diagnostics and sustainable organic waste utilization.*

Informasi Artikel

Proses artikel:
Diterima 25 September 2025
Diterima dan direvisi dari 4 December 2025
Accepted 30 Januari 2026

Kata kunci: *Gel EKG, Limbah Kulit Nanas, NaCl, Konduktivitas, Sinyal EKG*

Abstrak

Kulit nanas (Ananas comosus) sebagai limbah organik berpotensi sebagai bahan baku gel biomedis untuk perekaman elektrokardiogram (EKG). Gel EKG berfungsi sebagai media konduktif yang memfasilitasi transmisi listrik antara kulit dan elektroda untuk meningkatkan akurasi sinyal jantung. Penelitian ini mengembangkan gel dari limbah kulit nanas dengan penambahan natrium klorida (NaCl) untuk optimasi perekaman EKG. Proses meliputi ekstraksi kulit nanas, formulasi gel menggunakan carbomer 940, dan variasi konsentrasi ekstrak 10-100%. Evaluasi dilakukan terhadap sifat fisika seperti konduktivitas listrik, viskositas, pH, densitas, ketebalan kerak, dan kinerja perekaman EKG. Hasil menunjukkan gel dengan 20-50% ekstrak kulit nanas memiliki konduktivitas tinggi, pH kompatibel dengan kulit (4,5-7), dan ketebalan kerak berkurang. Perekaman EKG menghasilkan gelombang P, QRS, dan T terdefinisi baik dengan noise minimal. Temuan ini menunjukkan gel berbasis limbah kulit nanas merupakan alternatif ramah lingkungan yang menjanjikan untuk diagnostik jantung dan pemanfaatan limbah organik berkelanjutan.

1. Introduction

Indonesia ranks among the world's largest pineapple producers, with total production reaching 3.2 million tons in 2022, representing a 10.99% increase from the previous year's 2.8 million tons. This production growth reflects high demand for pineapples in both domestic consumption and export markets, demonstrating development in Indonesia's agricultural and agroindustrial sectors. Among all pineapple-producing regions in Indonesia, Lampung Province ranks first as the main producer with total production reaching 695.86 thousand tons annually, making it

* Corresponding author.
E-mail address: (a)gurum@fmipa.unila.ac.id; (b)warsito@fmipa.unila.ac.id

the national center of the pineapple plantation industry (Pusat Data dan Sistem Informasi Pertanian, 2023). The pineapple processing industry generates significant waste volume, considering annual pineapple production statistics reach approximately 40 million tons with disposal of inedible parts contributing about 60% of total weight (Gavahian, 2023). This rapid growth in Indonesia's pineapple processing industry presents immediate challenges, as high production volumes directly impact waste generation, particularly pineapple peels often neglected in conventional processing, potentially producing around 4,024,800 kg of pineapple peel waste annually from processing industries (Anggraini et al., 2022).

Various studies have demonstrated that pineapple peel waste (*Ananas comosus*) has significant potential for sustainable utilization across sectors as valuable alternative raw materials. Previous research shows pineapple peels can be utilized for probiotic beverages containing bioactive compounds like bromelain, flavonoids, and tannins, with antibacterial and prebiotic effects beneficial for health (Nurfaizin et al., 2023). Additionally, antioxidant activity studies indicate pineapple peel extracts, particularly with methanol solvents, have potential as strong natural antioxidants (Saka Nugraha et al., 2024). These studies show that pineapple peel waste utilization has evolved from conventional processing to high-value innovations through modern fermentation and extraction, contributing to circular economy, waste reduction, and applications in food, health, and energy sectors.

Recognizing its functional potential, pineapple peel waste is now developed further as gel-based material for technological and medical applications, particularly in electrogel production for medical applications including ECG gel. ECG gel functions as a conductive medium for electrical signals between skin and electrodes, optimizing signal recording quality (Ibrahim et al., 2016). Pineapple peel waste contains various bioactive compounds such as flavonoids, tannins, and bromelain enzyme with proteolytic properties (Salasa, 2019). These contents make pineapple peel waste potential material for ECG gel formulation due to its environmentally friendly and value-added nature. NaCl addition serves as electrolyte enhancing electrical conductivity, enabling better electrical signal transmission between skin and ECG electrodes (Adilah Wirdhani Lubis, 2020).

ECG gel usage is crucial in cardiac electrical signal recording as it enhances conductivity between skin and electrodes, ensuring more accurate and stable signals (Attia et al., 2019). Optimal electrode function requires adhesive gel as conductive medium, creating electrochemical processes between skin surface and electrodes for efficient electrical signal capture (Basuki, 2014). ECG gel contains conductive materials like salts or compounds with high electrical conductivity such as sodium chloride (NaCl), along with thickening agents like carbomer 940 maintaining gel viscosity and stability (Kesehatan et al., 2018). However, conventional commercial ECG gels made from synthetic polymer mixtures, humectants, electrolytes, and chemical additives can cause skin irritation including rashes, bacterial growth, and allergic contact dermatitis from compounds like paraben, formaldehyde, methylisothiazolinone (MIT), benzalkonium chloride, ethanol, isopropanol, sodium lauryl sulfate (SLS), synthetic fragrance, tartrazine, para-phenylenediamine (PPD), propylene glycol, and diethyl phthalate (DEP) (M. Avenel-audran et al., 2003; Soroudi et al., 2019; Wu et al., 2021).

Pineapple peel waste utilization as ECG gel base material has strong potential in medical fields due to chemical properties rich in bioactive compounds and natural electrolytes [4]. Research has successfully developed hydrogels based on agarose and hyaluronic acid reinforced with phenolic compounds from pineapple peels, proving technical validity and formulation stability (Yin et al., 2024). Furthermore, oxidized cellulose from pineapple peels can be used in electric field-responsive hydrogels showing adaptability and structural stability under electrical stimulus, important properties for ECG signal transmission and recording. Flavonoid and phenolic contents in pineapple peels have been utilized in green synthesis of AgNPs, providing antioxidant and antibacterial activities valuable for developing electrogel materials that are not only electrically efficient but also medically safe and beneficial (Das et al., 2019). Therefore, developing ECG gel based on pineapple peel waste with various extract concentrations represents an innovative medical solution, supporting gel stability while NaCl addition enhances electrical conductivity for optimal signal transmission, promoting sustainable and innovative natural material usage applicable in healthcare industries.

2. Research Methods

2.1 Materials and Equipment

This study utilized specific equipment including a blender, oven, beakers, measuring cups, Biobase digital scale, glass stirrer, spatula, Sakurama Electrical Conductivity meter, Brookfield viscometer, metal plates, Philips hair dryer, SH-2 magnetic stirrer, Batavialab pH meter, Avntru digital thickness gauges, and EDAN ECG equipment set. The materials comprised 420 ml of pineapple peel waste extract, Chemical Products NaCl electrolyte salt, Rendys Chemical carbomer 940, distilled water, and 10% Edukanca NaOH. Onemed conventional ECG gel served as the control sample for comparison with the developed pineapple peel waste-based gel (**Figure 1**).

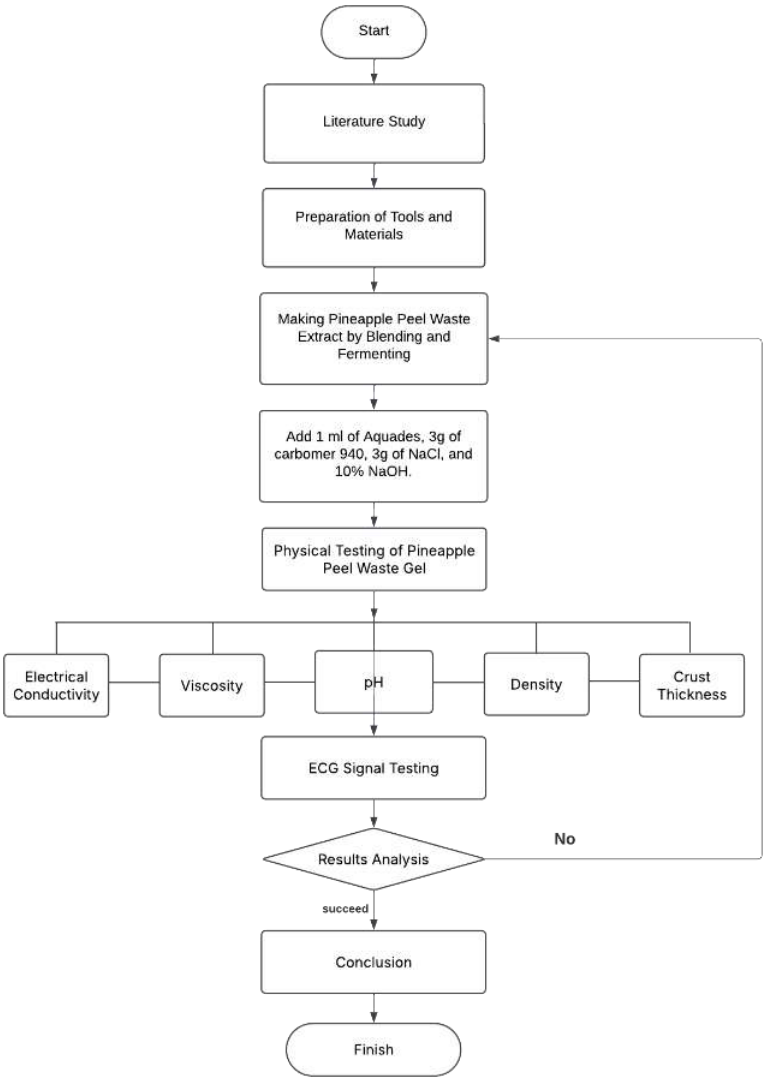

Figure 1. Research process

2.2 Sample Preparation and Gel Formulation

The research process began with pineapple peel waste collection from vendors, followed by thorough cleaning to remove dust, dirt, and pesticide residues. The cleaned peels underwent saltwater immersion for 30 minutes to reduce surface bacterial count, then oven-dried at 70°C for 190 minutes to prevent microbial growth. The dried peels were ground using a blender and fermented for 72 hours to produce the extract. Gel formulation involved mixing varying concentrations of pineapple peel extract (10%, 20%, 30%, 50%, and 100%) in 200 ml total volume with aquadest water, 3 grams of NaCl electrolyte salt, and 3 grams of carbomer 940. The pH was adjusted using 10% NaOH solution to match physiological skin pH levels.

2.3 Physical Parameter Testing

The formulated gels underwent comprehensive physical characterization including electrical conductivity measurement using an EC meter with probe insertion directly into gel samples, with acceptable values ranging from 100 µS/cm to 1000 µS/cm. Viscosity testing employed a Brookfield viscometer at rotational speeds of 2-5 rpm, targeting values below 10,000 cps for optimal performance. pH measurement utilized a calibrated pH meter with direct probe immersion, maintaining values within the 4.5-7 range suitable for skin contact. Density determination involved manual calculation by dividing gel mass (measured using digital scale) by volume (measured using 50 mL graduated cylinder), targeting the standard value of 1.08 g/cm^3. Crust thickness analysis was conducted by placing 1 gram of gel on metal plates, drying with a hair dryer, and measuring thickness using digital thickness gauges, with the standard thickness being 0.0035 cm.

2.4 ECG Signal Analysis

ECG signal evaluation was performed using a complete ECG system consisting of ECG machine, cables, electrodes, computer, and the test gels. Signal quality assessment focused on P wave characteristics (positive in leads

I and II, optimal display in leads II and V1, bifasic in lead V3), with normal duration less than 3 small squares and amplitude less than 2.5 small squares. PR interval measurements ranged from 0.12-0.20 seconds, measured from P wave onset to QRS complex beginning, ensuring clear P, QRS, and T wave definition with minimal noise interference (**Figure 2**).

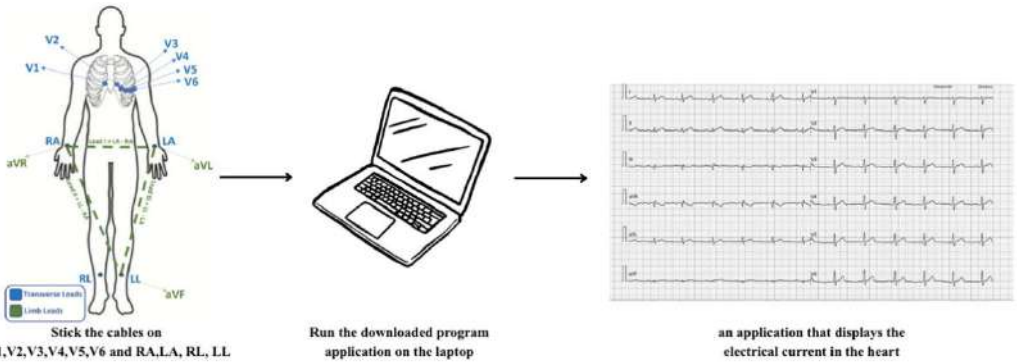

Figure 2 ECG signal acquisition diagram

2.5 Data Analysis and Statistical Methods

Data analysis employed descriptive methods to evaluate and compare physical characteristics of pineapple peel waste-based ECG gel against conventional gel. Statistical analysis included mean calculation for data representation, normalization methods applied to viscosity, density, and crust thickness parameters using the formula 1, standard deviation calculation to assess data variability, and coefficient of variation (CV) determination with values below 5% considered ideal for good precision. All measurements were conducted in triplicate to ensure reproducibility, with results compared against conventional ECG gel standards to assess the effectiveness and feasibility of pineapple peel waste-based gel as an environmentally friendly alternative for cardiac diagnostic applications.

$$Norm = 1 - \frac{X_{variation} - X_{control}}{Biggest\ gap} \quad (1)$$

3. Results and Discussions

3.1 Electrical Conductivity

Electrical conductivity is an important parameter in ECG gel development as it determines the gel's ability to conduct electrical signals from the skin to the electrodes. In this study, the gel base material was derived from fermented pineapple peel waste to obtain active compounds that play a role in enhancing electrical conductivity values (Irani et al., 2018), which was supplemented with 3 grams of NaCl electrolyte salt (Fitrya et al., 2022). Electrical conductivity values were measured using an EC Meter at various concentrations of pineapple peel waste, as shown in **Figure 3**.

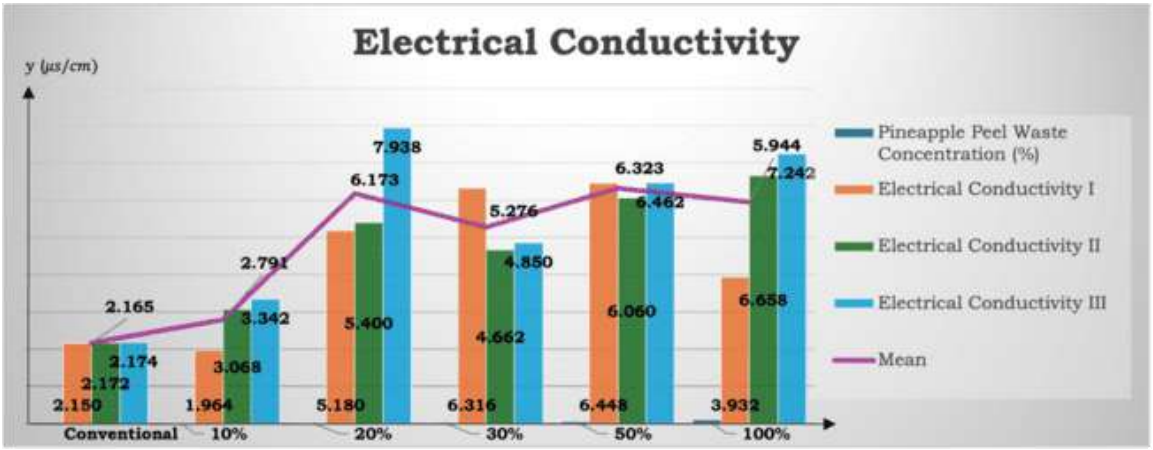

Figure 3. Electrical Conductivity Test Results Diagram

Pineapple peel can be utilized as a conductive medium in ECG gel applications because it contains ionic compounds that enable electrical current conduction. The electrical conductivity in pineapple peel originates from

organic acid content such as citric acid which produces H^+ ions, strong electrolyte minerals such as sodium, potassium, and magnesium that dissolve to form charged ions, as well as carbohydrates that can be fermented into additional acid compounds (Sitanggang et al., 2021). Based on the data **Figure 3**, it is known that the electrical conductivity value of conventional ECG gel has an average of 2.165 µS/cm, which serves as a reference in assessing the effectiveness of the developed gel. The formulation with 10% concentration showed increased conductivity compared to the control, averaging 2.791 µS/cm. Although the first measurement was relatively low compared to conventional gel, the second and third measurements showed increases. This indicates that although conductive compounds from fermentation begin to emerge, their quantity is not yet sufficient to significantly outperform conventional gel performance in the initial preparation (Putri & Abdul Halim Daulay, 2021). At 20% concentration, conductivity increased to an average of 6.172 µS/cm, making it a formulation with considerably high conductivity compared to conventional ECG gel.

This result demonstrates synergy between natural electrolyte compounds from fermentation and ions from added NaCl (Navaratnam et al., 2020). This value is nearly three times higher than conventional gel, showing significant superiority in electrical signal transmission efficiency. Formulations with 30% concentration ranging at 5.276 µS/cm and 50% ranging at 6.323 µS/cm also showed high conductivity, both remaining much higher than conventional gel. Meanwhile, the 100% concentration ranging at 5.944 µS/cm still demonstrated electrical conductivity superiority over conventional gel (Zakzak et al., 2024). Variations in each concentration and repetition can occur due to differences in manual stirring, contact duration, or waste distribution in solution, which are commonly found in similar research and highlight the importance of standardizing experimental procedures to obtain consistent results (Djamalu et al., 2019; Rahmasari Pohan, 2021).

3.2 Viscosity Test Results

Viscosity is an important physical parameter in ECG gel formulation as it determines how well the gel adheres to skin and electrodes without easily flowing or drying out. Viscosity values that are too high can complicate application, while viscosity that is too low will cause the gel to spread easily and become unstable during use (Komachi et al., 2017).

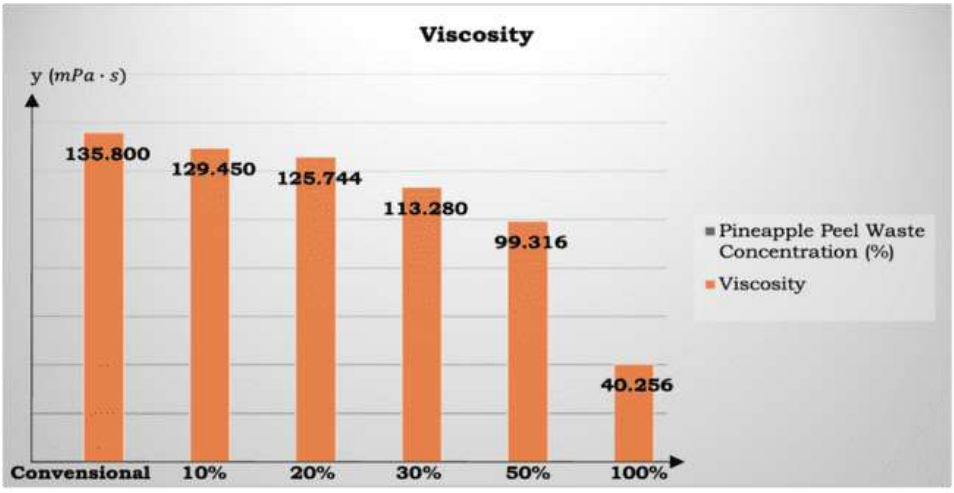

Figure 4. Viscosity Test Results Diagram

Based on **figure 4**, the viscosity of conventional gel available in the market is at 135.800 mPa.s, which serves as a reference comparison in this study. Meanwhile, all gel formulas developed using pineapple peel waste as the base material with the addition of 3 grams of NaCl and 3 grams of carbomer 940, as well as pH adjustment using 10% NaOH, showed varying results. At 10% pineapple peel waste concentration, the resulting viscosity was 129.450 mPa.s, approaching the control gel viscosity. At 20% concentration, the viscosity decreased to 125.744 mPa.s, but this value is still within the ideal range for ECG gel applications (Septiani & Fitriyani, 2025). Conditions began to change significantly at 30% and 50% concentrations, where viscosities decreased to 113.280 mPa.s and 99.316 mPa.s, respectively. A drastic decrease occurred at 100% concentration, with viscosity only reaching 40.258 mPa.s, which is considered too low for medical gel standards as it can cause the gel to flow easily and become unstable when used on electrodes (Fan et al., 2021).

The phenolic and flavonoid content in pineapple peel extract can form both hydrogen and hydrophobic interactions with polar groups on polymers, which can disrupt internal cross-linking between polymer chains, making the gel structure looser and reducing viscosity (Ode et al., 2024). The presence of bromelain, a natural proteolytic enzyme in pineapple peels, also contributes by cleaving protein bonds or other polymer components, which weakens the gel structure and reduces overall viscosity. Although its direct effect on viscosity has not been extensively studied explicitly, logically the reduction in network structure supports the decrease in viscosity (Lourenço et al., 2021).

3.3 pH Gel

The acidity level (pH) is an important parameter in ECG gel formulation as it directly relates to the comfort and safety of gel use on human skin. Generally, skin pH ranges from 4.5 to 7 (Novi Titin Wijayanti, 2018), therefore gel formulation must be within this range to avoid irritation or disruption to the skin's natural balance.

Table 1 shows the measurement results of acidity levels (pH) from the control gel and those formulated with varying concentrations of pineapple peel waste, namely 10%, 20%, 30%, 50%, and 100%. Measurements were

conducted three times for each concentration, and pH values were expressed on a pH scale (unitless). In the control sample, pH values were recorded as 7.23, 7.27, and 7.30, indicating neutral characteristics (Infokom PPNI Jaktim, 2021). At 10% pineapple peel waste, pH decreased to 6.49, 6.60, and 6.72. A further decrease was observed at 20% concentration with pH values of 6.15, 6.25, and 6.45. At 30% concentration, pH ranged from 6.49, 6.51, and 6.67. Meanwhile, at 50% concentration, pH was recorded stable at 6.22, 6.23, and 6.24. For the highest concentration of 100%, pH values were 6.28, 6.35, and 6.40. In the pineapple peel waste ECG gel formulation, pH remained within the safe range and approached the physiological pH of skin, which ranges from 4.5 to 7 (Infokom PPNI Jaktim, 2021; Lee et al., 2020).

Table 1. pH's gel

Pineapple Peel Waste Concentration (%)	pH			Mean	STD	KV(%)
	I	II	III			
Conventional	7.23	7.27	7.30	7.27	0.035119	0.48
10	6.49	6.60	6.72	6.60	0.115036	1.74
20	6.15	6.25	6.45	6.28	0.152753	2.43
30	6.49	6.51	6.67	6.56	0.098658	1.50
50	6.22	6.23	6.24	6.23	0.010000	0.16
100	6.28	6.35	6.40	6.34	0.060277	0.95

The pH testing represents a crucial stage to ensure product safety and suitability when applied to human skin. This examination is essential because pH within the physiological skin range (approximately 4.5 to 7) can help reduce irritation potential and maintain gel formulation stability during storage and application (Septiani & Fitriyani, 2025; Setyo Wiyono et al., 2019). At 10% pineapple peel waste concentration, pH values ranged from 6.49–6.72, indicating that at low concentrations, pineapple peel waste fermentation does not cause significant pH reduction and can be controlled with 10% NaOH addition (Nasoha et al., 2023)**.** At 20% and 30% concentrations, pH remained within the 6.15–6.67 range, which also complies with human skin tolerance limits (Novi Titin Wijayanti, 2018). These values demonstrate that fermentation compounds begin to exhibit acidic effects, yet can still be effectively neutralized through adjustment with base solution (10% NaOH). At 50% concentration, pH was slightly lower (around 6.22), but remained within safe limits (Nasoha et al., 2023). At 100% concentration, pH values ranged from 6.28 to 6.40, which remains relatively safe despite approaching the lower limit of normal skin pH (Anisah Putri Yuana Sari et al., 2024). This indicates that increased fermentation material concentration causes increased acidity, but not to the extent of creating strongly acidic gel. The addition of 10% NaOH proved effective in maintaining formulation pH stability (Nasoha et al., 2023).

The pH value differences across various pineapple peel waste concentrations, despite controlled treatment and environmental conditions, are primarily caused by substrate concentration effects on microorganism activity during fermentation processes. Different substrate concentrations result in varied organic acid production by microbes such as Saccharomyces cerevisiae, causing different pH changes, where 10% concentration tends to produce higher pH due to less acid accumulation, while 20% to 100% concentrations generate lower pH due to increased organic acid production (Nurwahyu Chamidy et al., 2023). Additionally, differences in nutrient availability, microorganism density, and metabolic rates at each concentration also contribute to pH variation despite identical procedures and environment (Febriningrum, 2013).

3.4 Density

Density or specific gravity is a physical parameter that describes the amount of mass per unit volume and serves as an important indicator in assessing the physical characteristics of a gel formulation. Density values significantly influence comfort, stability, and ease of gel application on skin surfaces, including medical applications such as ECG signal recording (Grigatti & Gefen, 2022).

Table 2. Density

Pineapple Peel Waste Concentration (%)	Density			Mean	STD	KV (%)
	I	II	III			
Conventional	1.0103	1.0705	1.0648	1.05	0.033233	3.17
10	1.2104	1.2103	1.2039	1.21	0.003724	0.31
20	1.0028	1.0029	1.0031	1.00	0.000153	0.02
30	1.2441	1.2438	1.2438	1.24	0.000173	0.01
50	1.0758	1.0757	1.0757	1.08	0.000058	0.01
100	1.1247	1.1247	1.1248	1.12	0.000058	0.01

From the data in **Table 2**, the highest density was recorded at 30% concentration, with respective values of 1.2441 g/mL, 1.2438 g/mL, and 1.2438 g/mL. Meanwhile, the lowest density was found at 20% concentration, with sequential values of 1.0028 g/mL, 1.0029 g/mL, and 1.0031 g/mL, indicating that this formulation has a balance between liquid and dissolved substances, making the gel sufficiently light yet stable and easy to apply (Kusumawati

et al., 2023). The difference in density at each concentration of pineapple peel waste is influenced by the amount of dissolved substances contained in the solution, such as organic compounds, ions, and fermentation products (Garza & Ibarz, 2010). Higher concentrations tend to contain more dissolved solids, which increases the solution's density (Selvanathan & Masngut, 2021).

This increase in density indicates an increase in the number of dissolved substances or solid compounds in the gel, originating from fermented pineapple peel waste and additional contributions from NaCl and carbomer. This high density indicates that the formed gel tends to be denser and more viscous, which could provide better adhesion but also risks being less comfortable if too heavy (Fadillah et al., 2025). Generally, variations in pineapple peel waste concentration in gel formulation affect density values, recorded in grams per milliliter (g/mL). The higher the density value obtained, the greater the possibility of increased solid substances or dissolved compounds in the mixture, although further analysis is needed to draw this conclusion scientifically (Nigen et al., 2019).

Crust Thickness

Crust thickness is a parameter used to assess the physical stability of gel against evaporation when applied to the electrode surface. The thicker the crust formed, the greater the likelihood of gel experiencing dehydration or hardening, which can interfere with ECG signal transmission (Lee et al., 2020). Therefore, measuring crust thickness is important to ensure the gel remains in optimal condition during clinical use.

Measurements were conducted using a thickness gauge on the stainless steel electrode plate surface after the gel was dried using a hair dryer. The fermented pineapple peel gel formulation demonstrated good performance with crust thickness of approximately 0.01 mm, compared to conventional gel which had a thickness of 0.02 mm. This value indicates that the control gel has a tendency to form thicker crust layers, which may indicate water evaporation or solvent evaporation (Mao et al., 2016). The ideal condition from these results was observed at concentrations of 20% to 100%, where all variations showed low and uniform crust thickness (0.01 mm). Meanwhile, at 10% concentration, it still showed a thickness of 0.02 mm. This occurs due to the combination of water-rich pineapple extract and organic components, carbomer as a thickening agent, NaCl as a conductor, and pH adjustment with 10% NaOH that together produce gel, leaving dry residue (Novi Titin Wijayanti, 2018). This indicates that the formulated gel is capable of maintaining moisture well and minimizing crust formation that can interfere with conductivity and comfort during use (Carvalho et al., 2025).

In **Table 3**, all variations of pineapple peel waste concentration produced very low mean values, differences, standard deviation (Std), and coefficient of variation (CV) (<5%), indicating that the measurement precision level is high. These results demonstrate that natural formulations have good resistance to drying, making them ideal for ECG examinations (Sadia Afzal et al., 2022). The sufficiently high water content in the fermented gel and the stable gel bond structure provide distinct advantages in maintaining moisture and minimizing signal transmission interference due to gel drying during the examination process (Sriprablom et al., 2023).

Table 3. Crust thickness

Pineapple Peel Waste Concentration (%)	Crust thickness			Mean	STD	KV (%)
	I	II	III			
Conventional	0.02	0.02	0.02	0.02	0	0
10	0.02	0.02	0.02	0.02	0	0
20	0.01	0.01	0.01	0.01	0	0
30	0.01	0.01	0.01	0.01	0	0
50	0.01	0.01	0.01	0.01	0	0
100	0.01	0.01	0.01	0.01	0	0

In testing the effectiveness of ECG signal recording using conventional gel as a control, examination results showed a heart rate of 82 bpm per minute, which falls within the normal range (Heru Sulastomo et al., 2019). Based on the ECG examination that has been conducted, the cardiac condition shows good and normal results overall (Soliman et al., 2017). ECG or electrocardiogram is an examination that records the electrical activity of the heart to observe how the heart functions, and the examination results indicate that the subject's heart is functioning properly (Gonçalves et al., 2020).

Table 4. ECG signal recording

Parameter	Normal Value	Conventional Gel	Pineapple Peel Gel					Clinical Interpretation
			10%	20%	30%	50%	100%	
Heart rate (HR)	60-100bpm	82bpm	82bpm	73bpm	81bpm	75bpm	75bpm	Normal
P duration	60-120ms	106ms	107ms	105ms	107ms	103ms	101ms	Normal
PR interval	120-200ms	182ms	185ms	186ms	177ms	181ms	181ms	Normal
QRS duration	75-105ms	83ms	83ms	86ms	86ms	85ms	88ms	Normal
QT/QTc	350-450ms	335/393ms	337/395ms	344/380ms	338/394ms	343/385ms	342/384ms	Normal

Based on **table 4** conventional gel, regarding the P wave that indicates atrial activity, the results were very normal with a duration of 106 ms, which falls within the healthy range (60-120 ms) (Chen et al., 2022), with good waveform morphology indicating that both atria are functioning normally (Yasuma & Hayano, 2004)**.** The QRS complex, which is the most important part of the ECG and represents ventricular contraction when the ventricles pump blood throughout the body (Utari, 2016), showed excellent results with a duration of 83 ms within the normal range (60-120 ms), indicating that electrical impulses flow efficiently through the ventricles (Hnatkova et al., 2021).

The T wave, which represents ventricular repolarization after contraction, also displayed normal results, with QT/QTc intervals of 335/393 ms within healthy limits and normal T wave morphology in all examination areas (Rezuş et al., 2015). The quality of the ECG recording was excellent, with high wave clarity and minimal interference (Yadav et al., 2016). There was no noise from body movement or electrical interference that could disrupt result interpretation, with stable baseline recording and all waves clearly identifiable, making the examination results reliable and accurate (Sofie & Rizal, 2016a; Winursito & Korespondensi, 2022). The overall test results demonstrate that conventional gel is capable of providing optimal ECG signal quality for cardiac electrical activity analysis with parameters within normal ranges.

In the effectiveness testing of ECG signal recording using a gel based on pineapple peel waste with a 10% concentration, examination results showed a heart rate of 82 beats per minute, which falls within the normal range (Heru Sulastomo et al., 2019). Based on the ECG results obtained on **Table 4**, the overall cardiac condition of the subject demonstrated good and normal findings, as evidenced by the three main waves that reflect cardiac function (Gonçalves et al., 2020; Soliman et al., 2017). The P wave showed excellent normal results with a duration of 107 ms, falling within the normal range of 60-120 ms (Chen et al., 2022). The waveform morphology also appeared optimal, indicating that the heart beats with proper rhythm originating from the sinoatrial node, demonstrating that the subject's atria function effectively in pumping blood to the heart ventricles (Yasuma & Hayano, 2004). The QRS complex, representing ventricular contraction, also displayed normal results with a duration of 83 ms, remaining within the normal limits of 60-120 ms, indicating that electrical conduction in the ventricles operates efficiently (Hnatkova et al., 2021). The T wave, reflecting the cardiac recovery phase after contraction, showed normal results with QT/QTc values of 337/395 ms within normal limits, indicating proper cardiac recovery processes occurring within appropriate timeframes, along with normal T wave morphology (Rautaharju et al., 2009; Rezuş et al., 2015).

The quality of the subject's ECG recording was excellent, characterized by high wave clarity and minimal interference (Yadav et al., 2016). No disturbances or noise interfered with the reading, and the baseline recording appeared stable and clean across all leads. This enabled physicians to provide accurate and precise interpretations of each cardiac wave component (Sofie & Rizal, 2016b; Winursito & Korespondensi, 2022). Such high recording quality is crucial for ensuring accurate diagnosis. In conclusion, the subject's ECG results demonstrated a healthy heart with normal rhythm and proper electrical function, validating the effectiveness of the pineapple peel-based gel as a viable alternative for ECG electrode applications.

In testing the effectiveness of ECG signal recording using pineapple peel waste-based gel at 20% concentration, examination results showed a heart rate of 73 bpm per minute, which is a normal heart rate within the range of 60-100 bpm (Heru Sulastomo et al., 2019). Based on the ECG results conducted, overall the subject's heart condition showed good and normal results, which can be seen from the three main waves that reflect the heart's functioning (Gonçalves et al., 2020; Soliman et al., 2017). Based on **Table 4**, the examination results showed that the subject's P wave was very normal. The subject's P wave duration was 105 ms, which is within the normal range of 60-120 ms (Chen et al., 2022). The QRS duration in the subject was 86 ms, still within the normal limit of 60-120 ms (Hnatkova et al., 2021). The heart's electrical flow direction was also within the normal range at -11, where normal is -30° to 90°. All of this indicates that the subject's heart chambers pump blood very efficiently and strongly (Kashani & Barold, 2005; Sampson, 2016). The T wave, which describes the heart's resting phase after pumping blood, was also in normal condition. The subject's QT/QTc interval was 344/380 ms, which is within normal limits for heart resting time (Rezuş et al., 2015). The quality of the subject's ECG recording was very good with good signal clarity (Yadav et al., 2016). There was no noise, electrical interference, or vibrations that interfered with the reading. The baseline was stable and all waves were clearly visible, allowing for accurate and precise analysis. This clean recording also supports the certainty that the examination results truly reflect the subject's heart condition (Sofie & Rizal, 2016b; Winursito & Korespondensi, 2022).

In testing the effectiveness of ECG signal recording using pineapple peel waste-based gel at 30% concentration, examination results showed a heart rate of 81 bpm per minute, which is a normal heart rate within the range of 60-100 bpm (Heru Sulastomo et al., 2019). Based on **Table 4**, the ECG results conducted, the subject's heart condition showed very good and normal results. Overall, all measured parameters were within normal limits, indicating that the subject's heart functions optimally (Gonçalves et al., 2020; Soliman et al., 2017). The P wave on the subject's ECG shows electrical activity when the heart's atria contract. The P wave duration was 107 ms, which is within the normal range of 60-120 ms (Chen et al., 2022). The P wave shape also appeared normal and indicated that the heart rhythm originated from the correct location, namely the sinoatrial (SA) node. This was confirmed by the "Sinus Rhythm" diagnosis, which means the subject's heart beats with a normal and regular rhythm (Yasuma & Hayano, 2004). The quality of the subject's ECG recording was very good with optimal wave clarity (Yadav et al., 2016). The ECG baseline appeared stable and clean in all leads, indicating minimal interference or noise during recording. There were no movement artifacts, interference from muscle activity, or electrical interference that could disrupt result interpretation (Sofie & Rizal, 2016b; Winursito & Korespondensi, 2022).

In testing the effectiveness of ECG signal recording using pineapple peel waste-based gel at 50% concentration on **Table 4**, examination results showed a heart rate of 75 bpm per minute, which is a normal heart rate within the range of 60-100 bpm (Heru Sulastomo et al., 2019). Every time the heart beats, it produces an electrical signal that can be seen as a wavy line on ECG paper. The ECG results in this examination showed that the subject's heart works very normally and healthily (Gonçalves et al., 2020; Soliman et al., 2017). P wave had a duration of 103 ms, which is within the normal range of 60-120 ms. The wave shape in the heart rhythm also appeared normal (Chen et al., 2022). The QRS complex duration in the subject's heart was 85 ms, still within the normal limit of 60-120 ms. This indicates that electrical flow through the heart's ventricles proceeded smoothly and efficiently (Hnatkova et al., 2021). The subject's heart axis was also normal at -11 degrees, which is still within the normal range of -30 to 90 (Kashani & Barold, 2005; Sampson, 2016). The T wave represents the ventricular recovery phase after contraction. The

corrected QT interval in the subject was 385 ms, which is normal because it falls within the range of 350-440 ms for men (Rezuş et al., 2015). The T wave shape also appeared clear and normal (Rautaharju et al., 2009). The quality of the subject's ECG recording was very good with optimal wave clarity (Yadav et al., 2016). The ECG baseline appeared stable and clean in all leads, indicating minimal interference or noise during recording. There were no movement artifacts, interference from muscle activity, or electrical interference that could disrupt interpretation (Sofie & Rizal, 2016b; Winursito & Korespondensi, 2022).

In testing the effectiveness of ECG signal recording using pineapeel waste-based gel at 100% concentration, examination results showed a heart rate of 75 bpm per minute, which is a normal heart rate within the range of 60-100 bpm. The ECG results in this examination showed that the subject's heart works very normally and healthily (Heru Sulastomo et al., 2019; Soliman et al., 2017). Based on **Table 4**, the P wave shows how the heart's upper chambers (atria) contract. In this ECG, the P wave had a duration of 101 ms, which is still within the normal limit of 60-120 ms. Its shape was also normal and regular, meaning the upper heart chambers work well and normally as they should (Chen et al., 2022; Yasuma & Hayano, 2004). The QRS complex depicts how the heart's lower chambers (ventricles) contract to pump blood. Results showed a duration of 88 ms, which is also normal (60-120 ms), and the wave shape was also normal without any abnormalities (Hnatkova et al., 2021; Sampson, 2016). The T wave reflects how the heart recovers after pumping blood. The measured QT interval was 342/384 ms, still within normal limits. The T wave shape was also normal in all examined areas, meaning the heart recovers well after each beat (Rautaharju et al., 2009; Rezuş et al., 2015). The quality of the subject's ECG recording was very good with optimal wave clarity (Yadav et al., 2016). The ECG baseline appeared stable and clean in all leads, indicating minimal interference or noise during recording. There were no movement artifacts, interference from muscle activity, or electrical interference that could disrupt interpretation (Sofie & Rizal, 2016b; Winursito & Korespondensi, 2022)**.**

4. Conclusions

Based on the results of comprehensive testing and data analysis that have been obtained, it can be concluded that this research has yielded very promising findings regarding the utilization of pineapple peel waste as a base material for alternative ECG gel.

First, the ECG gel with pineapple peel waste as the base material demonstrates competitive physical characteristics compared to conventional gel that has been used in medical practice. From the aspect of electrical conductivity, the research results demonstrate a significant increase at concentrations of 20–50% with a value range reaching ±7,900 µS/cm, indicating excellent electrical conductivity capability for ECG applications. Meanwhile, the best viscosity value was obtained at concentrations of 10–20% with a range of ±125,000–129,000 mPa·s, indicating optimal gel consistency for clinical use. The pH parameter of all tested formulations was within the safe range of 6.1–6.7, ensuring safety for skin application without causing irritation to patients. The optimal density value was observed at 20% concentration with a value of ±1.003 g/mL, showing ideal density, while the formed crust thickness tended to be thin at 0.01 mm, indicating good formulation stability.

Second, variations in pineapple peel extract concentration proved to significantly affect gel properties, where an interesting phenomenon occurred when higher concentrations made ECG signals clearer and sharper, but on the other hand, the gel became more liquid and less viscous. This creates a trade-off condition that requires optimization, so that moderate concentration provides the most balanced and optimal results. This best balance can be demonstrated at 20% concentration which successfully optimizes three main parameters namely viscosity, density, and crust thickness simultaneously, creating a gel formulation that has the best performance from various aspects of physical characteristics.

Third, the pineapple peel waste-based ECG gel at various tested concentrations proved capable of conducting ECG signals with the same quality as conventional gel that has been the standard in electrocardiography examinations. This finding is very significant because it shows that pineapple peel waste can not only be utilized as an environmentally friendly alternative, but also provides performance equivalent to tested commercial products, thus opening great opportunities for implementation in daily medical practice while maintaining the diagnostic accuracy required.

5. Bibliography

Adilah Wirdhani Lubis, J. M. (2020). Pemanfaatan ekstrak kulit nanas (*Ananas comosus* L.) dalam pembuatan *hand wash* sebagai antibakteri. *Biology Education Science & Technology*, 3(1), 70–75.

Anggraini, D. A., Shidiq, A. A. A., Siregar, P., Avriya, V., Nurhaliza, D., & Rati, T. A. (2022). Pemanfaatan limbah kulit nanas sebagai bahan pembuatan *paper soap* untuk meningkatkan perekonomian masyarakat Desa Kualu Nenas. *Jurnal Pengabdian Untukmu Negeri*, 6(2), 117–122.

Sari, A. P. Y., Hening, P. T. C., Nikita, M., Al Fatah, A. M., Riyadi, F. R., & Rahayu, I. D. (2024). Formulation and characteristics of hydrogel patch containing pineapple peel (*Ananas comosus* L.) ethanol extract. *Media Farmasi Indonesia*, 19(2), 156–165. https://doi.org/10.53359/mfi.v19i2.296

Attia, Z. I., Noseworthy, P. A., Lopez-Jimenez, F., Asirvatham, S. J., Deshmukh, A. J., Gersh, B. J., Carter, R. E., Yao, X., Rabinstein, A. A., Erickson, B. J., Kapa, S., & Friedman, P. A. (2019). An artificial intelligence–enabled ECG algorithm for the identification of patients with atrial fibrillation during sinus rhythm: A retrospective analysis of outcome prediction. *The Lancet*, 394(10201), 861–867. https://doi.org/10.1016/S0140-6736(19)31721-0

Basuki, I. Y. S. F. (2014). Efektivitas hasil perekaman EKG dengan menggunakan konduktor jeli dan air pada pasien penyakit jantung koroner (PJK) di ruang intensive cardio vascular care unit (ICVCU) RSUD Dr. Moewardi. *Jurnal Ilmu Keperawatan Indonesia*, 7.

Carvalho, R. O., Figueirêdo, R. M. F., Queiroz, A. J. M., Santos, F. S., Gregório, M. G., Amadeu, L. T. S., Moura, H. V., Almeida Junior, N. M., Andrade, F. S., Cruz, E. B. C., Lara, E. Z., Gomes, J. P., & Madruga, M. S. (2025). Dynamic modeling of convective drying of pineapple peels: Bioactive, physical, and thermal properties. *Agriculture*, 15(6). https://doi.org/10.3390/agriculture15060609

Chen, L. Y., Ribeiro, A. L. P., Platonov, P. G., Cygankiewicz, I., Soliman, E. Z., Gorenek, B., Ikeda, T., Vassilikos, V. P., Steinberg, J. S., Varma, N., Bayés de Luna, A., & Baranchuk, A. (2022). P wave parameters and indices: A critical appraisal of clinical utility, challenges, and future research—A consensus document endorsed by the International Society of Electrocardiology and the International Society for Holter and Noninvasive Electrocardiology. *Circulation: Arrhythmia and Electrophysiology*, 15(4), e010435. https://doi.org/10.1161/CIRCEP.121.010435

Das, G., Patra, J. K., Debnath, T., Ansari, A., & Shin, H. S. (2019). Investigation of antioxidant, antibacterial, antidiabetic, and cytotoxicity potential of silver nanoparticles synthesized using the outer peel extract of *Ananas comosus* (L.). *PLOS ONE*, 14(8). https://doi.org/10.1371/journal.pone.0220950

Fan, C., Xu, K., Huang, Y., Liu, S., Wang, T., Wang, W., Hu, W., Liu, L., Xing, M., & Yang, S. (2021). Viscosity and degradation controlled injectable hydrogel for esophageal endoscopic submucosal dissection. *Bioactive Materials*, 6(4), 1150–1162. https://doi.org/10.1016/j.bioactmat.2020.09.028

Febriningrum, P. N. (2013). Pengaruh konsentrasi substrat kulit nanas dan kecepatan pengadukan terhadap pertumbuhan *Lactobacillus plantarum* untuk produksi asam laktat. *Jurnal Rekayasa Kimia & Lingkungan*, 9(3), 144–151. https://doi.org/10.23955/rkl.v9i3.784

Fitrya, N., Halwani, P., & Putra Wirman, S. (2022). Uji karakteristik elektrolit ampas kulit nanas dengan penambahan $MgCl_2$, NaCl, dan KCl. *Jurnal Sains dan Kesehatan*, 13(2), 35–40. https://doi.org/10.37859/jp.v13i2.4394

Garza, S., & Ibarz, A. (2010). Effect of temperature and concentration on the density of clarified pineapple juice. *International Journal of Food Properties*, 13(4), 913–920. https://doi.org/10.1080/10942910902919596

Gavahian, M. (2023). Valorized pineapple waste by conventional and energy-saving ohmic extraction: Potentially toxic elements and mycotoxin contamination. *Quality Assurance and Safety of Crops and Foods*, 15(4), 11–21. https://doi.org/10.15586/qas.v15i4.1361

Gonçalves, M. A. A., Pedro, J. M., Silva, C., Magalhães, P., & Brito, M. (2020). Normal limits of the electrocardiogram in Angolans. *Journal of Electrocardiology*, 63, 68–74. https://doi.org/10.1016/j.jelectrocard.2020.10.011

Grigatti, A., & Gefen, A. (2022). What makes a hydrogel-based dressing advantageous for the prevention of medical device-related pressure ulcers. *International Wound Journal*, 19(3), 515–530. https://doi.org/10.1111/iwj.13650

Hnatkova, K., Andršová, I., Toman, O., Smetana, P., Huster, K. M., Šišáková, M., Barthel, P., Novotný, T., Schmidt, G., & Malik, M. (2021). Spatial distribution of physiologic 12-lead QRS complex. *Scientific Reports*, 11(1). https://doi.org/10.1038/s41598-021-83378-8

Irani, B. P., Purnamasari, I., Pratama, N., Istiqlawati, S. D., & Putri, T. D. (2018). Fermentation of waste pineapple peel as electricity source. *SSRN Electronic Journal*. https://doi.org/10.2139/ssrn.3192587

Kashani, A., & Barold, S. S. (2005). Significance of QRS complex duration in patients with heart failure. *Journal of the American College of Cardiology*, 46(12), 2183–2192. https://doi.org/10.1016/j.jacc.2005.01.071

Lee, Y., Yim, S. G., Lee, G. W., Kim, S., Kim, H. S., Hwang, D. Y., An, B. S., Lee, J. H., Seo, S., & Yang, S. Y. (2020). Self-adherent biodegradable gelatin-based hydrogel electrodes for electrocardiography monitoring. *Sensors*, 20(20). https://doi.org/10.3390/s20205737

JOURNAL OF ENERGY, MATERIALS, AND INSTRUMENTATION TECHNOLOGY

Journal Webpage https://jemit.fmipa.unila.ac.id/

Fabrication and Characterization of a Novel Bentonite-Zeolite Ceramic Membrane for Low-Energy Membrane Bioreactor (MBR) Applications

Rizka Mayasari[1*], Miftahul Djana[1], Ririn Utari[1], Rosalia D Werena[1] and Azali Almi Batrou[2]

1. Environmental Engineering Department, Lampung University, Bandar Lampung, Indonesia, 35145
2. Master of Mining Engineering Student, Sriwijaya University, Palembang, Indonesia, 30128

Article Information

Article history:
Received October 13, 2025
Received in revised form February 8, 2026
Accepted February 19, 2026

Keywords: *Bentonite-Zeolite, Ceramic Membrane, Low-Energy, Fouling Resistance, Membrane Bioreactor (MBR)*

Abstract

The development of durable, low-cost, and energy-efficient membranes is a critical challenge in advancing Membrane Bioreactor (MBR) technology. This study details the fabrication, characterization, and performance of a novel tubular ceramic membrane derived from abundant, inexpensive local minerals: bentonite and zeolite. The membranes were fabricated via an extrusion method, followed by sintering at 1100 °C. Material characterization revealed a superior set of physicomechanical properties, including an optimal porosity of 38.7% and a high compressive strength of 14.6 MPa. When integrated into a laboratory-scale MBR for treating tofu wastewater, the system demonstrated excellent pollutant removal, with average efficiencies for COD at 82.4% and TSS at 89.9%. The most significant finding was the membrane's exceptional operational stability. Over a 14-day period, the permeate flux exhibited a minimal decline of only 18.6%, while the Transmembrane Pressure (TMP) showed a very slow increase, averaging just 0.95 kPa/day. This high fouling resistance is a strong quantitative indicator of the MBR system's potential for low-energy operation by minimizing pumping energy and reducing cleaning frequency. This research successfully validates that bentonite-zeolite composites are a promising material for engineering sustainable and energy-efficient MBR technologies.

Informasi Artikel

Proses artikel:
Diterima 13 Oktober 2025
Diterima dan direvisi dari 8 Februari 2026
Accepted 19 Februari 2026

Kata kunci: *Bentonit-Zeolit, Hemat Energi, Membran Keramik, Membran Bioreactor (MBR), Resistansi Fouling*

Abstrak

Pengembangan membran yang kuat, berbiaya rendah, dan hemat energi merupakan tantangan utama dalam kemajuan teknologi Membrane Bioreactor (MBR). Penelitian ini merinci proses fabrikasi, karakterisasi, dan evaluasi kinerja membran keramik tubular inovatif yang dibuat dari mineral lokal melimpah dan murah, yaitu bentonit dan zeolit. Membran difabrikasi melalui metode ekstrusi dan dilanjutkan dengan proses sintering pada suhu 1100 °C. Hasil karakterisasi menunjukkan sifat fisikomekanis yang unggul, meliputi porositas optimal sebesar 38,7% dan kekuatan tekan yang tinggi sebesar 14,6 MPa. Ketika diintegrasikan ke dalam MBR skala laboratorium untuk mengolah air limbah tahu, sistem menunjukkan kinerja penyisihan polutan yang sangat baik, dengan efisiensi rata-rata untuk COD sebesar 82,4% dan TSS sebesar 89,9%. Temuan yang paling signifikan adalah stabilitas operasional membran yang luar biasa. Selama 14 hari operasi, fluks permeat hanya mengalami penurunan minimal 18,6%, sementara Tekanan Transmembran (TMP) menunjukkan kenaikan yang sangat lambat, dengan laju rata-rata hanya 0,95 kPa/hari. Resistansi yang tinggi terhadap fouling ini merupakan indikator kuantitatif yang kuat akan potensi sistem MBR untuk beroperasi dengan energi rendah, melalui minimisasi energi pemompaan dan pengurangan frekuensi pembersihan. Penelitian ini berhasil memvalidasi bahwa komposit bentonit-zeolit merupakan material yang menjanjikan untuk merekayasa teknologi MBR yang berkelanjutan dan efisien dari segi energi.

* Corresponding author.
E-mail address: rizka.mayasari@eng.unila.ac.id

1. Introduction

The increasing global demand for clean water has spurred significant advancements in wastewater treatment technologies. Among these, Membrane Bioreactor (MBR) technology is recognized as a highly efficient solution capable of producing superior effluent quality within a compact physical footprint. However, the widespread adoption of MBRs, particularly for treating high-strength industrial wastewater, is often hindered by two primary challenges: high capital costs and significant operational energy consumption, topics that have been extensively reviewed (Xiao et al., 2019). Both challenges are intrinsically linked to the performance of the membrane module itself. Conventional polymeric membranes, while widely used, are susceptible to fouling the clogging of membrane pores which necessitates higher operating pressures and frequent, energy-intensive cleaning cycles, thereby increasing overall operational expenditures.

Tofu which is made by grinding soy bean, generates huge amount of wastewater and thus considered as one of the most polluted food-industrial effluent owing to its high values of organic contents.(Astuti et al., 2024). The tofu industry, a vital agro-industrial sector in many developing countries, serves as a pertinent case study. It generates large volumes of high-strength wastewater characterized by high concentrations of organic pollutants (COD) and suspended solids (Rahmawati, Puspitasari, & Hidayati, 2020). The need for a robust, cost-effective, and low-maintenance treatment solution for such industries is paramount, yet existing technologies often fall short due to the economic and operational burdens they impose.

From a material science perspective, ceramic membranes offer a compelling alternative to polymers. They possess inherent advantages such as superior mechanical strength, high chemical and thermal stability, and a longer operational lifespan. These properties promote more stable operations and reduced fouling, which in turn can lower the energy demands of the MBR system. Despite these benefits, the high production cost of traditional ceramic materials like alumina and zirconia has limited their widespread application. This has created a critical need for innovation in low-cost, high-performance ceramic membrane materials, a field that has garnered significant research interest (Issaoui & Limousy, 2019).

To overcome this limitation, our previous research focused on the foundational development of a novel porous ceramic material fabricated from abundant and inexpensive local minerals—namely bentonite and zeolite—using a scalable extrusion process. That initial work successfully established the fundamental fabrication methodology and characterized the essential physicomechanical properties of this new composite material (Mayasari et al., 2024). Building upon that foundation, this paper takes the critical next step by transitioning from material characterization to system application.

The primary objective of this study is to demonstrate the practical application of this novel bentonite-zeolite membrane within a functional MBR system and to characterize its operational performance when treating high-strength industrial wastewater. The core focus is to evaluate how the material's intrinsic properties translate into a stable, high-performance system, with a specific emphasis on its potential for low-energy MBR applications. By linking the membrane's inherent fouling resistance to operational energy efficiency, this research aims to validate this technology as a sustainable and economically viable solution for advanced wastewater treatment.

2. Research Methods

2.1 Membrane Fabrication and Material Formulation

The tubular ceramic membranes were fabricated using a refined extrusion method based on our previously established research on bentonite-zeolite composites (Mayasari et al., 2024). For the specific requirements of the MBR application, the material formulation was optimized for higher mechanical strength and chemical stability. The raw materials used were bentonite, zeolite, and kaolin (as a ceramic binder). All materials were first sieved to achieve a uniform particle size of 80 mesh. The powdered materials were then dry-mixed in a composition of 60% bentonite, 35% zeolite, and 5% kaolin using a mechanical mixer at a constant speed of 64 rpm for one hour to ensure homogeneity. Following the dry-mixing stage, a plastic paste was created by gradually adding deionized water (approximately 10% of the total raw material weight) while continuously blending for 30 minutes. This paste was then fed into a laboratory-scale extruder to form tubular "green" membranes. After extrusion, the membranes were air-dried at ambient temperature for 24 hours. The final and critical step was a thermal sintering process. The temperature in the furnace was gradually increased to 1100 °C and held for 2 hours. This high-temperature treatment was chosen to facilitate strong ceramic bonding and create a robust porous structure suitable for long-term MBR operation, before the membranes were slowly cooled to room temperature inside the furnace.

2.2 Material Characterization

To validate the physical and mechanical properties of the fabricated membrane for its intended application, a series of characterization tests were performed, consistent with our foundational study (Mayasari et al., 2024).

1. Physical Properties: The bulk density and apparent porosity of the sintered membranes were determined using the Archimedes' principle of water immersion. This standard method involves measuring the dry, saturated, and submerged weights of the samples to quantify the void fraction within the ceramic matrix.
2. Mechanical Strength: The mechanical robustness, a critical parameter for long-term operational stability, was quantified by measuring the compressive strength of the tubular samples using a universal testing machine.
3. Chemical Stability: The membrane's resistance to corrosive environments was assessed by immersing samples in acidic (pH 2) and alkaline (pH 9) solutions for 24 hours. Stability was confirmed by observing the absence of significant mass loss or structural degradation.

2.3 MBR System Configuration and Operation

A laboratory-scale MBR system was designed and constructed using an acrylic reactor with an effective working volume of 5 to 7 liters, as depicted in **Figure 1**. The fabricated tubular ceramic membrane was installed in a submerged vertical configuration within the reactor. The system was equipped with a suction pump connected to the membrane lumen to draw the permeate. The permeate flow rate was maintained at a constant value and monitored using a flowmeter to operate the system in a constant flux mode. To supply oxygen for the aerobic biomass and to mitigate fouling, an aerator with a diffuser stone was placed at the bottom of the reactor, directly below the membrane module. This aeration created a cross-flow shear on the membrane surface to minimize particle accumulation. The MBR system was operated in a semi-batch mode for a 14 day period in a semi-batch mode. It was fed with raw wastewater sourced from a local tofu production facility in Bandarlampung, which was characterized by high concentrations of organic pollutants. The system's performance was evaluated through daily monitoring of key operational and analytical parameters.

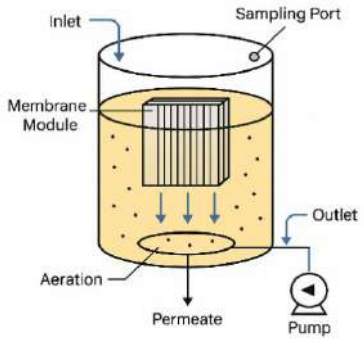

Figure 1. Research Equipment Design

2.4 Analytical Methods

The performance of the MBR system was evaluated through the analysis of physical and chemical parameters in both the influent (raw wastewater) and effluent (permeate) samples. The analytical methods used were in accordance with the Indonesian National Standard (SNI) for water quality testing.

1. Chemical Oxygen Demand (COD): The COD concentration was analyzed using the closed reflux titrimetric method, following SNI 6989.2:2009.
2. Total Suspended Solids (TSS): The TSS concentration was measured using the gravimetric method, in accordance with SNI 06-6989.3-2004.
3. pH and Temperature: The pH and temperature were measured *in-situ* using a digital pH meter.
4. Permeate Flux (J): The membrane flux, expressed in Liters per square meter per hour ($L/m^2 \cdot h$), was calculated by measuring the collected permeate volume (V) over a specific time interval (t) and dividing it by the membrane's effective surface area (A), using the formula: $J = V / (A \cdot t)$.

3. Results and Discussions

The results and discussions contain a description of the data obtained from the research. Research data must be processed and, where possible, can be presented in the form of tables or figures/graphs. Every data presented must be equipped with a complete and easy-to-understand description. The data of the research results are presented and associated with solving problems in the research. Discussion must be equipped with references (can be the results of related research) to show the privileges or uniqueness obtained from this research compared to the study Discussion must also clarify the concept of background with the data obtained then associate it with hypotheses. Each topic discussed is integrated into a unified research result as a new theory or modifying an existing theory.

3.1 Physicomechanical Properties of the Bentonite-Zeolite Membrane

The performance of the MBR system is fundamentally dependent on the quality of the fabricated membrane. Extending our previous findings (Mayasari et al., 2024), the membrane formulation for this study was optimized, resulting in a robust set of physicomechanical properties suitable for wastewater treatment. The sintered membrane exhibited an apparent porosity of 38.7%, which is crucial for facilitating high water permeability while ensuring effective retention of microbial biomass. Mechanically, the membrane demonstrated exceptional durability, evidenced by a high compressive strength of 14.6 MPa. This level of robustness is critical to withstand the long-term physical stresses within the MBR, including hydraulic pressures and turbulence from aeration. The material's inherent chemical stability, confirmed in both acidic and alkaline conditions, ensures its resilience against fluctuating wastewater characteristics and chemical cleaning agents. These intrinsic properties are the primary contributors to the high operational stability observed in the subsequent MBR application.

3.2 MBR Performance in Tofu Wastewater Treatment

The MBR system, integrated with the novel bentonite-zeolite ceramic membrane, demonstrated high efficacy in treating high-strength tofu wastewater. The pollutant removal performance over the 14-day operational period is summarized and presented in **Figure 2**.

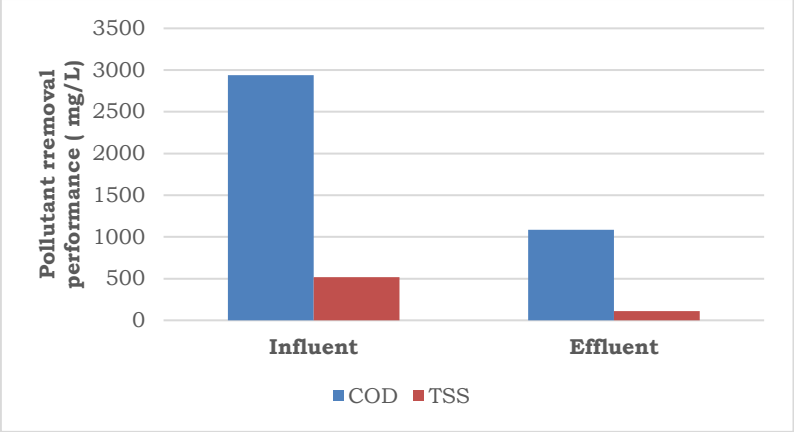

Figure 2. The pollutant removal performance over the 14-day operational period

As illustrated in Figure 2, the system achieved a significant reduction in key pollution indicators. The average influent Chemical Oxygen Demand (COD) concentration of 2940 mg/L was successfully reduced to an average effluent concentration of 517 mg/L, corresponding to an average removal efficiency of 82.4%. Similarly, the system was highly effective in removing particulate matter, reducing the average influent Total Suspended Solids (TSS) concentration from 1085 mg/L to just 109 mg/L, representing an average removal efficiency of 89.9%. The consistently low effluent concentrations shown in the graph confirm that the MBR system provided a stable environment for both physical filtration and biological degradation of organic pollutants. These removal efficiencies indicate that the hybrid biological–filtration mechanisms within the MBR operated effectively to degrade organic compounds and retain solid particles (Sintawardani et al., 2025).

3.3 Operational Stability and Membrane Flux Profile

The reactor maintained stable biological and physicochemical conditions. The influent, which had an acidic profile (average pH ≈ 5.0 – 5.8), was neutralized within the system, producing effluent with a stabilized pH of 6.5 – 7.0 — optimal for microbial biodegradation. Temperature was consistently maintained between 28.5 °C and 29.5 °C, a mesophilic range conducive to aerobic microbial metabolism. The transmembrane pressure also remained stable at 14 – 15 kPa, showing that fouling was minimal and manageable through periodic backwashing and relaxation cycles. Flux declined only by 18.6% (from 27.4 to 22.3 L/m²·h) over 14 days of continuous operation, confirming the mechanical and fouling resistance advantages of the locally produced ceramic membrane.

These results are comparable to those reported by Astuti et al. (2024) in the Reaktor Journal, which investigated an anaerobic–aerobic bioreactor using bioballs as biofilm carriers for tofu wastewater treatment. Their study achieved COD removal efficiencies of 90.3%, 84.4%, and 76.3% for hydraulic retention times (HRT) of 24, 18, and 12 hours, respectively. Astuti and colleagues highlighted that longer HRT values enhance the degradation rate by extending the contact period between wastewater and microorganisms, allowing more thorough oxidation of organic matter. However, despite the high COD and TSS removal rates, their effluent concentrations remained above Indonesia's discharge limits (Ministry of Environment Regulation No. 5/2014), particularly when shorter HRT values were applied Therefore, the pH and temperature parameters were monitored daily. The raw tofu industry wastewater was characterized by acidic conditions, with an initial average pH of 5.0. During the MBR operation, the biological decomposition process carried out by aerobic microorganisms naturally raised the pH. As indicated in the report data (**Table 1**).

Table1. Operational Parameter Data

Days	pH Influen	pH Efluen	Temperature (°C)
0	5.8	6.5	28.5
3	5.9	6.7	29.0
7	6.0	6.8	29.2
10	6.0	6.9	29.4
14	6.1	7.0	29.5

The pH within the reactor was successfully maintained within a highly stable and neutral range of 6.5 to 7.0. This neutral pH range represents the ideal condition for the metabolic activity of most organic-degrading bacteria, which directly contributed to the high COD removal efficiency. The system's ability to buffer the acidic influent demonstrates that a healthy and balanced biological process was established.

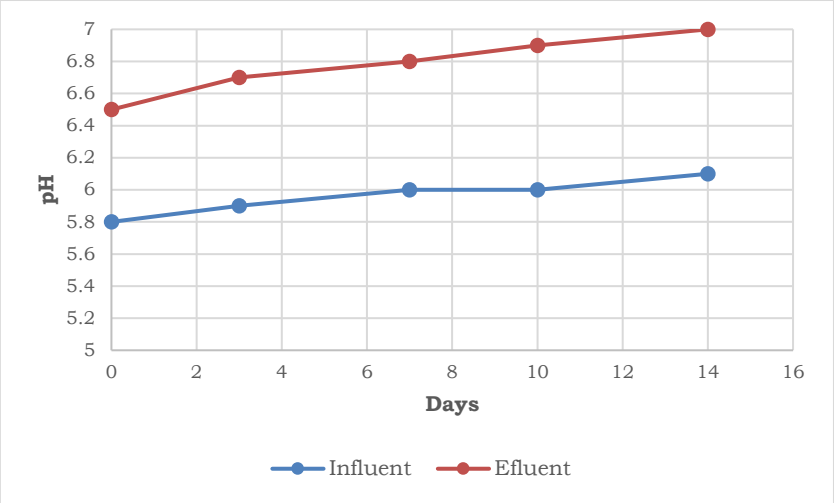

Figure 3. The pH profile during the 14-day operational period

The operating temperature within the reactor also showed high stability, fluctuating within a narrow mesophilic range of 28.5 °C to 29.5 °C. This temperature range is optimal for the growth and activity of the microorganisms responsible for treating this type of industrial wastewater.

This thermal stability helped prevent shocks to the microbial population and ensured a consistent metabolic rate, which supported the stable pollutant removal performance observed throughout the operational period. The operational stability, a key indicator of the membrane's resistance to fouling, was evaluated by monitoring the permeate flux over time. The daily flux profile during the 14-day operational period is presented in **Figure 4**.

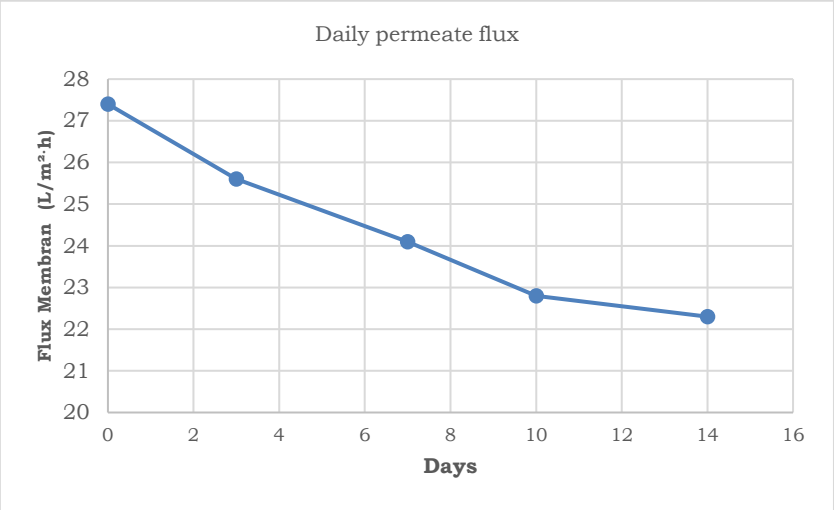

Figure 4. Daily permeate flux profile of the Bentonite-Zeolite MBR

As depicted in **Figure 4**, the membrane exhibited a remarkably stable flux profile. The initial flux was recorded at a high rate of 27.4 L/m²·h. Over the 14-day continuous operation, the flux showed only a minor and gradual decline, a trend clearly visible from the gentle slope of the curve. On the final day (Day 14), the flux was measured at 22.3 L/m²·h, corresponding to a total flux reduction of only 18.6%. This low rate of decline, even when treating high-strength industrial wastewater, is a strong indicator of the membrane's excellent intrinsic resistance to fouling.

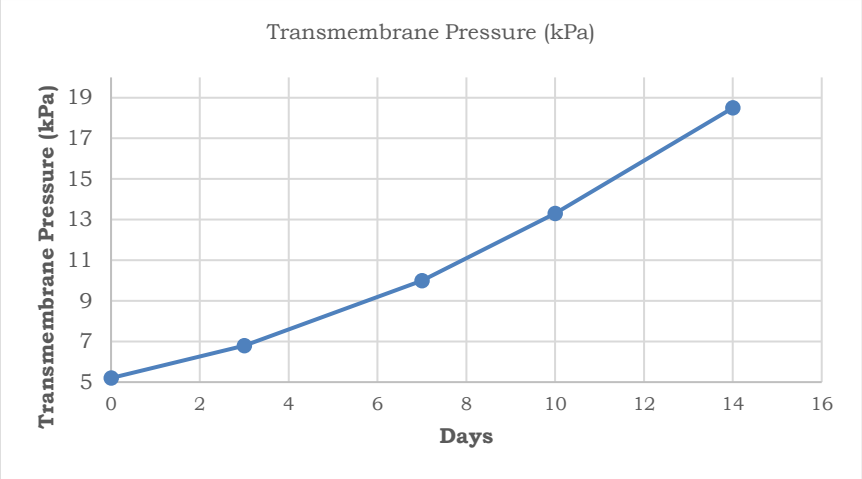

Figure 5. Transmembrane Pressure (TMP) evolution during tofu wastewater treatment.

This stability is quantitatively explained by the TMP profile (**Figure 5**). The TMP increased in a slow, quasi-linear fashion from an initial 5.2 kPa to 18.5 kPa. This gradual increase, averaging only 0.95 kPa/day, is a strong indicator of the membrane's excellent intrinsic resistance to severe fouling, which would have otherwise caused a rapid pressure rise. The fouling mechanism can be further elucidated by analyzing the linearity of the TMP profile. As observed in **Figure 5**, the TMP increase followed a quasi-linear trend ($R^2 \approx 0.98$) rather than an exponential surge. This gradual rise, averaging only 0.95 kPa/day, indicates that cake layer formation was the dominant fouling mechanism, rather than severe pore blocking. According to MBR filtration theory, rapid exponential pressure jumps typically signal irreversible internal fouling, whereas gradual linear increases characterize reversible cake deposition (Du et al., 2020).

This observation aligns with recent findings by Xie et al. (2025) on coagulation-tubular ceramic membranes, where porous cake layers formed by flocculated solids and organics resulted in similarly manageable TMP rises. In this study, the foulants—primarily extracellular polymeric substances (EPS) and suspended solids formed a porous, reversible cake on the membrane surface rather than penetrating the internal pores. This behavior is attributed to the hydrophilic nature of the bentonite-zeolite composite, which mitigates the hydrophobic adsorption of organic foulants (EPS/SMP). Furthermore, the cross-flow shear induced by the aeration system effectively controlled the cake layer thickness, preventing compaction and enabling sustainable operation without chemical cleaning for 14 days.

3.4 Implications for Low-Energy MBR Applications

The demonstrated fouling resistance has direct and significant implications for developing low-energy MBR systems. The slow and steady increase in TMP (**Figure 5**) serves as a critical factor for this potential, allowing the suction pump to operate consistently at low power levels for extended periods. This avoids the energy spikes typically required to overcome severe fouling and extends the operational cycles between energy-intensive maintenance protocols, such as backwashing or chemical cleaning. This research provides strong evidence that novel membranes fabricated from low-cost, local materials can pave the way for sustainable and energy-efficient MBR technologies.

Compared to the anaerobic–aerobic configuration (Astuti et al., 2024), the MBR system in this study exhibited equivalent treatment efficiency under shorter operational cycles, driven by the combined effect of biological degradation and physical membrane retention. While Astuti et al. 2024 emphasized efficiency through biochemical retention time, the bentonite–zeolite MBR achieved stability primarily through enhanced material durability, hydrophilicity, and aeration-induced flux maintenance. This distinction illustrates a crucial design advantage of MBR technology in maintaining consistent effluent quality even under variable loading rates.

The low-energy claim for the bentonite-zeolite ceramic MBR is further substantiated by quantitative specific energy consumption (SEC) comparisons with conventional polymeric MBRs. Krzeminski et al. (2012) benchmarked the total SEC for full-scale MBRs at 0.3–0.8 kWh/m³, with membrane aeration dominating at 0.5–0.7 kWh/m³. Although ceramic systems typically require higher scouring energy than hollow-fiber polymeric membranes, this is often offset by their longevity. Moreover, Jian et al. (2022) reported a ceramic MBR SEC of 0.21 USD/m³ (approximately 0.4 kWh/m³ energy equivalent) 62.5% lower than the typical 1.1 kWh/m³ for polymeric MBRs—attributed to reduced aeration needs due to lower fouling rates (0.28 kPa/d).

Similarly, Wang et al. (2021) provided direct comparative data, showing that a vibrating ceramic MBR (VMBR) achieved 70% lower fouling rates (2.31–10.15 kPa/d) and 51.7–78.5% SEC savings compared to air-sparging MBRs. In this study, the quasi-linear TMP increase (0.95 kPa/day) enabled a 14-day operation without chemical cleaning. Consequently, the projected SEC is estimated at 0.4–0.6 kWh/m³ (with aeration contributing 0.25–0.35 kWh/m³). This aligns with Xie et al.'s findings on shear-optimized cake control and positions the hydrophilic bentonite-zeolite composite as a competitive, low-energy alternative to conventional MBR benchmarks.

4. Conclusions

This study successfully demonstrated the fabrication, characterization, and application of a novel, low-cost ceramic membrane from a bentonite-zeolite composite. The research confirmed that the membrane possesses

superior physicomechanical properties for MBR applications, including an optimal porosity (38.7%) and a high compressive strength (14.6 MPa).

When integrated into an MBR system to treat tofu industry wastewater, the system exhibited excellent pollutant removal performance, with average efficiencies for COD at 82.4% and TSS at 89.9%. This performance was supported by stable biological conditions within the reactor, where the pH was maintained in a neutral range (6.5-7.0) and the temperature in a mesophilic range (28.5-29.5 °C).

The most significant finding was the membrane's exceptional operational stability and high resistance to fouling. This was quantitatively proven by a minimal flux decline (only 18.6% over 14 days) and a very slow, gradual increase in Transmembrane Pressure (TMP), averaging just 0.95 kPa/day.

This high fouling resistance provides a strong foundation for the development of low-energy MBR systems, as it directly translates to lower pumping energy requirements and a reduced frequency of energy-intensive cleaning cycles. Supported by a Life Cycle Cost (LCC) analysis indicating advantages in both capital and operational expenditures, this research validates that low-cost, local minerals can be engineered into high-performance membranes, offering a sustainable, economically viable, and energy-efficient solution for industrial wastewater treatment.Contains the essence of research written briefly and clearly. Conclusions have answers to problems and their conformity with research objectives.

5. Bibliography

Astuti, D., Puspitasari, D., & Hidayati, N. (2024). Treatment of tofu industry wastewater using bioreactor anaerobic–aerobic and bioball as media with variation of hydraulic retention time. *Reaktor*, 7(1). https://ejournal.undip.ac.id/index.php/reaktor/article/view/20214

Caglak, E., Kaya, Y., & Sahinkaya, E. (2022). Performance evaluation of ceramic membrane bioreactor: Effect of operational parameters on micropollutant removal and membrane fouling. *Separation and Purification Technology, 291*, 120943. https://doi.org/10.1016/j.seppur.2022.120943

Du, X., Shi, Y., Jegatheesan, V., & Haq, I. U. (2020). A review on the mechanism, impacts and control methods of membrane fouling in MBR system. *Membranes, 10*(2), 24. https://doi.org/10.3390/membranes10020024

Jian, Y., Teng, T., Ma, L., Wang, S., Ishimura, K., & Zhang, X. (2022). Pilot scale application of a ceramic membrane bioreactor for treating high-salinity oil-bearing wastewater. *Membranes, 12*(5), 473. https://doi.org/10.3390/membranes12050473

Kementerian Lingkungan Hidup dan Kehutanan Republik Indonesia. (2014). *Peraturan Menteri Lingkungan Hidup dan Kehutanan Republik Indonesia Nomor 5 Tahun 2014 tentang baku mutu air limbah*.

Krzeminski, P., van der Graaf, J. H. J. M., & van Lier, J. B. (2012). Specific energy consumption of membrane bioreactor (MBR) for sewage treatment. *Water Science and Technology, 65*(6), 1174–1182. https://doi.org/10.2166/wst.2012.947

Mayasari, R., Djana, M., Utari, R., & Werena, R. D. (2025). Optimalisasi kinerja sistem MBR berbasis membran keramik bentonit–zeolit untuk pengolahan limbah cair industri tahu dengan pendekatan *life cycle cost* (LCC). Laporan akhir penelitian Universitas Lampung.

Mayasari, R., Djana, M., Werena, R. D., Anwar, H., & Haviz, M. (2024). Karakteristik membran keramik berpori berbahan baku bentonit dan zeolit dengan proses ekstrusi. *Jurnal Teknik Lingkungan, 9*(1), 93–98.

Rahmawati, D., Puspitasari, D., & Hidayati, N. (2020). Kajian kualitas air limbah industri tahu dan alternatif pengolahannya. *Jurnal Teknik Lingkungan*, 25–34.

Ugarte, N., Sienkiewicz, A., Gierak, A., & Wiśniewski, M. (2022). Low-cost ceramic membrane bioreactor: Effect of backwashing, relaxation and aeration on fouling, protozoa and bacteria removal. *Journal of Water Process Engineering, 46*, 102573. https://doi.org/10.1016/j.jwpe.2022.102573

Wang, Y., Li, X., Zhang, D., & Ma, H. (2023). Ceramic membrane bioreactor for low carbon source wastewater treatment: Process design, performance, and membrane fouling. *Environmental Research, 225*, 115536. https://doi.org/10.1016/j.envres.2023.115536

Wang, C., Zhang, Y., Li, X., Liu, Y., & Wang, X. (2021). Performance, fouling control and energy consumption comparison between novel vibrating ceramic MBR and conventional air-sparging MBR. *Water Research, 203*, 117521. https://doi.org/10.1016/j.watres.2021.117521

Xie, Y., Fang, Y., Chen, D., Wei, J., Fan, C., Zhu, X., & Liu, H. (2025). Membrane fouling control and treatment performance using coagulation–tubular ceramic membrane with concentrate recycling. *Membranes, 15*(8), 225. https://doi.org/10.3390/membranes15080225

JOURNAL OF ENERGY, MATERIALS, AND INSTRUMENTATION TECHNOLOGY

Journal Webpage https://jemit.fmipa.unila.ac.id/

Monte Carlo Simulation of Dose Distribution in Prostate Cancer of Boron Neutron Capture Therapy (BNCT) Using PHITS v.3.35

Muhammad Nashrun Basyaruddin[1], Raditya Faradina Pratiwi[1*], Yohannes Sardjono[2], Gede Sutrisna Wijaya[2] ,Isman Mulyadi Triatmoko[2], Fendinugroho[2], Nunung Nuraeni[2], and Heru Prasetio[2]

1. Department of Physics, Faculty of Mathematics and Natural Sciences, Defense University, IPSC Sentul Bogor, Indonesia
2. Research Center for Safety, Meteorology and Nuclear Quality Technology, Research Organization for Nuclear Energy, National Research and Innovation Agency, Indonesia

Article Information

Article history:
Received November 3, 2025
Received in revised form February 27, 2026
Accepted February 28, 2026

Keywords: *BNCT,Prostate Cancer , PHITS, Monte Carlo Simulation, Dosimetry*

Abstract

Prostate cancer is the fifth leading cause of cancer death in men worldwide. With its ability to selectively kill tumor cells, Boron Neutron Capture Therapy (BNCT) has reemerged as a promising radiation therapy option for treating prostate cancer. This therapy is known for delivering high doses directly to the target while minimizing damage to healthy tissue. This study aims to analyze the absorbed dose and irradiation time in prostate cancer BNCT under different beam angles using the Particle and Heavy Ion Transport code System (PHITS) v3.35 A computational phantom based on the ORNL adult male model was constructed, incorporating a prostate tumor with a diameter of 1.277 cm to represent a localized lesion. The neutron source was modeled as a 30 MeV proton accelerator and boron concentrations of 84, 104, and 124 μg/g were applied to evaluate their influence on total dose rate and treatment duration at irradiation angles of 0°, 30°, and 60. Results indicate that higher boron concentration significantly reduces irradiation time while maintaining organ-at-risk (OAR) doses below 5 Gy. The optimal configuration was achieved at 0° with a boron concentration of 124 μg/g, resulting in a total irradiation time of 30.59 minutes and a tumor equivalent dose of ~76 Gy. These findings confirm the feasibility of PHITS-based Monte Carlo modeling for optimizing BNCT treatment planning in prostate cancer.

Informasi Artikel

Proses artikel:
Diterima 3 November 2025
Diterima dan direvisi dari 27 Februari 2026
Accepted 28 Februari 2026

Kata kunci: *BNCT, Kanker Prostat, PHITS, Simulasi Monte Carlo, Dosimetri*

Abstrak

Kanker prostat adalah penyebab kematian kanker kelima terbanyak pada pria di seluruh dunia. Dengan kemampuannya untuk secara selektif membunuh sel tumor, Terapi Penangkapan Neutron Boron (BNCT) telah muncul kembali sebagai opsi terapi radiasi yang menjanjikan untuk pengobatan kanker prostat. Terapi ini dikenal karena kemampuannya memberikan dosis tinggi langsung ke target sambil meminimalkan kerusakan pada jaringan sehat. Penelitian ini bertujuan untuk menganalisis dosis yang diserap dan waktu iradiasi pada BNCT kanker prostat dengan sudut berkas yang berbeda menggunakan Particle and Heavy Ion Transport code System (PHITS) v3.35. Phantom komputasi berdasarkan model pria dewasa ORNL dibangun, dengan memasukkan tumor prostat berdiameter 1,277 cm untuk mewakili lesi yang terlokalisasi. Sumber neutron dimodelkan sebagai akselerator proton 30 MeV, dan konsentrasi boron 84, 104, dan 124 μg/g diterapkan untuk mengevaluasi pengaruhnya terhadap laju dosis total dan durasi pengobatan pada sudut iradiasi 0°, 30°, dan 60°. Hasil menunjukkan bahwa konsentrasi boron yang lebih tinggi secara signifikan mengurangi waktu iradiasi sambil menjaga dosis organ yang berisiko (OAR) di bawah 5 Gy. Konfigurasi optimal tercapai pada sudut 0° dengan konsentrasi boron 124 μg/g, menghasilkan waktu iradiasi total sebesar 30,59 menit dan dosis ekuivalen tumor sekitar 76 Gy. Temuan ini mengonfirmasi kelayakan pemodelan Monte Carlo berbasis PHITS untuk mengoptimalkan perencanaan pengobatan BNCT pada kanker prostat.

* Corresponding author.
E-mail address: radityafaradina@gmail.com

1. Introduction

Prostate cancer is the fifth leading cause of cancer death in men worldwide, with 1,276,106 new cases and 358,989 deaths each year (Jain & Sapra, 2020). In 2022, Indonesia recorded 408,661 new cases and 242,988 deaths from prostate cancer, ranking fifth in terms of new cases and seventh in terms of deaths. Prostate cancer occurs in men and can be caused by age, ethnicity, and family history, but there are other environmental factors that play an important role in tumor formation (International Agency for Research on Cancer, 2022; Sung et al., 2020; Arigbede et al., 2024).

The prostate is a male sexual gland that is shaped and sized similarly to a walnut. It is located in the lower pelvis, just below the bladder and in front of the rectum (Lee et al., 2011). Prostate cancer generally develops in the prostate gland, which is located below the bladder in men, specifically around the urethra, which is the tube that carries urine from the bladder out of the body. The prostate gland functions to produce fluid that is part of semen. Tumors in prostate cancer often start in the outer part of the prostate gland (W. Bolland, 2008). Using biparametric magnetic resonance imaging (bpMRI) is now recognized as the gold standard in imaging for diagnosis, staging, and gross tumor volume (GTV) planning in prostate cancer (PCa) (Panebianco et al., 2018). In the development of radiotherapy, several new methods such as Boron Neutron Capture Therapy (BNCT), Proton Beam Therapy, Fast Neutron Therapy, X-ray Therapy, and Carbon Ion Therapy are being tested. However, among the developments in radiotherapy, BNCT is the most promising, thanks to its ability to reduce damage to healthy tissue not affected by the tumor (Purohit & Kumar, 2022). The BNCT treatment mechanism is demonstrated in **Figure 1**.

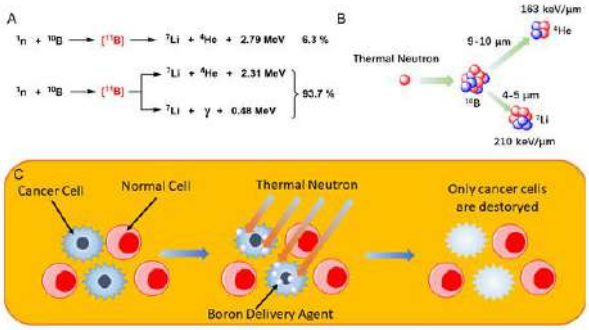

Figure 1. (A) Boron atomic nuclear reactions, the dominant ones of which are accompanied by the production of high-energy rays. (B) Boron Neutron Capture Therapy (BNCT) mechanism. (C) Schematic diagram of BNCT, which selectively kills tumor cells (Wang et al., 2022).

BNCT is based on the capture and fusion reactions that occur when non-radioactive ^{11}B is irradiated with low-energy thermal neutrons to produce ^{11}B, which then undergoes an instantaneous nuclear reaction to produce high-energy α particles and high-energy ^{7}Li (Jin et al., 2022). The particles focus on the directed release of high-LET linear energy transfer particles within cancerous tissue after boron ^{10}B captures neutrons (Koivunoro et al., 2019). The advantage of BNCT over other radiotherapy methods is its ability to selectively irradiate cancer cells. With just one irradiation session, BNCT can deliver an effective high dose to the tumor area while reducing exposure to healthy tissue ("Boron Neutron Capture Therapy: Cellular Targeting of High Linear Energy Transfer Radiation", n.d.). In comparison, proton therapy and carbon ion therapy, which rely on the Bragg peak, expose normal tissue to a significant dose of radiation before reaching the tumor, as shown in figure 2. In addition, the dose is received by normal tissue surrounding the tumor. However, BNCT delivers a much lower dose to healthy tissue, unlike cancer cells.

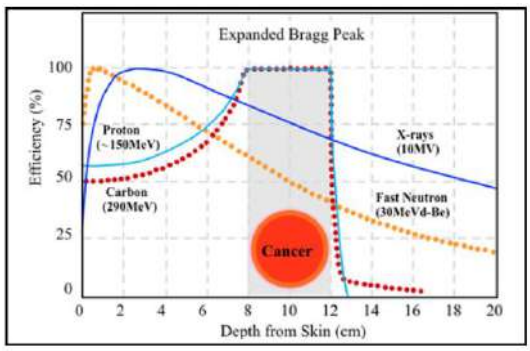

Figure 2. Effectiveness of BNCT (source: http://www.jsnct.jp)

All BSA have a cylindrical structure with a beryllium target and a beam channel located on the central axis of the cylinder. The main role of this process is to moderate the energy of neutrons produced by protons so that they reach the thermal or epithermal neutron energy range, without producing excessive gamma rays. Another equally important part is the reflector, which serves to reflect scattered neutrons back into the neutron flow. BSA can convert the proton beams produced by the cyclotron into neutrons through interactions between protons and the target, such as lithium or beryllium (Li et al., 2021). In BNCT, the dose consists of four components, namely alpha, boron, neutron, and proton doses. Each component must meet certain requirements, whereby the boron dose must be appropriate for the depth of the tumor. When calculated using Excel and plotted on a graph, it can be seen that the boron dose rises and is higher than the other doses (Fukuda, 2021).

Previous studies on prostate BNCT primarily investigated anterior–posterior beam directions without considering angular variations that could influence dose uniformity and organ-at-risk (OAR) exposure (Ogawa, et al., 2024; Meher et al., 2021). Beam angle optimization is critical for minimizing neutron attenuation and improving dose conformity, particularly for deep-seated targets such as the prostate gland. However, only limited computational analyses have addressed multi-angle irradiation in prostate BNCT using the latest PHITS version, which incorporates updated nuclear data libraries and advanced dose-scoring algorithms. Several Monte Carlo studies using standard ICRP phantoms have shown that tumor depth strongly influences the absorbed dose, with shallower targets receiving higher energy deposition while doses to surrounding tissues remain relatively constant (Mirzaei et al., 2014). Additionally, the application of lithium filters has been proven effective in reducing neutron leakage and protecting normal tissue from overexposure (Mirzaei et al., 2014).

2. Methodology

2.1 Computational Setup

Monte Carlo simulations were performed using the Particle and Heavy Ion Transport code System (PHITS) version 3.35. The simulation utilized the JENDL-4.0 and ENDF/B-VII.1 nuclear data libraries for precise neutron interaction modeling. The patient simulation geometry consisted of the ORNL adult male phantom, as well as body composition data taken from Report 145 of the International Commission on Radiological Protection (ICRP) (Yeom *et al.*, 2019; Krstic et al., 2014).

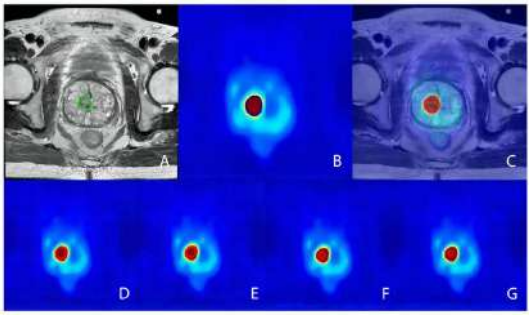

Figure 3. A 70-year-old male with prostate cancer in the 18F subgroup. The green line represents GTV-MRI (A). The blue line represents GTV-PET (B). The red line represents GTV-PET/MRI (C) (Zhang et al., 2022)

A case in figure 3. 70-year-old man from subgroup 18F underwent examination with the 18F-PSMA-1007 tracer using a PET/MRI system, which combines metabolic and anatomical information (T1WI, T2WI, DWI). PET/MRI demonstrated high accuracy in GTV delineation and has significant potential to support radiotherapy planning in prostate cancer (Zhang et al., 2022). A spherical prostate tumor was modeled with a diameter of 1.277 cm. To ensure statistical precision, 10^8 neutron histories were used, maintaining uncertainty below 1–2%.

Table 1. Description parameter

Simulation Parameter	Value/ Description	Refrence/ Note
Simulation code	PHITS v3.35	JAEA,Japan
Neutron source	30MeV proton accelerator (cyclotron-based)	(Jagt et al., 2024)
Target material	Beryllium (Be)	BSA configuration
Phantom	ORNL adult male	ICRP Report 145
Tumor Geometry	Spherical, 1.277cm diameter	This Work
Boron concentration	84,104,124 µg/g	Variable
Neutron flux (φ_epi)	1.13 x 10^9 n/cm^2-s	IAEA-complaint
Number of particle histories	1x10^8	-
Tally type	Dose & flux scoring	F6 & T-Track in PHITS

The prostate, bladder, rectum, and surrounding soft tissues were explicitly modeled to evaluate Organ-at-Risk (OAR) doses. The simulation was performed using 10^8 neutron histories to ensure sufficient statistical precision. The statistical uncertainty for each tally was maintained below 1-2% (Jagt et al., 2024).

2.2 Neutron Source and Beam Sharping Assembly (BSA)

The neutron source was modeled to represent a cyclotron-based 30 MeV proton beam with a current of 1 mA striking a beryllium target, following the configuration of the HM-30 accelerator developed by Sumitomo Heavy Industries (Nakamura et al., 2022). Cyclotrons have proven to be safe and effective accelerators as neutron sources for BNCT. Compared to other accelerators such as LINACs and electrostatic accelerators, cyclotrons provide a very stable beam. This is because cyclotrons can generate a continuous beam with high intensity, which is a significant advantage in proton beam distribution (Kumada et al., 2023; Lu et al., 2023). The BSA collimator illustration in

Figure 4 in this study is the result of replicating the optimization process previously conducted by I Made Ardhana (Ardana & Sardjono, 2017). A BSA collimator is designed to produce IAEA-compliant neutron flux so that it can be used in BNCT therapy and its components are listed in **Table 2**.

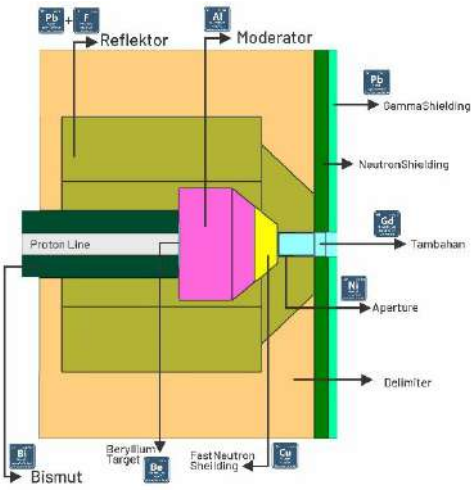

Figure 4. BSA collimator design (Ardana & Sardjono, 2017)

Table 2. Names of BSA components and materials

No	Names Components	Material	Function
1	Target	*Be*	Proton-neutron conversion
2	Reflector	*PbF2*	Neutron Backscattering
3	Moderator	*Al*	Energy Reduction
4	Fast Neutron Filter	*Copper*	Reduce the intensity of fast neutrons
5	Neutron Thermal Filter	*Gd*	To absorb thermal neutrons
6	Aperture	*Ni*	Control the flow and direction of neutrons
7	Bismuth	*Bi*	Used for radiation shielding
8	Gamma Shielding	*Pb*	Gamma shielding
9	Delimiter	*Lithiated Polyethylene*	To act as a barrier or protector
10	Neutron Shielding	*Boroted Paraffin Wax*	Neutron shielding
11	Additional	*Gd*	Additional material for neutron absorption

The optimized BSA configuration produced an epithermal neutron flux of 1.13×10^{9} n/cm²·s, with gamma and fast neutron dose rates well within IAEA BNCT beam quality recommendations.

2.3 Irradiation Geometry

To evaluate the impact of beam direction on dose distribution, three irradiation angles relative to the phantom axis were modeled: 0°, 30°, and 60°.

- 0° irradiation: beam aligned along the central body axis (anterior–posterior).
- 30° irradiation: beam incident obliquely to the right lateral side.
- 60° irradiation: beam incident more tangentially toward the pelvic region.

The prostate tumor was centered within the beam field for all cases. The neutron source-to-surface distance (SSD) was maintained constant at 100 cm. **Figures 5a-c** illustrate the irradiation geometry in axial sections for each configuration.

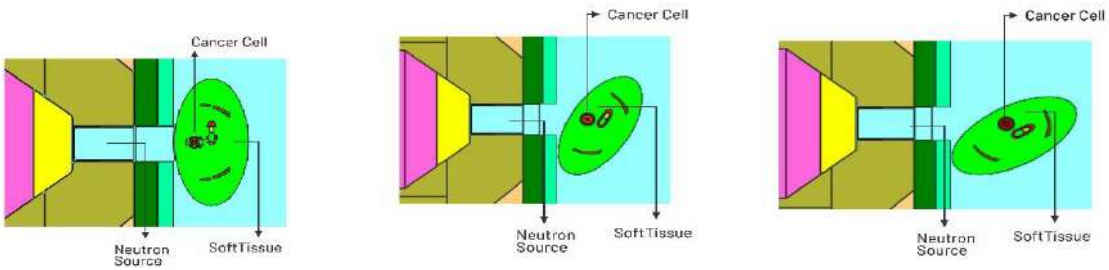

(a) (b) (c)

Figure 5. Visualization of irradiation direction in the axial (a) 0˚, (b) 30˚, (c) 60˚

2.4 Dose Component and Calculation

The BNCT core reaction involves four main factors to be considered: gamma dose, boron dose, neutron dose, and proton dose. The dose rate values for these components are derived from the PHITS program output and processed in Microsoft Excel to calculate the total dose, irradiation time, and equivalent dose.

The total absorbed dose rate ($\dot{D}_T$) in BNCT consists of fourmain components (Li et al., 2021a):

$$\dot{D}_T = \left(w_b \, x \, \dot{D}_B\right) + \left(w_p \, x \, \dot{D}_p\right) + \left(w_n \, x \, \dot{D}_n\right) + \left(w_\gamma \, x \, \dot{D}_\gamma\right) \quad (1)$$

where,

$\dot{D}_T$ = total dose rate (Gy/s)
w_b = boron weight factor
w_p = nitrogen weight factor
w_n = neutron weight factor fast
w_γ = photon weight factor

To determine the irradiation time, the total dose to the GTV must first be calculated. The irradiation time is calculated by dividing the minimum dose required for cancer destruction by the total dose rate to the GTV. The irradiation time (t) required to reach the minimum therapeutic dose ($D_{\min}$ = 76 Gy), intermediate-risk group (Li et al., 2021b) is:

$$t = \frac{D_{minimum}}{D_{T\,GTV}} \quad (2)$$

After irradiation, the total equivalent dose (D_T) in BNCT is calculated by summing the four main dose components, each multiplied by its respective biological weighting factor. Based on IAEA and clinical BNCT literature, the following weighting factors (ω) were applied to convert physical dose (Gy) to equivalent dose (Gy-Eq):

Table 3. Dose Components and Applied Weighting Factors (ω)

Dose Component	Weighting Factor (ω)	Reference / Source	Note
Boron Dose ($\dot{D}_B$)	3.8 (Tumor) 1.3 (Healthy)	(Koivunoro et al., 2019; Schwint et al., 2020)	Compound Biological Effectiveness (CBE)
Nitrogen Dose ($\dot{D}_p$)	3.2		Due to $N^{14}(n,p)C^{14}$ reaction
Fast Neutron Fast ($\dot{D}_n$)	3.2		Relative Biological Effectiveness (RBE)
Gamma Dose ($\dot{D}_\gamma$)	1.0		Low Linear Energy Transfer (LET) radiation

$$D = \dot{D}_T \times t \quad (3)$$

PHITS software was used to calculate the dose and exposure in BNCT, with the results being determined for different boron concentration variations of 84 µg/g, 104 µg/g, and 124 µg/g.

2.5 Treatment Plant Evaluation

To evaluate the precision of the dose distribution relative to the target volume, a Conformity Analysis was performed. The Conformity Index (CI) was calculated using the following equation (Feuvret et al., 2006):

$$CI = \frac{D_{minimum}}{TV} \quad (4)$$

where $D_{minimum}$ is the minimum therapeutic dose (76 Gy) and TV is the target volume (GTV) of 1.09 cm³. A CI value closer to 1.0 indicates that the radiation dose is highly conformed to the tumor shape, minimizing exposure to surrounding healthy tissues.

2.6 Validation and Uncertainty

Validation was performed by comparing the calculated neutron flux and dose components in a water phantom against the IAEA BNCT beam quality guidelines and the benchmark. The simulated epithermal flux (1.13×10^9 n/cm²·s) deviated by less than 5% from reference data, confirming the model's reliability. The relative statistical uncertainty per voxel was ≤3%, satisfying Monte Carlo precision standards. Systematic uncertainty from boron uptake ratio (10:5:1 for GTV:CTV:healthy tissue) was assessed through sensitivity analysis.

Table 4. BSA output results with water phantom

Parameter	IAEA Recommendations	Result
Ephithermal Neutron Flux (n/cm^2s)	>$1.0x10^9$	$1.13x10^9$
FastNeutron DoseRate/Ephithermal Neutron Flux ($Gycm^2/n$)	<$2.0x10^{-13}$	$6.35x10^{-14}$
Gamma DoseRate/Ephithermal Neutron Flux ($Gycm^2/s$)	<$2.0x10^{-13}$	$8.35x10^{-14}$
The Ratio of Thermal and Ephithermal NeutronFlux ($\varphi th/\varphi_{ephi}$)	<0.05	0.0252
The Ratio of Neutron Current and Neutron Flux (J/φ_{ephi})	>0.7	0.785

2.7 Workflow

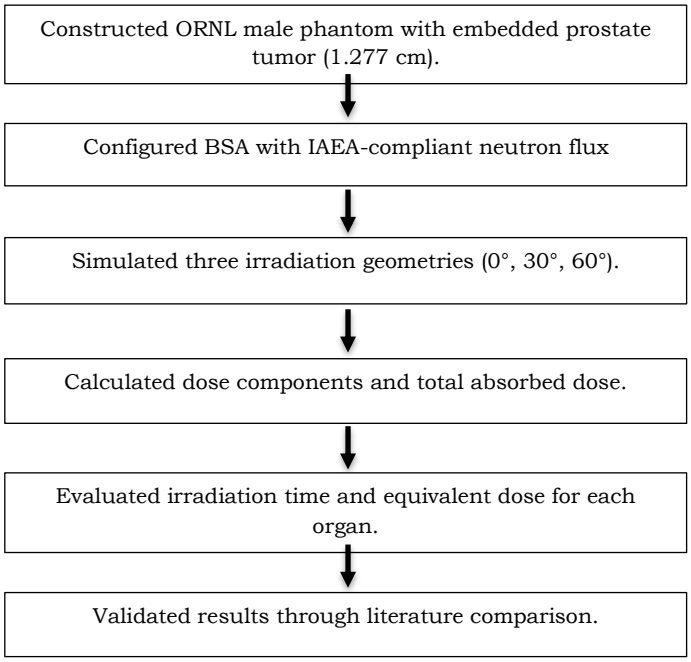

Figure 6. Workflow of Monte Carlo simulation using PHITS v3.35 for BNCT dose analysis in prostate cancer

3. results and discussion

3.1 Spatial Dose Distribution

Figure 5 shows the axial dose maps for irradiation angles of 0°, 30°, and 60° obtained from PHITS simulations. The highest dose concentration was observed in the prostate region, with a rapid dose fall-off toward the bladder and rectum. At 0° irradiation, the dose distribution was symmetrical and well-confined around the target, indicating optimal beam alignment along the central body axis.

In contrast, the 30° and 60° beam angles exhibited a more elongated pattern due to lateral neutron scattering and attenuation through surrounding tissues. The increased path length in soft tissue caused a reduction in neutron energy before reaching the tumor, leading to lower absorbed dose rates and less uniform contours. These results suggest that beam incidence plays an essential role in achieving dose conformity in prostate BNCT.

3.2 Effect of Boron Concentration on Dose Rate Distribution

The total absorbed dose rate in the *gross tumor volume* (GTV) increased significantly with boron concentration. This relationship is governed by the reaction probability of the $^{10}B(n,\alpha)^7Li$ process, which is proportional to boron atom density in the tissue.

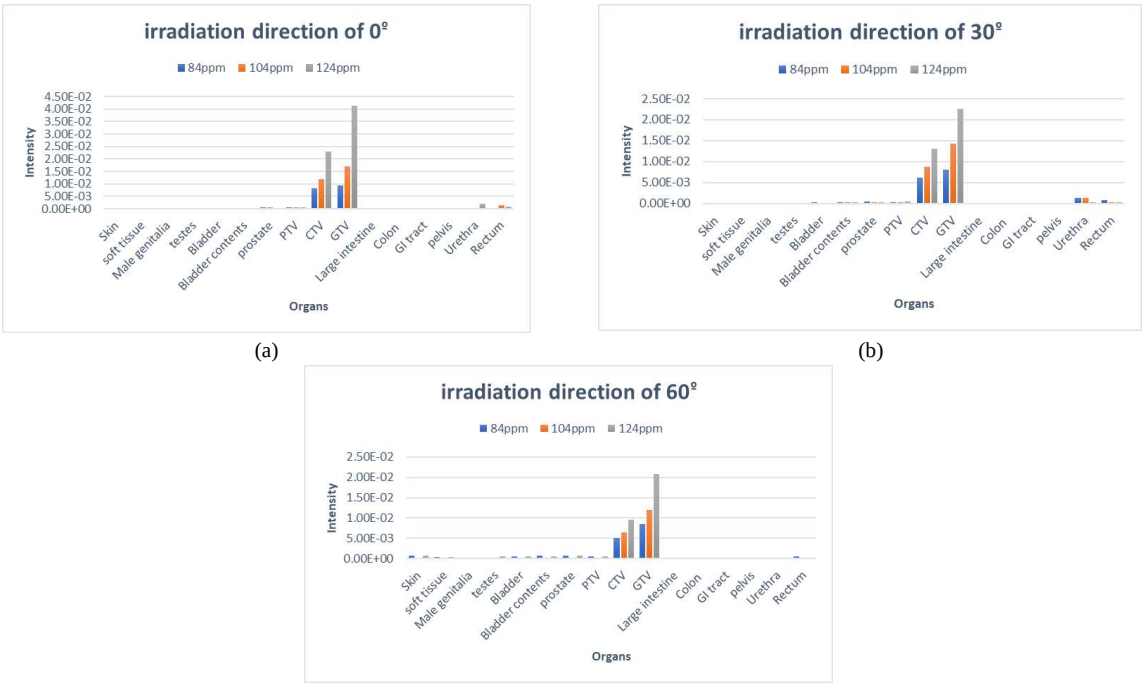

Figure 7. Total dose rate for each OAR from the irradiation direction of (a) 0°, (b) 30°, (c) 60°

Figures 7a-c present the total absorbed dose rate for each organ at risk (OAR) at irradiation angles of 0°, 30°, and 60°. The total dose rate in the gross tumor volume (GTV) increases markedly with boron concentration, consistent with the enhanced probability of the $^{10}B(n, \alpha)^{7}Li$ reaction, which is proportional to the boron atom density ($D_{Total} \propto \Phi\sigma NB$).

For all beam orientations, the gross tumor volume (GTV) received the highest dose rate because of the 10B enrichment ratio of 10 : 5 : 1 (µg/g) among GTV, CTV and normal tissue (International Atomic Energy Agency, 2021). The dose decreased gradually toward surrounding tissues, following the decline in boron concentration and neutron flux intensity. Quantitatively, at 0° irradiation, the GTV dose rate reached 0.0428 Gy/s for 124 µg/g boron, while the bladder and rectum received < 0.005 Gy/s, corresponding to cumulative doses below the 5 Gy safety limit (International Atomic Energy Agency, 2021).

At oblique angles (30° and 60°), the GTV dose rate decreased by ≈ 15–25%, due to increased neutron path lenght and lateral scattering, which reduce the neutron flux at depth. This trend demonstrates that beam alignment along the central axis (0°) maximizes dose delivery efficiency while minimizing irradiation to non-target tissues.

Table 5. Summary of Calculated Dose Rates and Equivalent Dose at GTV (0°, 124 $\mu g/g$)

Component	Physical Dose Rate (Gy/s)	Weighting Factor (ω)	Equivalent Dose Rate ($Gy-Eq/s$)
Boron	$1.02\ x\ 10^{-2}$	3.8	$3.87\ x\ 10^{-2}$
Proton	$5.12\ x\ 10^{-4}$	3.2	$1.64\ x\ 10^{-3}$
Neutron	$6.25\ x\ 10^{-4}$	3.2	$2.00\ x\ 10^{-3}$
Gamma	$4.50\ x\ 10^{-4}$	1.0	$4.50\ x\ 10^{-3}$
Total	$1.18\ x\ 10^{-2}\ (Gy/s)$		$4.15\ x\ 10^{-2}\ (Gy-Eq/s)$

Note: With a total dose rate of $4.15\ x\ 10^{-2}\ (Gy-Eq/s)$, the required irradiation time to achieve the minimum therapeutic dose of 76 $Gy-Eq$ is approximately 30.59 minutes.

3.3 Irradiation Time

The irradiation time required to deliver the prescribed therapeutic dose depends on the total absorbed dose rate. Figure 8 illustrates the relationship between ^{10}B concentration and irradiation time for irradiation angles of 0°, 30°, and 60°.

The results show that increasing boron concentration significantly reduces irradiation time across all configurations. This is consistent with the principle that the total dose rate D_{Total} increases with boron atom density (NB), as the reaction rate $R=\Phi\sigma NB$ of the $^{1}B(n,\alpha)^{7}Li$ process becomes higher. Consequently, the required exposure time $t = D_{target}/D_{Total}$ decreases proportionally.

Among the three angles, based on the optimal simulation parameters (0° beam angle and 124 µg/g boron concentration), the GTV received a total dose rate of $4.15\ x\ 10^{-2}\ (Gy-Eq/s)$. Consequently, to reach the prescribed therapeutic dose of 76 $Gy-Eq$ for the intermediate-risk group, the total irradiation duration was determined to be 30.59 minutes.

This duration falls within the clinically acceptable range of 20–60 minutes for accelerator-based BNCT systems, confirming the feasibility of the proposed treatment configuration (International Atomic Energy Agency, 2021; Suzuki et al., 2014), confirming the feasibility of the modeled configuration.

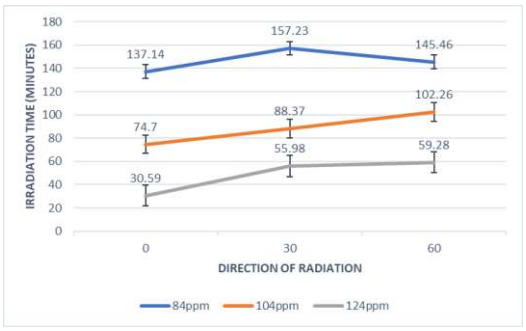

Figure 7. Irradiation Time Graph at angles 0˚, 30°, 60°

3.4 Equivalent Dose to Organs at Risk (OARs)

Figures 9 a-c illustrate the equivalent dose received by each organ at risk (OAR) for irradiation angles of 0°, 30°, and 60°. The gross tumor volume (GTV) consistently received the highest equivalent dose, reaching approximately 76 Gy at 124 µg/g boron, while the surrounding organs such as the bladder and rectum received significantly lower doses (5 Gy).

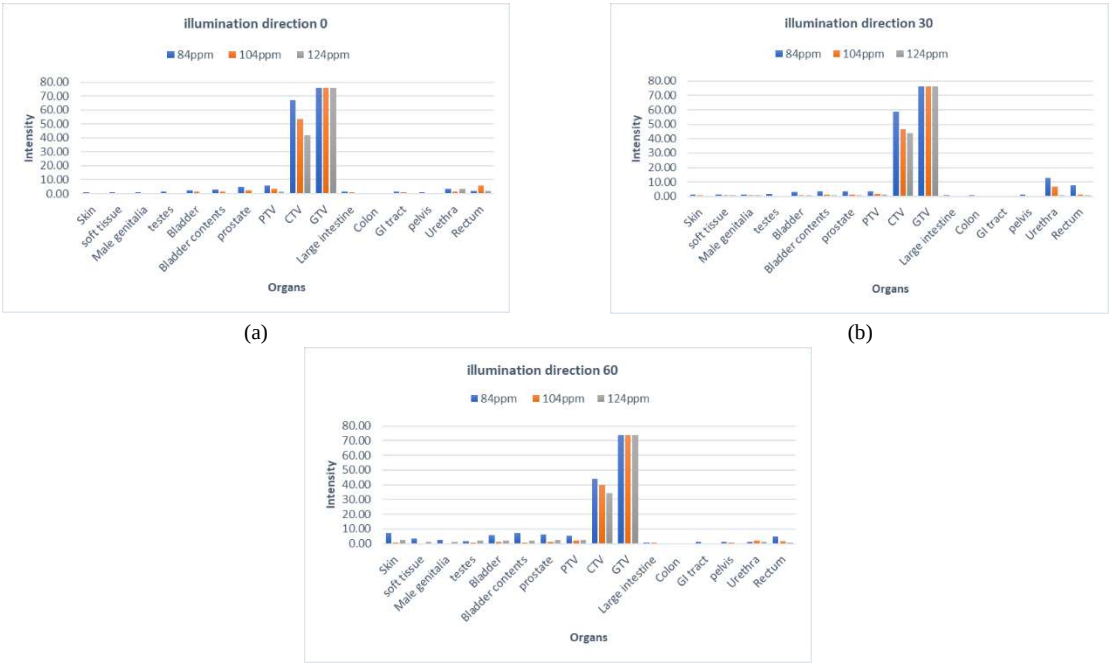

(a) (b)

(c)

Figure 8. Equivalent dose in OAR for radiation direction (a) 0˚, (b) 30˚, (c) 60˚

The ratio of boron concentration between tumor and normal tissue was assumed to 10 : 5 : 1, it means normal tissue receives about 10% of the boron concentration in tumor tissue following standard BNCT tissue uptake data (International Atomic Energy Agency, 2021) Within the tumor, boron uptake was distributed as GTV ≈ 100%, CTV ≈ 50%, and PTV ≈ 5% of the tumor concentration, which reflects the expected gradient in boron delivery (Mirzaei et al., 2014).

As boron concentration increased, the equivalent dose to OARs slightly decreased. This trend results from the selective localization of ^{10}B in tumor tissue, causing most neutron capture reactions to occur within the target volume. The emitted α and ^{7}Li particles have a limited range of 5–9 µm, thus confining energy deposition to the tumor region and reducing dose leakage to surrounding OAR.

All OAR doses remained below the clinical tolerance limit of 5 Gy recommended for pelvic organs in BNCT (International Atomic Energy Agency, 2021), confirming the selectivity and safety of the modeled configuration.

3.5 Comparative And Physical Analysis

Based on the simulation results and dose distribution analysis, variations in irradiation direction irradiation direction significantly influence the dose conformity and protection of surrounding organs. The 0° beam orientation exhibited the most symmetric and concentrated dose distribution on the tumor volume, with a steep dose fall-off toward the bladder and rectum. In contrast, irradiation at 30° and 60° produced elongated isodose patterns, indicating lateral neutron scattering and increased penetration path length, which decreased the dose conformity.

The 0° configuration provided the highest overall dose conformity and the most uniform dose coverage across the gross tumor volume (GTV), demonstrating optimal geometric alignment between the neutron beam and the tumor

center. This condition reduced neutron attenuation and allowed a more direct flux incidence on the GTV, resulting in higher absorbed dose rates and more stable irradiation times across boron concentrations.

At oblique irradiation angles, the increased path length of neutrons through normal tissue (following $x = d/\cos\theta$) led to enhanced scattering and reduced effective flux density at the target, which consequently decreased both the total and equivalent doses in the tumor region by approximately 15–25%. This behavior is consistent with previous Monte Carlo studies on BNCT beam orientation (Suzuki et al., 2014; Koivunoro et al., 2019), which reported that beam direction plays a crucial role in determining dose conformity and treatment efficiency.

Physically, the relationship between boron concentration, neutron flux, and absorbed dose rate can be expressed as:

$$\dot{D}_T = \Phi_\sigma N_B E_{\alpha,Li} \quad (5)$$

where Φ is the thermal neutron flux, σ is the microscopic capture cross-section of ^{10}B (3.84×10^{-22} cm²), NB is the boron atom density, and E_(α,Li) represents the total energy released from the $^{10}B(n,\alpha)\,^{7}Li$ reaction (~2.79 MeV). This proportional relationship explains the observed linear increase in dose rate with boron concentration and the corresponding decrease in irradiation time. From a therapeutic standpoint, the optimal configuration (0° irradiation at 124 µg/g boron concentration) achieved the most favorable dose conformity and maintained OAR doses below 5 Gy, fulfilling the IAEA clinical safety guidelines (International Atomic Energy Agency, 2021).

These results are consistent with previous studies (Suzuki et al., 2014; Koivunoro et al., 2019; Barth et al., n.d.) which demonstrated that increased boron concentration and accurate beam alignment enhance treatment efficiency and dose selectivity in BNCT. The equivalent dose to the tumor region obtained in this simulation (~76 Gy at 124 µg/g) falls within the therapeutic range reported by Barth et al. (2018) for clinical BNCT (60–80 Gy-Eq), while doses to surrounding organs remained within the 5 Gy tolerance limit, confirming both the physical reliability and clinical feasibility of the modeled system. These findings highlight that precise beam orientation, optimized boron delivery, and accurate dose modeling play essential roles in improving therapeutic gain and minimizing collateral damage in accelerator-based BNCT applications.

4. Conclusions

Variations in irradiation direction and boron concentration significantly influenced dose conformity, dose rate, and irradiation time in accelerator-based Boron Neutron Capture Therapy (BNCT) for prostate cancer. The 0° beam orientation achieved the highest conformity index and the lowest exposure to organs at risk (OARs), with an equivalent tumor dose of approximately 76 Gy and a total irradiation time of 30.59 minutes. Increasing boron concentration from 84 µg/g to 124 µg/g improved neutron capture efficiency, resulting in higher absorbed dose within the gross tumor volume (GTV) and reduced treatment time, while OAR doses remained below the clinical tolerance limit of 5 Gy.

These findings confirm the physical reliability of PHITS-based Monte Carlo simulations for dose optimization in BNCT and demonstrate that angular configuration plays a critical role in achieving an optimal balance between tumor control and normal tissue protection. These results can serve as a quantitative reference for the development of treatment-planning protocols in accelerator-based BNCT systems, particularly for prostate and other deep-seated malignancies.

5. Recommendations

a) Future work should include patient-specific anatomical modeling using CT or MRI data to improve dose accuracy and clinical applicability.
b) Further optimization of beam energy spectra and boron compound pharmacokinetics is recommended to enhance treatment selectivity.
c) Experimental validation using physical phantoms or benchmark data is necessary to confirm the Monte Carlo results and support clinical translation.

Overall, the simulation results contribute to the ongoing development of accelerator-based BNCT by providing quantitative insights into the influence of beam orientation and boron concentration on dose distribution, which may serve as a foundation for future clinical treatment planning and system optimization.

Acknowledgment

The authors would like to express our deepest gratitude and highest appreciation to the Physics Study Program, Faculty of Mathematics and Natural Sciences, National Defense University, as well as the National Research and Innovation Agency, Center for Safety, Metrology, and Nuclear Quality Technology Research, Ionizing Radiation Dosimetry Research Group, for all forms of assistance and support provided during this research process.

Author Contribution

This research received significant contributions from Muhammad Nashrun Basyaruddin, Raditya Faradina Pratiwi , Yohannes Sardjono, Gede Sutrisna Wijaya, Isman Mulyadi Triatmoko, Fendinugroho, Nunung Nuraeni, and Heru Prasetio. The other authors participated by reading and approving the final version of the manuscript.

6. Bibliography

Ardana, I. M., & Sardjono, Y. (2017). Optimization of a neutron beam shaping assembly design for BNCT and its dosimetry simulation based on MCNPX. *Jurnal Teknologi Reaktor Nuklir Tri Dasa Mega, 19*(3), 121. https://doi.org/10.17146/tdm.2017.19.3.3582

Arigbede, O., Buxbaum, S. G., Falzarano, S., & Rhie, S. K. (2024). Global disparities in prostate cancer burden: An analysis of the GLOBOCAN 2020 database. *Cancer Epidemiology, Biomarkers & Prevention, 33*(9 Suppl), C001–C001. https://doi.org/10.1158/1538-7755.DISP24-C001

Barth, R. F., Coderre, J. A., Vicente, M. G., & Blue, T. E. (2005). Boron neutron capture therapy of cancer: Current status and future prospects. *Clinical Cancer Research, 11*(11), 3987–4002.

Bolland, W. (2008). Prostate cancer. *InnovAiT: Education and Inspiration for General Practice, 1*(9), 642–650. https://doi.org/10.1093/innovait/inn114

Feuvret, L., Noël, G., Mazeron, J. J., & Bey, P. (2006). Conformity index: A review. *International Journal of Radiation Oncology Biology Physics, 64*(2), 333–342. https://doi.org/10.1016/j.ijrobp.2005.09.028

Fukuda, H. (2021). Boron neutron capture therapy for cutaneous malignant melanoma using BPA. *Cells*. https://doi.org/10.3390/cells10112881

International Agency for Research on Cancer. (2022). *Indonesia source: GLOBOCAN 2022 (The Global Cancer Observatory)*. https://gco.iarc.fr/today/data/factsheets/populations/360-indonesia-fact-sheets.pdf

International Atomic Energy Agency. (2001). *Current status of neutron capture therapy*. https://www.iaea.org/publications/6134/current-status-of-neutron-capture-therapy

Jagt, T. Z., Janssen, T. M., & Sonke, J. J. (2024). Evaluating the effect of higher Monte Carlo statistical uncertainties on accumulated doses after daily adaptive fractionated radiotherapy in prostate cancer. *Physics and Imaging in Radiation Oncology, 32*. https://doi.org/10.1016/j.phro.2024.100636

Jain, M. A., & Sapra, A. (2020). Prostate cancer screening. *StatPearls*. https://pubmed.ncbi.nlm.nih.gov/32310541/

Jin, W. H., Seldon, C., Butkus, M., Sauerwein, W., & Giap, H. B. (2022). A review of boron neutron capture therapy: Its history and current challenges. *International Journal of Particle Therapy*. https://doi.org/10.14338/IJPT-22-00002.1

Koivunoro, H., Kankaanranta, L., Seppälä, T., Haapaniemi, A., Mäkitie, A., & Joensuu, H. (2019). Boron neutron capture therapy for locally recurrent head and neck squamous cell carcinoma: An analysis of dose response and survival. *Radiotherapy and Oncology, 137*, 153–158. https://doi.org/10.1016/j.radonc.2019.04.033

Krstic, D., Markovic, V. M., Jovanovic, Z., Milenkovic, B., Nikezic, D., & Atanackovic, J. (2014). Monte Carlo calculations of lung dose in ORNL phantom for boron neutron capture therapy. *Radiation Protection Dosimetry, 161*(1–4), 269–273. https://doi.org/10.1093/rpd/nct365

Kumada, H., Sakae, T., & Sakurai, H. (2023). Current development status of accelerator-based neutron source for boron neutron capture therapy. *EPJ Techniques and Instrumentation, 10*(1). https://doi.org/10.1140/epjti/s40485-023-00105-5

Lee, C. H., Akin-Olugbade, O., & Kirschenbaum, A. (2011). Overview of prostate anatomy, histology, and pathology. *Endocrinology and Metabolism Clinics of North America*. https://doi.org/10.1016/j.ecl.2011.05.012

Li, G., Jiang, W., Zhang, L., Chen, W., & Li, Q. (2021). Design of beam shaping assemblies for accelerator-based BNCT with multi-terminals. *Frontiers in Public Health, 9*. https://doi.org/10.3389/fpubh.2021.642561

Lu, L., An, S., Guan, F., Wang, Z., & Zhao, Y. (2023). Performance research and optimization of beam shaping assembly used for BNCT based on cyclotron. *IEEE Nuclear Science Symposium Conference Proceedings*. https://doi.org/10.1109/NSSMICRTSD49126.2023.10338497

Meher, N., et al. (2021). Synthesis and preliminary biological assessment of carborane-loaded theranostic nanoparticles to target prostate-specific membrane antigen. *ACS Applied Materials & Interfaces, 13*(46), 54739–54752. https://doi.org/10.1021/acsami.1c16383

Mirzaei, D., Miri-Hakimabad, H., & Rafat-Motavalli, L. (2014). Depth dose evaluation for prostate cancer treatment using boron neutron capture therapy. *Journal of Radioanalytical and Nuclear Chemistry, 302*(3), 1095–1101. https://doi.org/10.1007/s10967-014-3397-2

Nakamura, R., Hino, M., Tanaka, H., Kuriyama, Y., & Iwashita, Y. (2022). Conceptual design of a target station using a 30-MeV cyclotron accelerator for BNCT study. *Nuclear Instruments and Methods in Physics Research Section A, 1042*, 167425. https://doi.org/10.1016/j.nima.2022.167425

Ogawa, T., et al. (2024). Overview of PHITS ver. 3.34 with particular focus on track-structure calculation. *EPJ Nuclear Sciences & Technologies, 10*, 13. https://doi.org/10.1051/epjn/2024012

Panebianco, V., et al. (2018). An update of pitfalls in prostate mpMRI: A practical approach through the lens of PI-RADS v2 guidelines. *Insights into Imaging*. https://doi.org/10.1007/s13244-017-0578-x

Purohit, M., & Kumar, M. (2022). Boron neutron capture therapy: History and recent advances. *Materials Today: Proceedings*. https://doi.org/10.1016/j.matpr.2022.12.181

Schwint, A. E., et al. (2020). Clinical veterinary boron neutron capture therapy studies in dogs with head and neck cancer. *Biology, 9*(10). https://doi.org/10.3390/biology9100327

Sung, H., Ferlay, J., Siegel, R. L., Laversanne, M., Soerjomataram, I., Jemal, A., & Bray, F. (2021). Global cancer statistics 2020: GLOBOCAN estimates of incidence and mortality worldwide for 36 cancers in 185 countries. *CA: A Cancer Journal for Clinicians, 71*(3), 209–249. https://doi.org/10.3322/caac.21660

Suzuki, M., et al. (2014). Boron neutron capture therapy outcomes for advanced or recurrent head and neck cancer. *Journal of Radiation Research*. https://doi.org/10.1093/jrr/rrt098

Wang, S., Zhang, Z., Miao, L., & Li, Y. (2022). Boron neutron capture therapy: Current status and challenges. *Frontiers in Oncology*. https://doi.org/10.3389/fonc.2022.788770

Yeom, Y. S., et al. (2019). Computation speeds and memory requirements of mesh-type ICRP reference computational phantoms in Geant4, MCNP6, and PHITS. *Health Physics, 116*(5).

Zhang, Y. N., et al. (2022). Gross tumor volume delineation in primary prostate cancer on 18F-PSMA-1007 PET/MRI and 68Ga-PSMA-11 PET/MRI. *Cancer Imaging, 22*(1). https://doi.org/10.1186/s40644-022-00475-1

JOURNAL OF ENERGY, MATERIALS, AND INSTRUMENTATION TECHNOLOGY

Journal Webpage https://jemit.fmipa.unila.ac.id/

Mechanical Homogenization of Biochar Porous Structures Using Two-Dimensional RVE: A Study of Finite Element Methods on the Relationship of Actual Porosity and Effective Elastic Modulus

Naufal Nabiha Luthfiantoro, and Ahmad Atif Fikri

Mechanical Engineering, University of Malang, Malang, Indonesia

Article Information

Article history:
Received January 23, 2026
Received in revised form January 30, 2026
Accepted February 28, 2026

Keywords: *Mechanical Properties; Porosity; Finite Element Method; Homogenization; Microstructure*

Abstract

This study analyzes the mechanical response of porous biochar using a 2D FEM–RVE homogenization approach to investigate the effect of mesh-based actual porosity and microstructural arrangement on stiffness and stress concentration. Three types of RVEs (regular, shifted, and random) were simulated at several porosity levels for five biochar types (wood, bamboo, grass, RHB, and sludge) under the assumption of linear elastic material. Loading was applied using kinematic uniform boundary conditions (KUBC), and the effective elastic modulus (E_{eff}) was extracted from the homogenization response, while the maximum stress (σ_{max}) was recorded as an indicator of stress localization. Results show that E_{eff} decreases nonlinearly with increasing ϕ_{mesh}, and at the same porosity, more continuous microstructures retain higher stiffness. Normalization into relative modulus (E_rel) reveals overlapping trends across biochar types for the same RVE, allowing the influence of solid-phase properties to be separated from pore shape effects. These findings underscore the importance of using actual porosity and simultaneously evaluating global stiffness and local stress indicators in interpreting the mechanics of porous biochar.

Informasi Artikel

Proses artikel:
Diterima 3 Januari 2026
Diterima dan direvisi dari 30 Januari 2026
Accepted 28 Februari 2026

Kata kunci: *Mechanical Properties; Porosity; Finite Element Method; Homogenization; Microstructure*

Abstrak

Penelitian ini menganalisis respons mekanik biochar berpori menggunakan pendekatan homogenisasi FEM–RVE dua dimensi untuk mengkaji pengaruh porositas aktual berbasis mesh dan susunan mikrostruktur terhadap kekakuan dan konsentrasi tegangan. Tiga tipe RVE (teratur, tergeser, dan acak) disimulasikan pada beberapa tingkat porositas untuk lima jenis biochar (wood, bamboo, grass, RHB, dan sludge) dengan asumsi material elastik linier. Pembebanan diterapkan menggunakan kinematic uniform boundary condition (KUBC), kemudian modulus elastis efektif (EE_{eff}) diekstraksi dari respons homogenisasi dan tegangan maksimum (σ_max) dicatat sebagai indikator lokalisasi tegangan. Hasil menunjukkan E_{eff} menurun nonlinier seiring meningkatnya ϕ_{mesh}, dan pada porositas yang sama mikrostruktur yang lebih kontinu mempertahankan kekakuan lebih tinggi. Normalisasi menjadi modulus relatif (E_rel) memperlihatkan kecenderungan kurva yang saling berimpit lintas biochar pada RVE yang sama, sehingga pengaruh sifat fase padat dapat dipisahkan dari pengaruh bentuk pori. Temuan ini menegaskan pentingnya penggunaan porositas aktual dan evaluasi simultan kekakuan global serta indikator tegangan lokal dalam interpretasi mekanika biochar berpori..

1. Introduction

Biochar is a porous carbon material produced through the process of pyrolysis biomass under oxygen-limited conditions (M. Zhang dkk., 2022). In recent years, biochar has been widely studied for its potential in a wide range

* Corresponding author.
E-mail address: aufal.nabiha.2205146@stundents.um.ac.id

of engineering and environmental applications, including soil amelioration, environmental remediation, adsorbent materials, as well as as a supporting component in sustainable construction and materials systems. The main characteristic of biochar lies in its complex and multiscale pore structure, which results in a high specific surface area and superior physical–chemical function. These characteristics make biochar an interesting functional material to be developed further.

In general, the mechanical properties of porous materials are determined by a combination of the properties of the solid phase of their constituent and the shape of the pore microstructure (Long dkk., 2021; Xu, 2023). Increased porosity generally leads to a decrease in effective elastic modulus due to a reduction in the load-supporting solid phase fraction and the appearance of a stress concentration around the pores. This kind of porosity-rigidity relationship has been widely studied in various engineered porous material systems, such as lattice structures and Triply Periodic Minimal Surface (TPMS) (Long dkk., 2021; Xu, 2023), and is widely accepted as a basic framework in the mechanical analysis of porous materials.

However, the application of these porosity–mechanical properties relationships to biochar becomes more complex because its microstructures are irregular, heterogeneous, and often disconnected (Zhang et al., 2025; Z. Zhang et al., 2023). At high porosity levels, the mechanical load tends to be concentrated on the remaining solid phase path, thereby increasing the potential for localized deformation and a significant decrease in rigidity. This condition suggests that the mechanical description of biochar cannot always be adequately represented through global porosity parameters alone.

The Finite Element Method (FEM) numerical approach has been widely used to bridge the relationship between microstructures and the mechanical response of porous materials (Huang dkk., 2024; Xu, 2023). In the study of porous materials in general, the global mechanical response is known to be influenced by the multiscale interaction between the microstructure and the solid-phase properties of its constituents, as also reported in a variety of heterogeneous porous media systems (Lv et al., 2023). However, most existing studies still use design target porosity assumptions or simple homogenization parameters, so they do not fully represent the actual geometry of the microstructure analyzed numerically. In addition, studies that systematically evaluate the effect of the microstructure of the Representative Volume Element (RVE) on the elastic response of biochar and explicitly separate the contribution of the solid-phase stiffness properties of biochar from the influence of pore shape in a single consistent homogenization framework are still very limited. As a result, mechanistic understanding of the role of the actual porosity of discretized mesh results and the arrangement of microstructures in controlling the elastic response of porous biochar has not been fully quantified in the literature (Huang et al., 2024; Long et al., 2021; Z. Wang et al., 2024; Xu, 2023; Z. Zhang et al., 2023).

Therefore, this study analyzes the mechanical homogenization of porous biochar using a two-dimensional FEM–RVE approach with variations in microstructure and porosity levels. The analysis focused on the relationship between the actual porosity obtained from the mesh geometry and the effective elastic modulus. Normalization of elastic modulus into relative modulus is applied to separate the influence of the solid-phase stiffness properties of biochar from the influence of pore shape. Through this framework, the research aims to provide a mechanistic understanding of the role of porosity and the microstructure of microstructures in controlling the elastic response of porous biochar (Huang et al., 2024; Long et al., 2021; Z. Wang et al., 2024; Xu, 2023; Z. Zhang et al., 2023).

2. Methodology

2.1 General Framework of FEM–RVE Homogenization

Mechanical analysis of porous biochar was performed using a numerical homogenization based approach *Representative Volume Element* (RVE) with the element method up to (*Finite Element Method*, FEM). The main goal of this approach is to extract the effective elastic properties of the macro scale from the mechanical responses of porous microstructures that are explicitly resolved at the micro scale (Huang et al., 2024; Z. Wang et al., 2024). In the framework of first-order homogenization, the macro strain field is represented through the boundary conditions on the RVE domain, while the local voltage and strain fields are calculated numerically and averaged to obtain effective properties. The FEM–RVE approach has been widely used in heterogeneous porous materials due to its ability to capture the influence of microstructure arrangements, solid phase connectivity, as well as deformation localization potential that cannot be represented by simple analytical homogenization models (Krzaczek et al., 2022; Menke et al., 2021). In the context of porous materials, global mechanical responses are often controlled by the presence of a minimum solid load path and the distribution of local stress in small-sectional ligaments, so explicit analysis at the microscale is crucial.

2.2 RVE Microstructure Design

The biochar microstructure is represented using a two-dimensional RVE that models a solid–void two-phase system. Three types of microstructures were used to separate the effect of the regularity and heterogeneity of solid load paths on mechanical responses, namely RVE1 (regular), RVE2 (displaced with intermediate heterogeneity), and RVE3 (random/irregular). All RVEs have the same domain size and the same number of pore features equalized at each porosity level, so the difference in mechanical response mainly reflects the difference in the topology and connectivity of the solid phase (Krzaczek et al., 2022; Menke et al., 2021).

The RVE1 is built as a periodic void array with a continuous solid load path. The increase in porosity is done by uniformly enlarging the size of the void while maintaining geometric periodicity. RVE2 was developed from RVE1 by applying controlled shifting to the void position, so that the symmetry and continuity of the load path is reduced without changing the pore size statistics. RVE3 is formed through random placement of voids with rules *non-overlap*, which results in a more fragmented and heterogeneous solid-phase network. For RVE3, multiple realizations were used at each porosity condition to capture the statistical variability of the mechanical response (Huang et al., 2024; Z. Wang et al., 2024).

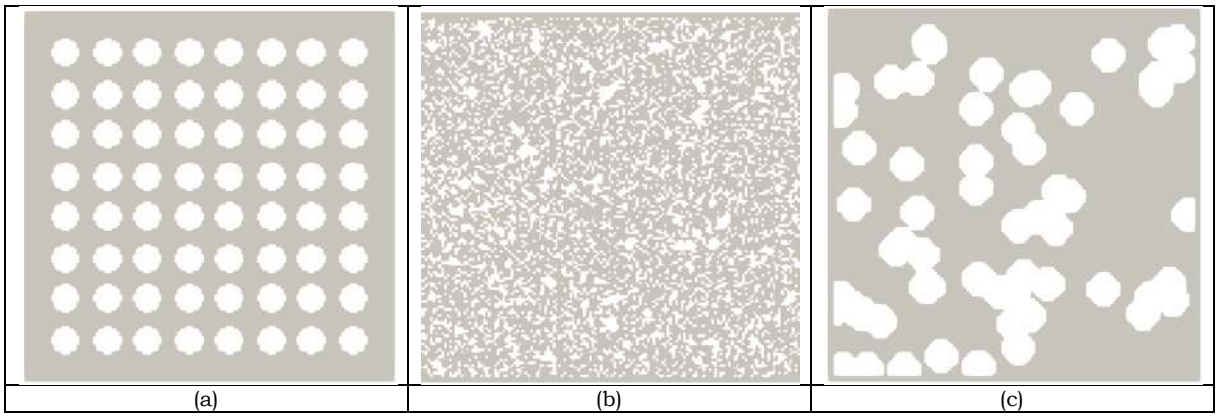

Figure 1. Examples of porous biochar two-dimensional RVE geometry: (a) RVE1 is regular (Bataillou dkk., 2022), (b) RVE2 shifted (Chakma & Luo, 2024) and (c) random RVE3. The three microstructures are equalized in domain size and pore base statistics(Pingaro dkk., 2019)

2.3 Definition of Actual Porosity

The porosity used in the analysis is defined as the actual porosity of the discretized mesh result, which is denoted as . In solid–void two-dimensional systems, porosity is calculated as the ratio of the area of the void phase to the total area of the domain,ϕ_{mesh}

$$\phi_{\text{mesh}} = \frac{A_{\text{void}}}{A_{\text{total}}}$$

The mesh-based porosity definition was chosen because the mechanical response is calculated directly on the discrete geometry used in the FEM simulation. Thus, the actual porosity value expressed as φ_mesh represents the conditions of the structure that are actually numerically analyzed. Some studies have shown that nominal porosity or design target porosity can differ from actual porosity due to geometric discretization and mesh manufacturing processes, especially in porous structures with minimally sized ligaments. Therefore, the use of φ_mesh ensures consistency between the structural descriptors used in the analysis and the simulated numerical domains (Thompson et al., 2021; Zhuang et al., 2022).

2.4 Biochar Solid Phase Material

The solid phase of biochar is modeled as an isotropic linear elastic material. The material parameters used are the Young's modulus of solid phase and Poisson ratio. The five types of biochar are differentiated by value, while they are kept constant for all cases to separate the influence of the material scale from the influence of the microstructure of the microstructure $E_s \nu E_s \nu$(Behazin dkk., 2016). This approach is in line with the practice of modeling porous materials and cellular structures, where effective mechanical properties are seen as the result of the interaction between the material properties of the strut and relative density. (Krzaczek et al., 2022; Menke et al., 2021).

Table 1. The elastic parameters of the solid phase of biochar used in the FEM simulation

Code	Jenis biochar	Young's Modulus of Solid Phase, (GPa)E_s	Rasio Poisson, (-)ν	References
B1	Wood / softwood chip	10.0	0.25	**[11]**
B2	Grass / wheat-straw	5.0	0.25	**[11]**
B3	Bamboo	7.0	0.25	**[12] [13]**
B4	RHB (rice husk biochar)	8.0	0.25	**[12] [13]**
B5	Sludge	4.0	0.25	**[12] [13]**

It should be noted that the solid-phase Young modulus values for wood-based biochar (10 GPa) and grass-based biochar (5 GPa) are adopted directly from the results of nanomechanical measurements reported by E_s(Behazin dkk., 2016). The study showed that the biochar from pyrolysis of lignocellulose biomass has intrinsic stiffness on the order of a few gigapascals, with significant differences depending on the type of feedstock.

Meanwhile, for bamboo-based biochar, rice husk biochar (RHB), and sludge, until this writing stage, no reference has been found that states the exact same value as the value used in the simulation. Therefore, the three materials are treated as assumption parameters that are still within the stiffness range of pyrolysis carbon materials as reported in nanoindentation studies and mechanical analysis of biochar and biochar-based biocomposites E_s(Das dkk., 2016; Zickler et al., 2006). This approach can be accounted for as long as it is explicitly stated as an assumption and is used in the context of FEM-based parametric studies to evaluate the relative influence of solid-phase properties on the effective mechanical response of porous structures.

2.5 Homogenization Boundary Conditions

Mechanical homogenization is carried out using *a displacement-based Kinematic Uniform Boundary Condition* (KUBC). In this scheme, the displacement field at the RVE boundary is forced following the linear macro strain field,

$$u_i(\mathbf{x}) = \varepsilon_{ij}^{\text{macro}}\, x_j$$

For uniaxial loading in the direction, displacement is applied to the left and right boundaries of the domain so as to produce the target macro strain. One additional reference point is locked to eliminate the motion of rigid objects. KUBC was chosen because it is numerically stable and theoretically provides an estimate of the upper limit of the elastic properties effective over other boundary conditions $x\varepsilon_{xx}$(Krzaczek et al., 2022; Menke et al., 2021).

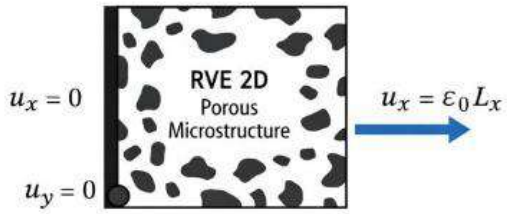

Figure 2. Scheme of application of KUBC on two-dimensional RVE for elastic homogenization.

2.6 FEM Settlement and Effective Quantity Extraction

The linear elastic boundary problem in the RVE domain is solved using *finite element solver* SfePy. The domain is discretized into two-dimensional triangular elements, and the elastic equilibrium equation is solved using *linear solver* directly. Once the displacement field is obtained, the strain and voltage fields are calculated at the level of the solid-phase element (Krzaczek et al., 2022; Menke et al., 2021).

The mean macro voltage in the direction of loading is defined as the average area of the voltage component in the solid phase,

$$\bar{\sigma}_{xx} = \frac{1}{A_s}\int_{\Omega_s} \sigma_{xx}\,(\mathbf{x})\,\mathrm{d}A$$

The effective elastic modulus is then calculated from the ratio between the average stress and the applied macro strain,E_{eff}

$$E_{\text{eff}} = \frac{\bar{\sigma}_{xx}}{\varepsilon_{xx}^{\text{macro}}}$$

In addition to the homogeneous response, the maximum voltage of σ_{max} is recorded as an indicator of local stress concentration related to the heterogeneity of the microstructure and the presence of critical ligaments (Saunier et al., 2024; Tian et al., 2022).

2.7 Normalization and Relative Modulus

In order to separate the influence of the solid phase property from the influence of the pore microstructure, the elastic modulus is effectively normalized into a relative modulus. Normalization is carried out by dividing the solid phase Young modulus of each biochar,$E_{rel}E_{eff}$

$$E_{\text{rel}} = \frac{E_{\text{eff}}}{E_s}$$

This approach allows an evaluation of the internal consistency of homogenization results and emphasizes the role of the shape and arrangement of pore microstructures separately from the properties of solid-phase materials. In linear elastic regimes, the modulus curve relative to the same porosity is expected to show a tendency to constrict each other for various materials, indicating that the elastic response is primarily controlled by the geometry and interconnectedness of the structure. Behavior E_{rel}*collapse* This kind has been widely reported in studies of lattice structures and engineered porous materials (Judawisastra et al., 2025; Lv et al., 2023; M. Zhang et al., 2022).

2.8 Simulation and Data Processing Pipeline

All simulations were run systematically for a combination of RVE type, biochar type, and porosity level. Each case is assigned a unique identity and all input–output parameters are recorded in a structured table format to guarantee repeatability and traceability of results. Quality checks were performed at the pre-simulation (solid-phase connectivity, mesh quality) and post-simulation (reasonableness of values and) stages to minimize numerical artifacts that could affect the interpretation of the results $E_{\text{eff}}\sigma_{\max}$(Krzaczek et al., 2022; Zhuang et al., 2022).

3. Results and Discussions

3.1 Results

Internal Validation of Elastic Models

Before discussing the relationship between porosity and mechanical response, internal validation was performed to ensure that the entire simulation was still in a linear elastic state and was not affected by numerical errors. This validation is carried out by examining the linearity of the relationship between the macro stress and strain, as well as the stability of the elastic modulus value effective against small variations of applied strain (Krzaczek et al., 2022; Menke et al., 2021). All simulations show a linear stress–strain relationship over the strain range used, so that the mechanical response obtained can be considered representative of the elastic behavior of the material.

In addition, based on the examination of the local strain field as commonly reported in the FEM analysis of porous materials (Z. Zhang dkk., 2023), the highest strain concentration was identified in solid-phase ligaments with a minimum cross-section. Meanwhile, most domains exhibit a relatively homogeneous strain distribution, a characteristic typical of elastic responses in multiscale porous materials (Menke et al., 2021). This distribution pattern is also in line with previous findings on engineered porous structures, which suggest that strain localization is primarily controlled by critical ligament geometry and not by numerical instability (Behazin dkk., 2016), so it can be concluded that the simulation is in a linear elastic condition with no indication of local plasticity.

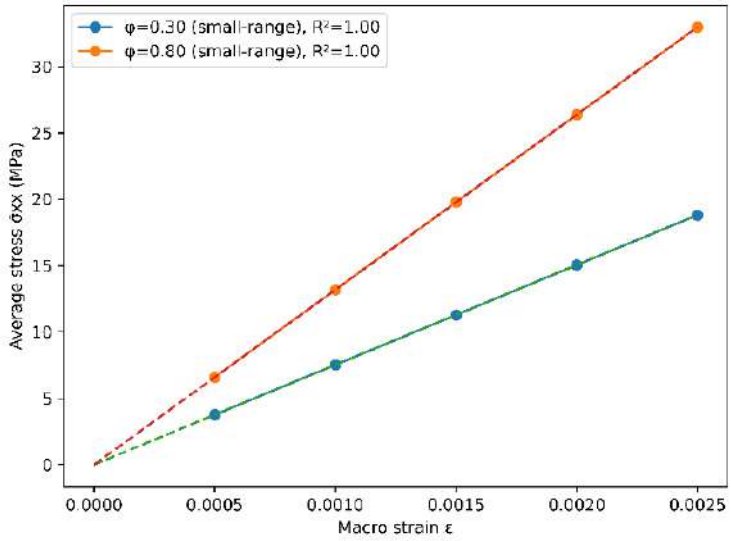

Figure 3. An example of a macro stress–strain relationship resulting from FEM–RVE homogenization showing a linear elastic response.

Figure 3 shows the relationship between the mean macro stress and the applied macro strain for one representative case (RVE1–Wood,). The resulting curve shows a very clear linear relationship over the entire analyzed strain range, with no indication of nonlinearity or deviation from the linear elastic behavior.$\bar{\sigma}_{xx}\varepsilon_{xx}^{macro}\phi_{mesh} \approx 0.30$

This linearity confirms that the mechanical response of RVE is entirely within the range of linear elastic behavior, so that the assumption of isotropic elastic material applied in the FEM simulation remains valid and consistent with the homogenization theory (Krzaczek dkk., 2022).

This figure shows verification that the simulation is in a linear elastic condition because for the two contrasting porosity conditions, and , the relationship between the mean stress and the macro strain remains a straight line at the small strain range used (up to) with for both so that no nonlinear deviation is found at the modulus extraction working range, while the difference in line slope between the two porosities shows that the change in porosity changes the load path and the degree of tension localization in the remaining solid ligaments.$\phi_{mesh} = 0.30\phi_{mesh} = 0.80\bar{\sigma}_{xx}\varepsilon\varepsilon = 0.0025R^2 = 1.00$

Effect of Porosity on Effective Elastic Modulus

Figure 4 shows the variation of the elastic modulus effective against the actual porosity for all RVE types and biochar types. In general, an increase in porosity leads to a decrease that is nonlinear in nature. This behavior reflects a decrease in the fraction of the solid phase that serves as a load-bearer, as well as an increase in the concentration of tension in the remaining ligaments as porosity increases, as reported in studies of porous materials and heterogeneous structures$E_{\text{eff}}\phi_{\text{mesh}}E_{\text{eff}}$(Palomar & Barluenga, 2022; Zickler dkk., 2006). However, at high porosity, the decrease in rigidity becomes more pronounced because—as described in the study of engineered porous structures (Zhang et al., 2025; M. Zhang et al., 2022)The disconnection of the solid load path leads to the dominance of the small-cross-sectional critical ligaments that control the overall mechanical response.

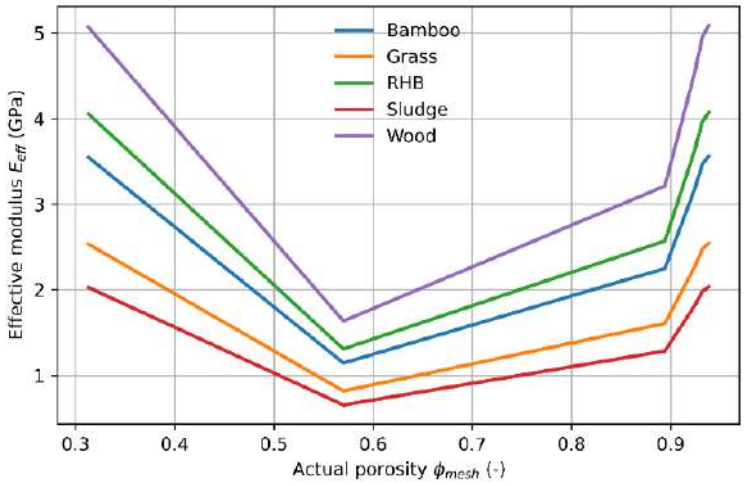

Figure 4. The elastic modulus relationship is effective against the actual porosity for different types of RVE.$\mathbf{E_{eff}\phi_{mesh}}$

A sharp downward bend on the curve against occurs because when the actual porosity increases, the solid-phase network loses load path continuity nonlilaterally, the connective ligaments thin and part of the effective load path disappears, so that the global stiffness drops rapidly over a given porosity range $\boldsymbol{E_{eff}\phi_{mesh}}$(De Carolis dkk., 2024) Meanwhile, the visible increase in high porosity can occur when the configuration/placement of the pore makes the residual load path more efficient in the direction of load so that some structures retain relatively higher rigidity even when the porosity is large, not because the material changes to nonlinear $\boldsymbol{E_{eff}}$(Biswas & Ma, 2022) And this graph is important because it confirms that porosity alone is not always sufficient as the sole foundation of rigidity, geometry and pore space configuration are decisive so that the curve – necessary to map the stiffness sensitivity effectively – while associating the shape of the curve with the shape of the microstructure observed through stress localization $\boldsymbol{E_{eff}\phi_{mesh}}$

Role of RVE Microstructure Arrangement

Comparisons between RVE types show that the arrangement of microstructures has a significant influence on values at the same porosity level. RVE1, which has a more regular void arrangement, produces the highest value because the solid phase path still forms a relatively straight and continuous load trajectory. In contrast, RVE3 with random pore distribution showed the lowest values, which were related to the fragmentation of solid-phase tissues and an increased tendency to localize tension in the minimum cross-sectional ligaments. This behavior is in line with findings in heterogeneous porous materials, where the regularity of the microstructure arrangement plays an important role in maintaining the continuity of load transfer and the stability of the elastic mechanical response $\boldsymbol{E}_{\text{eff}}\boldsymbol{E}_{\text{eff}}\boldsymbol{E}_{\text{eff}}$(Thompson dkk., 2021).

RVE2 displays a response that is somewhere between the two extremes, reflecting the intermediate level of microstructural heterogeneity. These findings indicate that, as reported in studies of heterogeneous porous materials (Behazin dkk., 2016), in addition to total porosity, the topology and connectivity of the solid phase play a dominant role in controlling the effective rigidity of porous materials, especially when the solid-phase network begins to lose continuity (Thompson dkk., 2021).

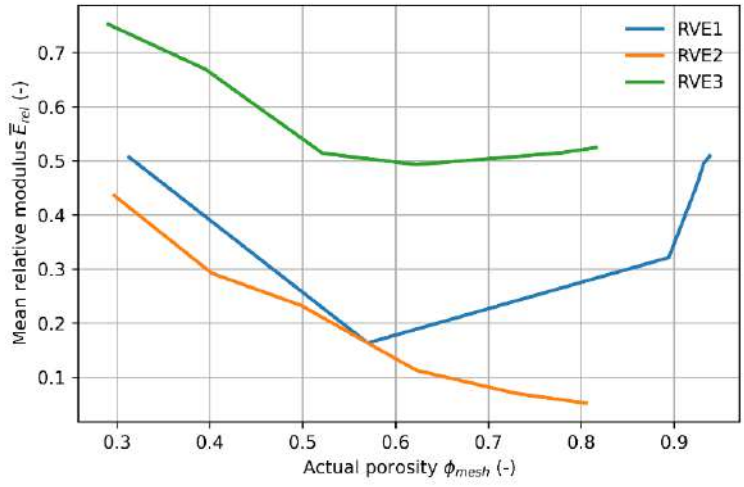

Figure 5. Comparison between RVE types at the same porosity level.$\mathbf{E_{eff}}$

Figure 5 Average relative modulus comparison to actual porosity for RVE1–RVE3. The difference in curves between RVEs at the same porosity shows that the microstructural arrangement (solid-phase load path connectivity and continuity) contributes significantly to effective stiffness, regardless of variations in solid-phase stiffness scales.$\bar{E}_{rel}\phi_{mesh}$

Curve shape – in RVE1 it differs from RVE2 and RVE3 in that the more regular/periodic RVE1 maintains a more continuous solid-phase load path so that the decrease in relative rigidity tends to be more controlled, whereas the shifted RVE2 disrupts symmetry and accelerates the weakening of the ligament connectivity so that it descends more sharply, while the random RVE3 results in a network of load paths that are affected by irregularity/percolation so that the response can be more pronounced $\bar{E}_{rel}\phi_{mesh}\bar{E}_{rel}$*Robust* at a certain porosity range but more sensitive to local configurations that are aligned with the intrinsically non-periodic pore character of biochar (Somboon dkk., 2025), so from this data RVE1 is not automatically more ideal than RVE2/RVE3 because the ideal depends on the purpose: RVE1 is more ideal as a stable and easily reproducible baseline/benchmark for controlled studies, while RVE3 is more statistically representative to generalize the response of random porous materials in an RVE-based homogenization framework (Pingaro dkk., 2019)

Relative Modulus and Separation of Material Influences Microstructure

In order to evaluate the role of the microstructure arrangement of the microstructure independently of the properties of the solid phase, the elastic modulus is effectively normalized to a relative modulus. Figure 6 shows the relationship to all types of biochar in each type of RVE.$E_{rel}E_{rel}\phi_{mesh}$

In the same type of RVE, the curves of different types of biochar tend to overlap, especially in RVE with a more regular arrangement of microstructures. This phenomenon shows that, as reported in studies of lattice structures and engineered porous materials E_{rel}(Zickler dkk., 2006), the absolute value difference is mainly controlled by the mechanical properties of the solid phase of biochar. In contrast, the shape of the relationship between modulus and porosity is more determined by the arrangement and connectivity of the microstructure, which regulates how the load is transferred through the solid-phase network E_{eff}(Palomar & Barluenga, 2022). Behavior *curve collapse* This kind is generally understood as an indicator of the internal consistency of the homogenization process and has been widely used as a conceptual validation in the analysis of elastic porous materials (Lee & al., 2024).

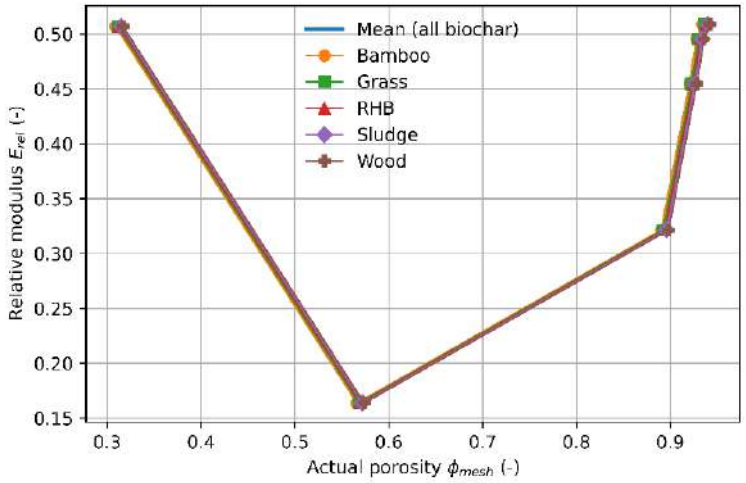

Figure 6. The modulus relationship relative to the actual porosity for different types of biochar in a single type of RVE.$\mathbf{E_{rel}}$

Voltage Distribution and Deformation Localization

The von Mises stress distribution in the RVE domain shows that the maximum stress concentration is mainly localized in the solid-phase ligaments that connect adjacent pores. This localization pattern is in line with the character of heterogeneous elastic porous materials, where the minimum cross-sectional ligament acts as a critical point of load transfer and tends to experience the highest stress concentrations (Thompson dkk., 2021).

The intensity and location of the voltage concentration are greatly influenced by the microstructure arrangement and the level of porosity. In RVE with a regular arrangement, the voltage distribution is relatively symmetrical and more even along the main load path(Guo et al., 2023). In contrast, in RVEs with random pore distribution, the voltage field becomes highly heterogeneous with sharp stress peaks localized to specific ligaments, as also reported in heterogeneous porous structure studies (Palomar & Barluenga, 2022). The maximum stress value increases as porosity increases, which indicates increased susceptibility to local fault initiation, although the global mechanical response still shows linear elastic behavior $\boldsymbol{\sigma}_{\mathbf{max}}$(Behazin dkk., 2016).

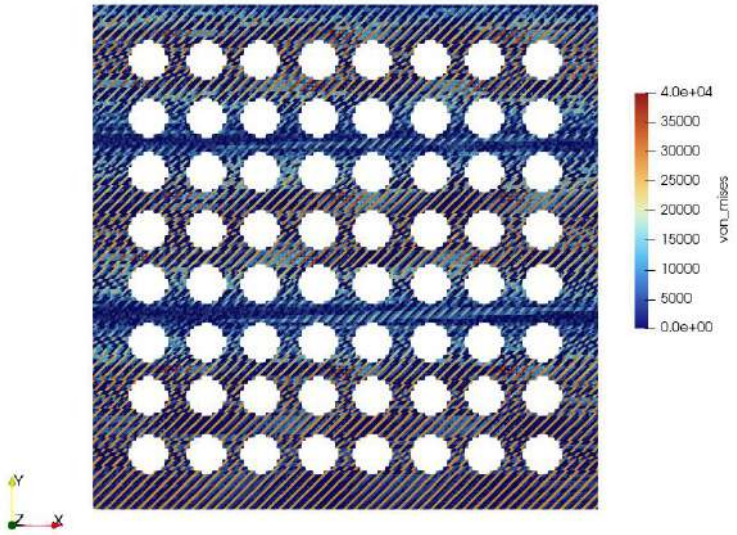

Figure 7. Example of the von Mises voltage distribution on RVE

Summary of Quantitative Results

A summary of the actual porosity values, effective elastic modulus, relative modulus, and maximum stress for the entire combination of RVE type and biochar type are presented in Table 3.1. This table provides a comprehensive quantitative overview of the influence of porosity and the microstructure arrangement of microstructures on the mechanical response of porous biochar.$\boldsymbol{\phi_{mesh} E_{eff} E_{rel} \sigma_{max}}$

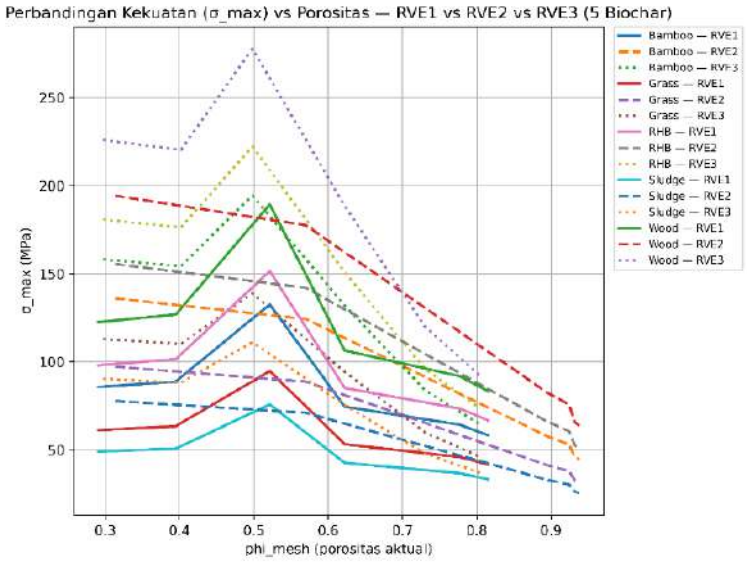

Figure 8. Summary of the mechanical parameters of FEM–RVE homogenization results for all combinations of RVE and biochar types.

The figure shows the relationship between the local maximum voltage () and the actual porosity () for five types of biochar in the three RVE configurations. In general, the entire curve exhibits a nonlinear response to porosity, where it increases and reaches peak values at low–medium porosity (), then decreases at higher porosity. This pattern reflects an increased stress concentration when the solid-phase path is continuous but limited, while the decrease in high porosity is related to weakened solid-phase connectivity and reduced ability of porous structures to transfer stress effectively, as reported in studies of heterogeneous elastic porous materials [11], [14]. $\boldsymbol{\sigma_{max}\phi_{mesh}\sigma_{max}\phi_{mesh} \approx 0,3–0,5\sigma_{max}}$The difference in values at the same porosity confirms the role of the microstructure of RVE and the solid-phase properties of biochar on local stress distribution [18]. Wood and bamboo-based biochar tend to show higher than thatching, rice husk, and mud-based biochar,$\boldsymbol{\sigma_{max}\sigma_{max}}$ The wood and bamboo biochar on the graph are affected because the more "skeletonized" lignocellulose feedstock is able to maintain a hierarchical architecture and a high carbon fraction so that its micromechanical properties (hardness/indentation response) can reach high values when the original structure is maintained (Q. Wang dkk., 2025), while straw and rice husk biochar tend to carry larger ash/mineral fractions (including inorganic components that modify the pyrolysis pathway and increase the heterogeneity of solids) so that the load-bearing carbon frame becomes more disrupted and effectively lowers the solid

rigidity seen by homogenization (Puri et al., 2024), and in mud-based biochar this difference is usually stronger because the character of sludge-derived biochar is generally rich in minerals/inorganic components and more complex/heterogeneous so that it is mechanically less ideal as an elastic load-bearing framework than lignocellulose biochar (Zhou et al., 2024), so that when in the simulation the differences between biochars are modeled through solid phase parameters, the output directly follows the solid stiffness scale and is physically consistent with the carbon-ash microstructure differences reported in the recent literature indicating a stiffer load path but more susceptible to voltage localization. In the context of this study, it is used as an indicator of elastic microstructural vulnerability, so that the results obtained represent a comparison of the relative mechanical response between RVE and between biochar types, not as a measure of material collapse strength.$\boldsymbol{E_0 E_{eff} \sigma_{\max}}$

3.2 Discussions

This discussion focuses on how the actual mesh-based porosity (φ_mesh), variation in the RVE microstructure arrangement, and the overall solid phase nature of biochar impact the elastic response expressed through effective elastic modulus (E_eff), relative modulus (E_rel), and maximum stress (σ_max). The focus is not only on showing trends, but explaining the mechanisms that cause those trends to appear in porous materials.

Increased φ_mesh consistently lowers E_eff across all RVE types and all biochar. Physically, as the pores increase, the dense part of the load carrier decreases and the load transfer path becomes narrower or more severed, so that the effective rigidity also decreases. This pattern is common in porous materials and cellular structures, as reported in TPMS/lattice structures and engineered porous systems (Zhang et al., 2025; M. Zhang et al., 2022) and in porous carbon materials with interconnected dense-pore tissues (Gibson & Ashby, 1982; Sadek & al., 2024). The use of φ_mesh also reinforces the consistency of interpretation because FEM responses are calculated on discrete geometry that is actually simulated; The target/design porosity may deviate from the actual porosity due to discretization and mesh fabrication, especially when minimum ligaments are the determining factor (Thompson et al., 2021; Zhuang et al., 2022).

At the same φ_mesh value, the difference in the microstructure of the RVE still results in a noticeable E_eff difference. RVEs with more connected solid-phase networks tend to maintain higher E_eff, while more random/fragmented microstructures are more prone to localized deformation so that E_eff descend (Huang et al., 2024; Z. Zhang et al., 2023). These findings are in line with studies of foam/porous materials that emphasize that not only the number of pores, but also the distribution of pore size and the connectivity of solid tissues play a major role in determining the effective elastic modulus (Gibson & Ashby, 1982; Li dkk., 2021). Normalization of E_eff into E_rel helps to separate the influence of solid-phase stiffness scale from the influence of pore shape: in the same type of RVE, inter-biochar E_rel curves that tend to overlap each other show that E_eff differences are mainly due to solid-phase modulus differences, while the pattern of decline in porosity is more determined by the arrangement of microstructures; This approach is commonly used as an internal consistency check in the study of porous structures/lattices (Stuart et al., 2025), and is also reported on porous carbon systems (Gibson & Ashby, 1982). At very high porosity, small inter-curve deviations are still possible due to the increasingly sensitive response to minimum ligament details and local irregularities (Behazin et al., 2016; Z. Zhang et al., 2023)

In terms of local response, increased porosity is generally followed by increased σ_max, which indicates that stress tends to accumulate in the remaining ligaments as the solid phase fraction decreases; This phenomenon is a common feature of porous materials and is usually sharper in microstructures with low affinity (Behazin et al., 2016; Z. Zhang et al., 2023). In complex structured carbon materials, the heterogeneity of solid tissues also often gives rise to stress concentration points that are relevant to initial mechanical susceptibility (Gibson & Ashby, 1982; Sadek & al., 2024). In addition, multiscale studies on biochar systems in composite matrices show that microstructural inconsistencies can trigger dominant local responses even though the discussion is still at low load (Manna & al., 2025). Therefore, σ_max in this study is best treated as an indicator of elastic microstructural vulnerability, not a measure of material collapse strength.

4. Conclusions

The results showed that mesh-based actual porosity (φ_{mesh}) was the most consistent parameter in explaining stiffness attenuation, where E_{eff} systematically decreased as φ_{mesh} increased for all combinations of RVE type and biochar type. Although φ_{mesh} the same, the microstructure of RVE still produces a noticeable E_{eff} difference; RVEs with more connected solid-phase networks maintain higher E_{eff}, while more fragmented microstructures decrease E_{eff} due to localization of deformation. The relative modulus (E_{rel}) pattern indicates that absolute E_{eff} variation is more influenced by the rigidity of the solid phase, while the decrease in porosity is determined by the microstructure. In addition, the local maximum stress (σ_{max}) increases with φ_{mesh} and appears on critical ligaments, confirming that this indicator is more relevant to the vulnerability of elastic microstructures than to the collapse strength of the material. This study presents a controlled and reproductive 2D FEM–RVE framework, confirms the role of φ_{mesh} as a numerical structure descriptor, and presents E_{eff}–E_{rel}–σ_{max} metrics to assess the stiffness and vulnerability of microstructures simultaneously.

However, this research model has limitations because it is still 2D, so the three-dimensional effects, spatial anisotropy, and 3D connectivity are not fully represented, and the solid phase is assumed to be isotropic linear elastic without considering plasticity, damage, or cracking. For follow-up research, it is recommended to develop a 3D RVE to evaluate network anisotropy and connectivity, incorporate a nonlinear model or damage to attribute σ_{max} to failure initiation, and add numerical robustness studies related to RVE size, random realization variations, and mesh sensitivity to establish limits on applicability and uncertainty of outcomes.

Acknowledgement

This research was completed well thanks to the support and assistance from various parties. The author would like to thank all who have provided guidance, input, and motivation during the research process.

5. Bibliography

Bataillou, G., Lee, C., Monnier, V., Gerges, T., Sabac, A., Vollaire, C., & Haddour, N. (2022). Cedar Wood-Based Biochar: Properties, Characterization, and Applications as Anodes in Microbial Fuel Cell. *Applied Biochemistry and Biotechnology*, *194*(9), 4169–4186. https://doi.org/10.1007/s12010-022-03997-3

Behazin, E., Ogunsona, E., Rodriguez-Uribe, A., Mohanty, A. K., Misra, M., & Anyia, A. O. (2016). Mechanical, chemical, and physical properties of wood and perennial grass biochars for possible composite application. *BioResources*, *11*(1), 1334–1348.

Biswas, P., & Ma, J. (2022). Spatial pore distribution: An approach to uncouple the strength–porosity trade-offs. *Journal of Materials Science*, *57*(1), 411–421. https://doi.org/10.1007/s10853-021-06587-6

Chakma, P., & Luo, Y. (2024). Impact of Regular and Irregular Pore Distributions on the Elasticity of Porous Materials: A Microstructure-Free Finite Element Study. *Materials*, *17*(18), 4490. https://doi.org/10.3390/ma17184490

Das, O., Sarmah, A. K., & Bhattacharyya, D. (2016). Nanoindentation assisted analysis of biochar added biocomposites. *Compos. Part B Eng.*, *91*, 219–227.

De Carolis, S., Putignano, C., Soria, L., & Carbone, G. (2024). Effect of porosity and pore size distribution on elastic modulus of foams. *International Journal of Mechanical Sciences*, *261*, 108661. https://doi.org/10.1016/j.ijmecsci.2023.108661

Gibson, L. J., & Ashby, M. F. (1982). The mechanics of three-dimensional cellular materials. *Proc. R. Soc. A*, *382*(1782), 43–59. https://doi.org/10.1098/rspa.1982.0088

Guo, W., Wang, F., Wu, Y., Jiang, J., & Xu, W. (2023). New insights into freezing behavior of saturated and air-entrained porous media via a micromechanics-based thermo-hydro-mechanical model. *Water Resour. Res.*, *59*(4). https://doi.org/10.1029/2022WR034211

Huang, W., Meng, F., Liu, J., & Wong, T. (2024). Development of compaction localization in Leitha limestone: Finite element modeling based on synchrotron X-ray imaging. *J. Geophys. Res. Solid Earth*, *129*(8). https://doi.org/10.1029/2024JB028868

Judawisastra, N., Wicaksono, S., Dwianto, Y., Mahyuddin, A., Dirgantara, T., & Zuhal, L. (2025). Comprehensive prediction of the relative modulus of strut-based gyroid lattice structures employing an ML-based surrogate model. *J. Biomed. Mater. Res. B Appl. Biomater.*, *113*(8). https://doi.org/10.1002/jbm.b.35613

Krzaczek, M., Nitka, M., & Tejchman, J. (2022). A novel DEM-based pore-scale thermo-hydro-mechanical model for fractured non-saturated porous materials. *Acta Geotech.*, *18*(5), 2487–2512. https://doi.org/10.1007/s11440-022-01746-8

Lee, J., & al., et. (2024). Engineering a hierarchy of disorder: A new route to synthesize high-performance 3D nanoporous all-carbon materials. *Adv. Mater.*, *36*(32). https://doi.org/10.1002/adma.202402628

Li, S., Xu, J., Liu, Z., & Zhang, Y. (2021). A 3D RVE-based computational homogenization approach for predicting the effective elastic properties of periodic porous materials. *Comput. Mater. Sci.*, *199*, 110738. https://doi.org/10.1016/j.commatsci.2021.110738

Long, K., Chen, Z., Zhang, C., Yang, X., & Saeed, N. (2021). An aggregation-free local volume fraction formulation for topological design of porous structures. *Materials*, *14*(19), 5726. https://doi.org/10.3390/ma14195726

Lv, W., Hu, J., Liu, J., Xiong, C., & Zhu, F. (2023). Porosity effect on the mechanical properties of nano-silver solder. *Nanotechnology*, *34*(16), 165701. https://doi.org/10.1088/1361-6528/acb4f3

Manna, K., & al., et. (2025). Microstructural characterization of ball-milled biochar and its reinforcing efficiency in biobased thermoplastic polyurethane. *ACS Sustain. Resour. Manage.*, *2*(9), 1719–1730. https://doi.org/10.1021/acssusresmgt.5c00225

Menke, H., Maes, J., & Geiger, S. (2021). Upscaling the porosity–permeability relationship of a microporous carbonate for Darcy-scale flow with machine learning. *Sci. Rep.*, *11*(1). https://doi.org/10.1038/s41598-021-82029-2

Palomar, I., & Barluenga, G. (2022). Acoustic assessment of multiscale porous lime–cement mortars. *Materials*, *16*(1), 322. https://doi.org/10.3390/ma16010322

Pingaro, M., Reccia, E., & Trovalusci, P. (2019). Homogenization of Random Porous Materials With Low-Order Virtual Elements. *ASCE-ASME Journal of Risk and Uncertainty in Engineering Systems Part B: Mechanical Engineering*, *5*(3), 030905. https://doi.org/10.1115/1.4043475

Puri, L., Hu, Y., & Naterer, G. (2024). Critical review of the role of ash content and composition in biomass pyrolysis. *Frontiers in Fuels*, *2*, 1378361. https://doi.org/10.3389/ffuel.2024.1378361

Sadek, H., & al., et. (2024). Well-ordered bicontinuous nanohybrids from a bottom-up approach for enhanced strength and toughness. *Nano Lett.*, *24*(35), 11020–11027. https://doi.org/10.1021/acs.nanolett.4c03157

Saunier, J., Chinnayya, A., Kaeshammer, É., Reynaud, M., & Genetier, M. (2024). Mesoscale modeling of the shock-to-detonation transition of pressed HMX. *Propellants Explos. Pyrotech.*, *49*(9). https://doi.org/10.1002/prep.202400125

Somboon, S., Schlichenmaier, S., Thumanu, K., Pakawanit, P., Yodda, S., Sukitprapanon, T.-S., & Lawongsa, P. (2025). Transformations in physicochemical properties and pore structure of biochar derived from rice straw revealed by synchrotron techniques. *Scientific Reports*, *15*(1), 23641. https://doi.org/10.1038/s41598-025-08772-y

Thompson, E., Tomenchok, K., Olson, T., & Ellis, B. (2021). Reducing user bias in X-ray computed tomography-derived rock parameters through image filtering. *Transp. Porous Media*, *140*(2), 493–509. https://doi.org/10.1007/s11242-021-01690-3

Tian, Y., Zhan, W., Jamal, A., & Dini, D. (2022). On the microstructurally driven heterogeneous response of brain white matter to drug infusion pressure. *Biomech. Model. Mechanobiol.*, *21*(4), 1299–1316. https://doi.org/10.1007/s10237-022-01592-3

Wang, Q., Ji, Y., Sridharan, M. M., Lang, L., Zou, Y., Kirk, D. W., & Jia, C. Q. (2025). Unlocking extreme anisotropy in monolithic biochar hardness. *Biochar X*, *1*(1), 0–0. https://doi.org/10.48130/bchax-0025-0007

Wang, Z., Ding, X., Liu, J., & Fu, L. (2024). Numerical simulations on compression behaviors of laminated shale based on digital image technology and the discrete element method. *Sci. Rep.*, *14*(1). https://doi.org/10.1038/s41598-024-66333-1

Xu, X. (2023). Grain-level numerical simulations for the effective elasticity of weakly cemented sandstones. *ACS Omega*, *8*(37), 33610–33621. https://doi.org/10.1021/acsomega.3c03802

Zhang, M., Xu, M., Li, J., Shi, W., & Chen, Y. (2022). Compressive behavior of hollow triply periodic minimal surface cellular structures manufactured by selective laser melting. *Rapid Prototyping Journal*, *29*(3), 569–581. https://doi.org/10.1108/RPJ-04-2022-0128

Zhang, Z., Qi, Y., Wei, B., Bao, H., & Xu, Y. (2023). Application strategy of finite element analysis in artificial knee arthroplasty. *Front. Bioeng. Biotechnol.*, *11*. https://doi.org/10.3389/fbioe.2023.1127289

Zhou, Y., Gao, J., Yang, X., Ni, H., Qi, J., Zhu, Z., Yang, Y., Fang, D., Zhou, L., & Li, J. (2024). Recent Progress in Sludge-Derived Biochar and Its Role in Wastewater Purification. *Sustainability*, *16*(12), 5012. https://doi.org/10.3390/su16125012

Zhuang, Ł., Shin, H., Yeom, S., Pham, C., & Kim, Y. (2022). A novel method for estimating subresolution porosity from CT images and its application to homogeneity evaluation of porous media. *Sci. Rep.*, *12*(1). https://doi.org/10.1038/s41598-022-20086-x

Zickler, G. A., Schöberl, T., & Paris, O. (2006). Mechanical properties of pyrolysed wood: A nanoindentation study. *Philos. Mag.*, *86*, 1373–1386.

MINISTRY OF EDUCATION, CULTURE, RESEARCH, AND TECHNOLOGY
UNIVERSITY OF LAMPUNG
FACULTY OF MATHEMATICS AND NATURAL SCIENCE
DEPARTMENT OF PHYSICS
St. Prof. Dr. Soemantri Brodjonegoro No.1 Bandar Lampung 35145 http://fisika.fmipa.unila.ac.id
Telp. 0721-704625 - Fax. 0721-704625